Fundus Spectroscopy and Studies in Retinal Oximetry using Intravitreal Illumination

by
David Alan Salyer

A Dissertation Submitted to the Faculty of the
Committee on Optical Sciences (Graduate)
In Partial Fulfillment of the Requirements
For the Degree of
Doctor of Philosophy
In the Graduate College
The University of Arizona

2 0 0 6

THE UNIVERSITY OF ARIZONA

GRADUATE COLLEGE

As members of the Dissertation Committee, we certify that we have read the dissertation prepared by David A. Salyer entitled Fundus Spectroscopy and Studies in Retinal Oximetry using Intravitreal Illumination and recommend that it be accepted as fulfilling the dissertation requirement for the Degree of Doctor of Philosophy.

Dr. Russell A. Chipman Date: 11/16/2006

Dr. Robert I. Park, MD Date: 11/16/2006

Dr. Kurt R. Denninghoff, MD Date: 11/16/2006

Final approval and acceptance of this dissertation is contingent upon the candidate's submission of the final copies of the dissertation to the Graduate College.

I hereby certify that I have read this dissertation prepared under my direction and recommend that it be accepted as fulfilling the dissertation requirement.

Dissertation Director: Dr. Russell A. Chipman Date: 11/16/2006

Statement by Author

This dissertation has been submitted in partial fulfillment of requirements for an advanced degree at The University of Arizona and is deposited in the University Library to be made available to borrowers under rules of the Library.

Brief quotations from this dissertation are allowable without special permission, provided that accurate acknowledgment of source is made. Requests for permission for extended quotation from or reproduction of this manuscript in whole or in part may be granted by the copyright holder.

Signed: David A. Salyer

Acknowledgments

I dedicate this dissertation to my wife and best friend, Renee Kathryn Salyer. Her unwavering faith in me and her patience through this long research project has made all of this work possible. She also deserves thanks and recognition for countless hours spent proofreading this document. Renee has learned a lot more about optics and retinal oximetry than she ever planned to. I also would like to thank my parents, Goebel and Pauline Salyer, family and friends for their incredible support over my incredibly long academic career. I owe everything I am to them.

Dr. Russell Chipman served as an advisor, mentor, and friend over the course of this dissertation. Russell continuously brought out the best in me with his timely advice and high expectations. Dr. Robert Park is a truly talented retinal surgeon and researcher; his skills ultimately enabled all of the research contained in this dissertation. My research team at the University of Arizona was truly a pleasure to work with. Dr. Neil Beaudry made countless contributions to the project including software development and data processing techniques. Neil's skills are great and diverse, he was truly an integral part of this project. Dr. Sreenivasa Basavanthappa is a skilled surgeon as well as a gifted researcher. Sreeni was involved in every phase of the live swine experiments and data analysis. Karen Twietmeyer wrote fine data analysis code that I used for dissecting the large amount of data collected over the course of the research. In addition, Karen made all of the papers that resulted from this work better with her skilled writing and valuable (although sometimes painful) critique of my writing. Finally, I'd like to thank Dr. Kurt Denninghoff for infusing me with enthusiasm for my research when my enthusiasm started to wane. Dr. Denninghoff's vast experience in the subject matter and his tireless effort made this dissertation better.

One final thank you is in order...I'd like to thank my daughter Farrah Jane Salyer for coming into the world and giving me the final impetus to finish.

Table of Contents

Table of Contents—*Continued*

Table of Contents—*Continued*

List of Figures

List of Figures—*Continued*

List of Figures—*Continued*

List of Figures—*Continued*

List of Figures—*Continued*

List of Figures—*Continued*

List of Figures—*Continued*

List of Tables

Abstract

This dissertation documents the development of a new illumination technique for use in the studies of retinal oximetry and fundus spectroscopy. Intravitreal illumination is a technique where the back of the eye is illuminated trans-sclerally using a scanning monochromator coupled into a fiber optic illuminator. Retinal oximetry is the process of measuring the oxygen saturation of blood contained in retinal vessels by quantitative measurement of the characteristic color shift seen as blood oxygen saturation changes from oxygenated blood (reddish) to deoxygenated blood (bluish). Retinal oximetry was first attempted in 1963 but due to a variety of problems with accuracy and difficulty of measurement, has not matured to the point of clinical acceptability or commercial viability.

Accurate retinal oximetry relies in part on an adequate understanding of the spectral reflectance characteristics of the fundus. The use of intravitreal illumination allows new investigations into the spectral reflectance properties of the fundus. The results of much research in fundus reflectance and retinal oximetry is detailed in this document, providing new insight into both of these related fields of study.

Intravitreal illumination has been used to study retinal vessel oximetry and fundus reflectometry resulting in several important findings that are presented in this document. Studies on enucleated swine eyes have provided new insight into the bidirectional reflectance distribution function of the fundus. Research on live swine has shown accurate measurement of retinal vessel oxygen saturation and provided the first *in vivo* spectral transmittance measurement of the sensory retina. A secondary discovery during this research suggests that vitrectomy alters the retinal vasculature, an finding that should spawn new research in its own right.

Chapter 1
Introduction

This dissertation documents the development of a new illumination technique for use in the studies of retinal oximetry and fundus spectroscopy. Intravitreal illumination is a technique where the back of the eye is illuminated trans-sclerally using a scanning monochromator coupled into a fiber optic illuminator. Retinal oximetry is the process of measuring the oxygen saturation of blood contained in retinal vessels by quantitative measurement of the characteristic color shift seen as blood oxygen saturation changes from oxygenated blood (reddish) to deoxygenated blood (bluish). Retinal oximetry was first attempted in 1963 [3], but due to a variety of problems with accuracy and difficulty of measurement, has not matured to the point of clinical acceptability or commercial viability.

Accurate retinal oximetry relies in part on an adequate understanding of the spectral reflectance characteristics of the fundus. The use of intravitreal illumination allows new investigations into the spectral reflectance properties of the fundus. The results of much research in fundus reflectance and retinal oximetry is detailed in this document, providing new insight into both of these related fields of study.

1.1 Motivation for Research

The need exists for a non-invasive eye oximeter that is reliable and accurate for a wide range of oxygen saturations. Optical oximetry is an established method used by physicians for the purpose of clinical diagnostics and patient monitoring [4, 5]. The most common non-invasive clinical method is pulse oximetry. Pulse oximeters are used in the monitoring of a patient's arterial oxygen saturation (S_aO_2). Of particular interest to emergency room doctors, however, is the monitoring of mixed venous

oxygen saturation (S_vO_2) as it has been shown to be an extremely sensitive indicator of occult (internal) bleeding [6]. Retinal oximetry provides data for both S_aO_2 and S_vO_2 as both retinal arteries and veins are accessible for analysis. Retinal oximetry has promise for ophthalmic purposes as well. Pathologic conditions in the retina can lead to vision loss and blindness. The retina requires an exorbitant amount of oxygen, and hypoxia (lack of oxygen) of the retina is believed to be a factor in the development of ocular vascular diseases such as diabetic retinopathy and glaucoma [7, 8, 9]. The ability to measure oxygen saturation in the ocular fundus could improve the understanding and early diagnosis of these ocular diseases.

Retinal oximetry is difficult due to a host of problems such as uncertain light paths, extraneous specular reflections from vessel surfaces and other ocular surfaces, and non optimized choices of analysis wavelengths. Various retinal oximetry techniques have been investigated for over 50 years, but no viable commercial retinal oximeter is currently in use. All of these oximeters have used transcorneal illumination and are non-invasive. Non-invasive transcorneal illumination is used on all conventional fundus cameras in which the illuminating light is directed through the cornea. One disadvantage of transcorneal illumination that hampers accurate vessel absorption measurements is the bright specular reflections from the top surface of the blood vessel (hereafter referred to as glints) cause the vessel transmission profile to appear W-shaped rather than the expected U-shaped. Additionally, the light in transcorneal images of retinal vessels is a mixture of light which has single-passed and double-passed the vessel, as well as scattered from other ocular surfaces. Although it is essential to accurately measure the spectrum of retinal blood in-vivo, assigning partial spectral changes between single the double pass light is difficult using transcorneal illumination.

To address the difficulties associated with transcorneal retinal oximetry, this dissertation details the development of a new illumination method with the goal of obtaining more accurate measurements of retinal blood oxygen saturation using in-

traocular illumination. A fiber optic illuminator coupled to a scanning monochromator is used to obliquely illuminate the fundus. The invasive nature of this method excludes it from use in clinical settings. However, this dissertation demonstrates the usefulness of the technique as a research tool for use in animal models, both through its ability to greatly reduce the effect of the central glint which occurs when using transcorneal illumination, as well as offering much more control over the retinal illumination allowing a distinct separation between single-pass and double-pass light.

Development of this invasive technique is meant to solve these long standing problems and provide a gold standard to which future noninvasive eye oximeters can be compared. All experiments were performed on porcine eyes due to their availability and extensive similarities to human eyes, particularly in the retinal vasculature [10]. The knowledge gained through this research will help to guide the design and development of future non-invasive eye oximetry instruments.

1.2 Organization of Dissertation

Accurate measurement of oxygen saturation in retinal vessels requires a complete understanding of the structure of the eye, especially the fundus which contains the retinal vessels. Chapter 2 begins by describing the basic anatomy of the eye and the detailed anatomy of the retina and posterior layers. It goes on to describe the blood supply system to the retina including retinal blood flow and characteristic vessel size. Finally, the principles of retinal oximetry and are described and a review of previous work done on retinal oximetry and fundus reflectometry is provided.

Preparation for live animal experiments on swine eyes was accomplished by work on enucleated swine eyes. Chapter 3 describes the work with enucleated eyes, including the hardware and software developed to support the research described in this dissertation. Through cannulation of the chorio-retinal artery, we were able to perfuse the enucleated eye with blood of varying oxygen content and perfect our spectral

imaging technique. Spectral transmittance data from retinal vessels as well as fundus spectral reflectance data is presented.

Chapter 4 describes a series of experiments performed on enucleated eyes in which the spectral reflectance of the fundus was characterized for a variety of illumination angles. The flexibility provided by intravitreal illumination allowed us to take previously unobtainable measurements. This work led to a publication in Investigative Ophthalmology and Visual Science.

A series of live swine experiments were performed using the techniques developed from this research. Multispectral image sets of retinal vessels were obtained as the animals' blood oxygen content was lowered. Chapters 5 details the oximetry performed on two of the swine that produced the most repeatable and well behaved data.

Chapter 6 presents further oximetry results two experiments performed on swine eyes. In the first experiment, a small piece of Spectralon was subretinally inserted beneath the retina of one of the swine eyes discussed in chapter 5, and the same retinal vessels are remeasured for decreasing oxygen saturation. The second experiment described in this chapter was performed on 3rd swine. It was necessary to remove the vitreous from the swine eyes prior to insertion of Spectralon. As the vitreous was removed a balanced salt solution was inserted into the eye to maintain the structural integrity of the globe, a standard practice in retinal surgery. The focus of this study was to compare retinal vessel oximetric measurements performed both before and after vitrectomy to quantify the effect of vitreous removal on oximetry measurements.

Chapter 7 focuses on the fundus spectroscopy of the live swine experiments. The spectral reflectance of fundus areas free of large vessels was measured. Spectralon was inserted both super and subretinally to isolate the spectral reflectance characterless of the bare fundus and to provide a model for quantifying the amount of stray light encountered when imaging the retina and retinal vessels.

The vitreous replacement fluid is known to be chemically different from vitreous, most notably an absence of ascorbic acid, and thus has different spectral transmit-

tance. Chapter 8 describes a series of experiments that were performed on enucleated vitreous and the vitreous replacement fluid to investigate these differences. Additionally, the role of ascorbic acid was measured.

Chapter 9 gives the authors opinions on what was learned in this work and in what directions this work should continue. Recommendations are made for modifications for future experiments using intravitreal illumination. Additionally, the potential benefits of straylight modeling of retinal vessel imaging using intravitreal illumination are discussed.

Chapter 2
Background and Physiology

Retinal oximetry with intravitreal illumination is an invasive modification to previous studies in retinal oximetry. Retinal oximetry is performed by spectral imaging of retinal veins and arteries and quantitatively measuring the color shift of the retinal vessels to calculate blood oxygen saturation. This chapter has a twofold purpose: One, describe the relevant structure of the retina and retinal blood flow; and two, provide the fundamentals of retinal oximetry and fundus reflectometry, including a review of past work in these two related subjects.

2.1 Anatomy and Physiology of the Retina

The first section describes the structure of the posterior region of the eye including the multi-layered retina. The second part describes retinal circulation and summarizes the results of several studies that have been performed to quantitatively measure retinal blood flow.

2.1.1 Anatomy of the Retina

The retina is a thin layer of brain tissue located at the posterior region of the eye globe and covers approximately 72% of the interior globe surface. [11] The retina converts incident light into biochemical then electrical signals that subsequently travel through the optic nerve to the brain for processing. Figure 2.1 is a schematic of the eye including all the ocular components from the anterior to posterior regions. The retina is included in the cutout from the figure. A full description of the anatomy of the eye is found in a number of excellent texts dedicated to the subject. [12, 13]

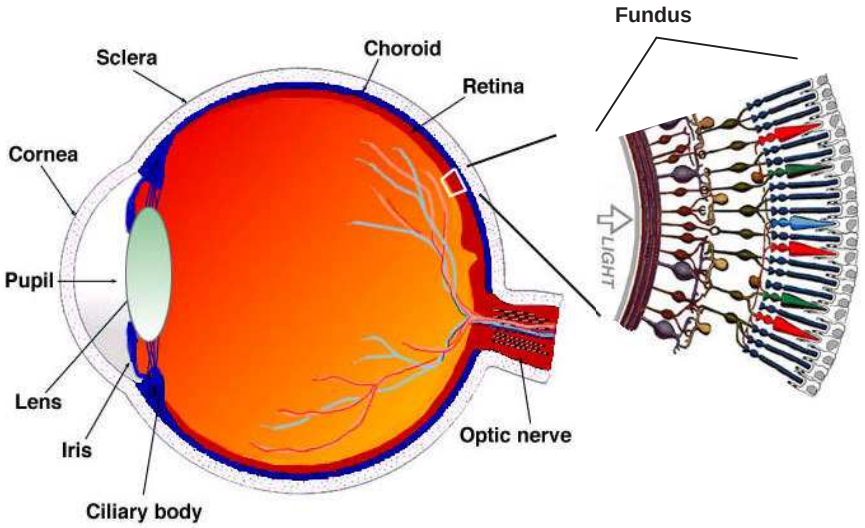

FIGURE 2.1. Schematic of the eye showing ocular surfaces. A posterior segment, including the retina, is cut-out and enlarged.

Figure 2.2 is the fundus view of the retina. The fundus image is the view seen by an ophthalmologist or optometrist examining an eye with an ophthalmoscope. The term fundus is a general medical term that refers to the back surface of an organ with an opening into a hollow interior. Applied to the eye, this term describes the view visible with an ophthalmoscope as the ocular fundus. Several features of the retina are identified in Figure 2.2 including the retinal vessels, macula, fovea, and optic nerve head (ONH). The optic nerve head is the white oval seen in Figure 2.2 and measures 2 x 1.5mm. From the ONH (also known as the optic disk) emanate the retinal vessels. The darker section approximately 2.5 disk diameters to the right of the ONH is the macula, the fovea is the center of the macula. The macular region is marked by a greater concentration of photoreceptors, especially the color sensitive cones. The highest concentration of photoreceptors occurs at the fovea.

Figure 2.3 illustrates the posterior section of the eye in more detail, detailing the sensory retina, the RPE, Bruch's membrane, the choroid, and the sclera. A retinal

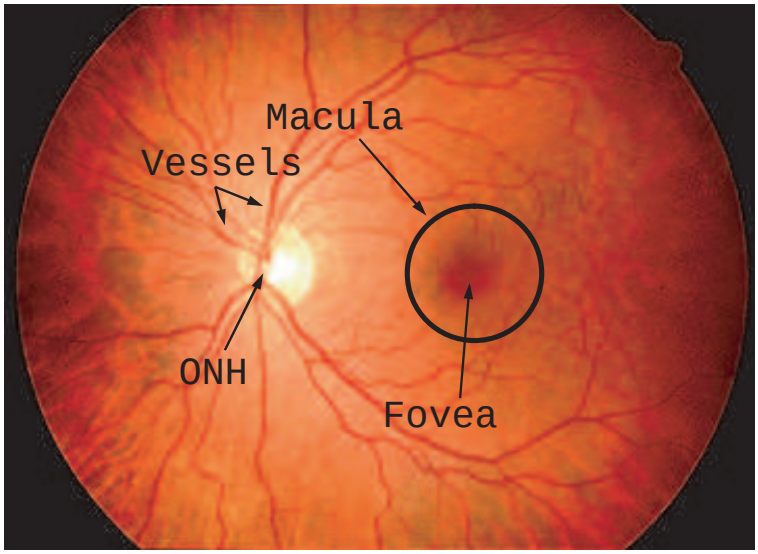

FIGURE 2.2. Typical retinal image taken with a fundus camera. This image was obtained from http://www.itd.umich.edu/ websvcs/projects/eyes/optic-fundus/arteries-veins.html

blood vessel is drawn in the sensory retinal layer. The thickness of the retina is approximately 0.5mm, thicker closer to the ONH. The retina is a layered organ that is commonly divided into two main parts, the sensory retina, which is further divided into 9 layers, and the retinal pigment epithelium (RPE). The RPE is made up of a singular layer of cuboidal cells that serves to separate the choroidal circulation from the retina and to transport nourishment to the photoreceptors. The RPE is pigmented with melanin that absorbs scattered light, preventing it from reaching the photoreceptors, and also scavenges free radicals. [14] Bruch's Membrane separates the RPE from the choroid, consists of five layers and is composed of mostly collagen and elastin proteins. [14] The choroid is a spongy layer that is heavily vascularized, providing 65-85% of the blood flow to the eye. [15, 16] The main purpose of the choroid is to provide nourishment to and remove waste from the outer retina. The final layer shown in Figure 2.3 is the sclera; the exterior surface of the eye (the white

part of the eye). It is a tough protective layer that is approximately 1-2mm thick and encircles the globe, merging with the cornea at the front of the eye.

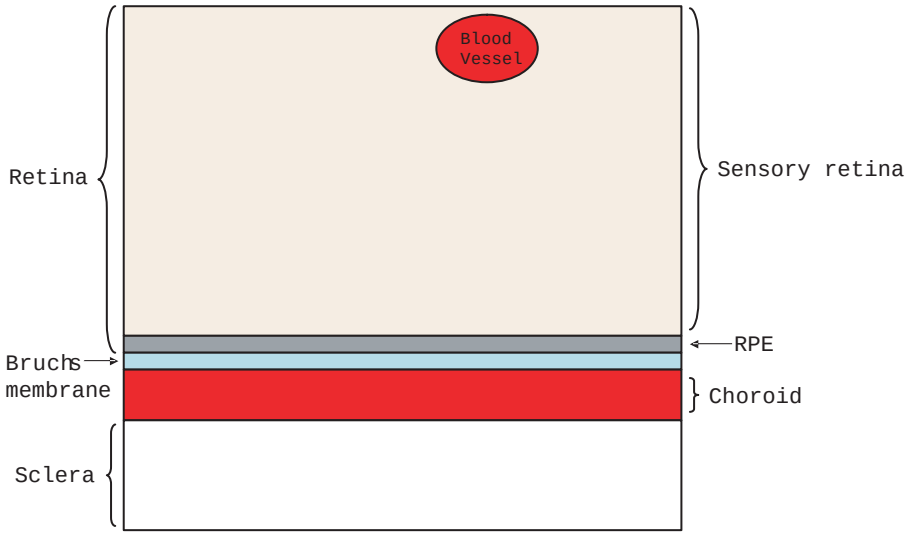

FIGURE 2.3. Layered structure of the posterior eye.

Figure 2.4 shows the sensory retinal layers. Beginning with the most anterior layer of the retina, the inner limiting membrane (ILM) is a transparent layer of cells that serves as a barrier layer between the vitreous and retina. The nerve fiber layer (NFL) is formed from the axons of ganglion cells. The NFL radiates out from the ONH and carries information from the retina to the brain. The NFL is a thickest at the ONH, measuring approximately 20-30 microns. Beneath the NFL is the ganglion cell layer (GCL). This layer is thickest at the macula, where it measures between 60-80 microns, although it is absent in the fovea. Posterior to the GCL is the inner plexiform layer (IPL) which varies in thickness from 18 and 36 microns, and is also absent in the fovea. The IPL is where bipolar, amacrine and ganglion cells form connections. Next is the inner nuclear layer (INL), with four types of nerve cells. It is heavily vascularized by retinal capillaries. The outer nuclear layer (ONL) follows the INL. Next is the outer plexiform layer (OPL). The outer limiting membrane (ILM)

separates the OPL from the final retinal layer, the photoreceptor layer.

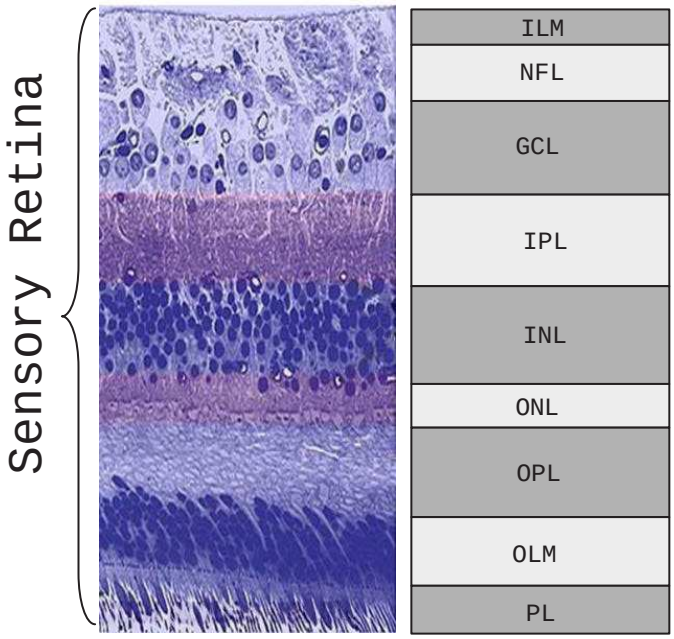

FIGURE 2.4. The sensory retina including the nine associated sub-layers.

2.1.2 Ocular Circulation

The retina depends on both the retinal vessels and choroid for sustenance. The retinal vascular system is shown in Figure 2.5. The central retinal artery and vein enter through the optic nerve and branch into four main vessel pairs to supply the four quadrants of the retina. Capillary free zones surround arterioles, which are small terminal branches of arteries that connect with capillaries. The ophthalmic artery, the first branch of the internal carotid artery, supplies most of the blood to the eye, and it branches off into the central retinal artery and to one to five posterior ciliary arteries. [17] The former supplies blood directly to the four main retinal arteries and the latter supplies the choroid, intraorbital optic nerve, and the retina. [15] Retinal vessels are largest near the ONH and taper as a function of length until the

capillary bed is reached. Characteristic size for the largest retinal arteries and veins is 130 and 160μm , respectively, and generally the size ratio for an artery/vein pair is 1.25 [18, 19]. The retinal vessels and capillary beds are found in the inner 2/3rds of the retina while the outer layers, including the photoreceptor layer are avascular, receiving oxygen and nutrients through the choroidal blood flow. [15] The fovea is the only region of the retina that is completely devoid of vessels, allowing light to reach the central photoreceptors without encountering any blood vessels.

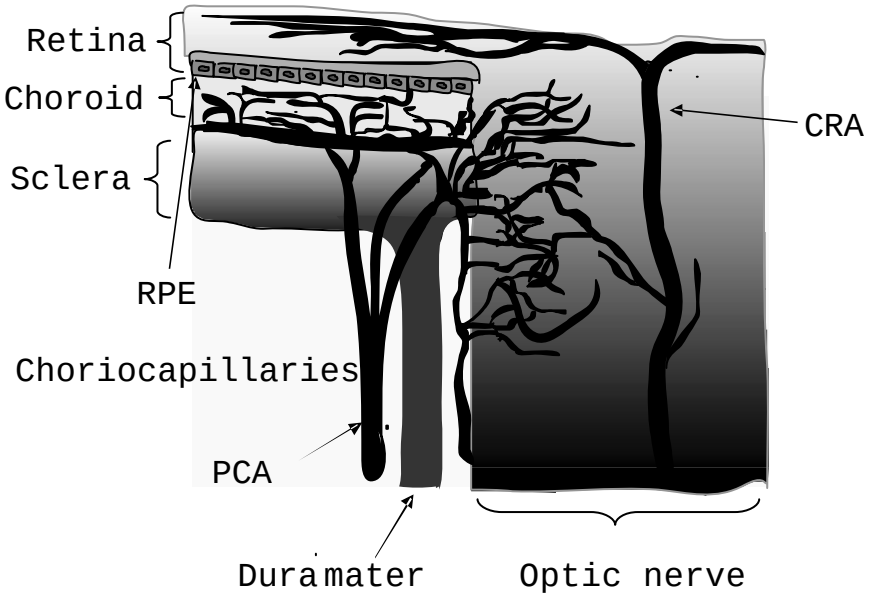

FIGURE 2.5. Vasculature of the posterior eye. The central retinal artery (CRA) and posterior ciliary artery (PCA) are branches of the internal carotid artery.

Techniques such as laser Doppler flowmetry have enabled the measurement of retinal blood flow in primates. Feke et. al. measured ocular blood flow using a Doppler flowmetry technique to measure the time averaged velocity of red blood cells (RBCs) flowing at discrete, selected cites in the retinal vasculature [19, 20]. Assuming Poiseuille flow in retinal vessels, they calculated total retinal blood flow as 80 $\pm$ 12 μl/min. Further, they show that blood flow in retinal vessels varies with the blood

vessel diameter D as D^4, as predicted by Poiseuille model [19]. Their results are in good agreement with results obtained by other investigators for the macaque monkey retina [19, 21].

2.1.3 Blood and the Transport of Oxygen

This section briefly describes the composition of blood and its role in the process of respiration. Towards that end, we begin with a description of blood and the mechanism by which it binds with oxygen molecules (hereafter, 0_2) and transports 0_2 to the muscles and tissues that require it.

Blood is a mixture of a watery medium called plasma and a few different suspended particles. Of these particles, the majority of the constituents are red blood cells (RBCs) which make up 32% to 52% of the blood volume. The fractional volume of red blood cells is called hematocrit. Red blood cells have the shape of a biconcave discoid and a characteristic size range of 5-12 μm outer diameter and and axial thickness of 2-3 μm. The remaining particles (in order of percent volume) are white blood cells, platelets, dissolved gasses, hormones, glucose, urea and an assortment of proteins. For the purposes of this dissertation, the only constituents that are considered to contribute to the oximetry measurement are the RBCs and plasma.

Oxygen is transported by blood from the lungs to all areas of the body in two forms: 0_2 dissolved in the blood plasma and 0_2 bound with hemoglobin to form oxyhemoglobin. Only 1.5% of the 0_2 needed by the body is delivered through the plasma, the remaining 98.5% of the required 0_2 is transported by hemoglobin. Red blood cells contain approximately 250 million hemoglobin molecules. Each hemoglobin molecule can transport (bind with) four 0_2 molecules. Hemoglobin binds readily to 0_2 molecules to form oxyhemoglobin and is the mechanism for oxygen transport. Upon reaching tissues that require 0_2, oxyhemoglobin gives up the 0_2 molecule to become deoxyhemoglobin. The hemoglobin exhibits a binding characteristic called cooperative bind-

ing: when oxygen binds to hemoglobin, other oxygen molecules bind more readily. Hemoglobin's affinity for 0_2 increases as saturation increases. Saturation is defined as the fraction of 0_2 binding sites on the hemoglobin molecules that are filled with 0_2. In equation form the saturation s is give as:

$$s = \frac{c_{HbO_2}}{c_{HbO_2} + c_{Hb}} = \frac{c_{HbO_2}}{c_{Hb_{total}}}, \tag{2.1}$$

where c_{HbO_2} and c_{Hb} represent the relative concentrations of oxyhemoglobin and hemoglobin, respectively.

Oxygen saturation is a ratio of the amount of oxygen bound to hemoglobin to the oxygen carrying capacity of the hemoglobin molecules. Total oxygen carrying capacity is determined by the saturation and the amount of hemoglobin present in the blood. The change of shape and structure of hemoglobin as it binds with oxygen and becomes oxyhemoglobin leads to a change in the absorption spectrum. As will be seen Section 2.2.1, exploiting this characteristic spectral shift is fundamental to retinal oxygen saturation measurements.

2.2 Retinal Oximetry

The fundamentals of blood oxygen saturation measurements using retinal oximetry are presented in this section. Following is a summary of the evolution of retinal oximetric techniques and summaries of the contributions by the many researchers in the field.

2.2.1 Fundamentals of Retinal Oximetry

Retinal oximetry is a technique for measuring the oxygen saturation of retinal arteries, $S_{ra}0_2$ and retinal veins, $S_{rv}0_2$. Hemoglobin undergoes a significant red color shift as oxygen saturation changes from $S0_2 = 0\%$ (deoxyhemoglobin) to $S0_2 = 100\%$ (oxyhemoglobin). In retinal oximetry, incident light of known spectral content transmits

through, or reflects from a retinal vessel, causing wavelength dependent extinction (defined as losses due to absorption and scattering) to the spectra depending on the oxygen saturation of the blood and the optical properties of the other components of the vessel. The light collected by a retinal oximeter comes from three primary paths: light transmitted through the vessel, light reflected from the blood column in the vessel, and light scattered from a variety of surfaces, especially from the RBCs. The scattered component constitutes noise in the system and attempts have been made to limit its influence. The mathematical model chosen to model a particular retinal oximeter must be chosen wisely to correctly weight the influence of the spectral contribution from each of these pathlengths. Most retinal oximetry techniques are based on the measurement of the light transmitted through a quantity of blood. Intravitreal illumination retinal oximetry, the focus of this dissertation, is modelled as transmission oximetry; therefore the review provide in this section deals only with transmission oximetry.

Light extinction: Purely absorptive medium A fundamental parameter governing the behavior of light as it passes through a medium is the complex index of refraction, written as,

$$\hat{n}(\lambda) = n(\lambda) + i\kappa(\lambda), \tag{2.2}$$

where λ denotes wavelength, n is the real part of $\hat{n}$ and κ is the imaginary part. The real part, $n(\lambda)$ is unitless measure of the speed of light in a medium as compared to the speed of light in a vacuum and governs the laws of reflection and refraction of the light at an interface between two materials of differing indices of refraction. The absorption of light is described by the imaginary part of the complex index of refraction, κ. Scattering losses are influenced by $n(\lambda)$ and κ.

Lambert's law provides a model for the absorption of light as it pass through a linear, homogeneous, and isotropic medium and is written as,

$$I(\lambda) = I_0 * e^{-\alpha(\lambda)*l}, \tag{2.3}$$

where I is the transmitted intensity, I_0 is the intensity of the incident light, l is the path length and α is known as the absorption coefficient. α is related to the complex index of refraction by

$$\alpha = \frac{2\omega\kappa}{c}, \tag{2.4}$$

where ω is the angular frequency of the light and c is the speed of light in a vacuum. Expressing Lambert's law as transmittance, T, yields,

$$T(\lambda) = \frac{I(\lambda)}{I_0(\lambda)} = e^{-\alpha(\lambda)*l}. \tag{2.5}$$

In spectrometry, the the transmittance of a material is simplified using a base 10 log, which eliminates the exponential dependence. Transmittance written in this manner is

$$T(\lambda) = 10^{-\frac{\alpha(\lambda)}{\ln(10)}*l} = 10^{-a*l} \tag{2.6}$$

Transmittance can be modelled in a fashion more amenable to blood analysis by incorporating Beer's law, which states that the absorption of incident light is proportional to the concentration of the absorbing medium. The extinction coefficient $a = \frac{\alpha}{\ln(10)}$ can be rewritten as the product of the millimolar extinction coefficient ϵ of the absorber and the concentration of absorbing medium, c (in our case, hemoglobin concentration).

$$D = -log(T) = \varepsilon * c * l, \tag{2.7}$$

where the D is defined as optical density. This equation, known as the Lambert-Beer law, can be generalized for two or more absorbing and non interacting substances as

$$D = \varepsilon_1 * c_1 * l + \varepsilon_2 * c_2 * l + ... + \varepsilon_n * c_n * l \tag{2.8}$$

Light extinction: An absorptive and scattering medium Whole human blood is not a linear, homogeneous, and isotropic medium due to inhomogeneities in the blood (primarily RBCs). The inclusion for a single scatterer, defined as light scattering once from a particular inhomogeneity and then entering the detection system, is fairly easy to model. For the case of multiple scattering, the mathematical description gets more complicated.

First, for the case of a single scattering episode, consideration of a single scatterer modifies the absorption coefficient to look like

$$\acute{\alpha} = \alpha(\lambda) + \alpha_{scatter}(\lambda), \tag{2.9}$$

where α is given by 2.4 and $\alpha_{scatter}$ is the scatter coefficient. The transmittance of the absorbing/single scattering medium including the scatter coefficient is written as

$$T(\lambda) = \frac{I(\lambda)}{I_0(\lambda)} = e^{-[\alpha(\lambda) * l + \alpha_{scatter}(\lambda)]}. \tag{2.10}$$

In reality, whole blood contains a concentration of RBCs that act as multiple scatterers, i.e., light impinges on multiple RBCs in succession. Multiple scatter is a function of particle size, particle concentration, and sample thickness. The precise definition of multiple scattering is the subject of some debate, but the definition above is used for the purposes of this dissertation. The study of multiple scatter is an subject of much research and will not be treated in detail in this dissertation. We present only the results arrived at by workers in the field that are directly applicable to retinal oximetry. The interested reader is urged to consult the references provided below for further study.

Twersky developed an expression for the transmittance of light through a multiply scattering and absorbing medium (such as blood). [22, 23] Twersky's expression was derived by calculating the multiply scattered field distribution due to a semi infinite ensemble of scatterers interacting with a plane wave. The expression takes the form:

$$T(\lambda) = e^{-N\alpha(\lambda)*l}[e^{-\beta(\lambda)*l} + q(\theta)(1 - e^{-\beta(\lambda)*l})] = T_a(\lambda) * T_s(\lambda), \tag{2.11}$$

where T_a corresponds to the term outside the brackets and is just the extinction due to normal absorption, and T_s corresponds to the bracketed term and represents transmittance due to scatter. The bracketed portion of the equation contains both a loss term (the first term) and a gain term (second term in brackets). The gain results from forward scattering of light into the optical detection system. The other two terms in 2.11, $\beta(\lambda)$ and $q(\theta)$, represent a measure of the scattering transmittance of a single scatterer and a measure of the light scattered into the detector's acceptance cone by a single particle, respectively. [22, 23] While Twersky's work provides a rigorous treatment and mathematic model of the multi scattering phenomenon, application of the theory directly to retinal oximetry has proven difficult. Most workers have applied extensive simplifications to the model, modified the blood sample so as to remove the scattering contribution (hemolyzed RBCs), or empirically determined scattered light contribution by calibration methods.

Transmission Retinal Oximetry Transmission oximetry is based on the measurement of the wavelength dependent absorption of light as it traverses a quantity of blood. The preferential spectral extinction of light as a function of wavelength is different for oxygenated and deoxygenate blood based primarily on the changing structure of hemoglobin as it binds with 0_2 and becomes oxyhemoglobin. A series of measurements were made in 1970 on the absorption spectrum of hemolyzed blood. [1] Hemolyzed blood has been stripped of its RBC structure resulting in pure hemoglobin or oxyhemoglobin. The absorption of hemolyzed blood is due only to hemoglobin absorption, effectively removing the effects of scattering from RBCs. The plots shown in Figure 2.6 depict the millimolar extinction coefficients of oxyhemoglobin and deoxyhemoglobin, where extinction coefficients are defined as the optical density of an absorbing substance in a concentration of 1mmol/liter, measured with a light path of

1cm. [1] The dimensions of the millimolar extinction coefficients are $\frac{cm^2}{\mu mole}$.

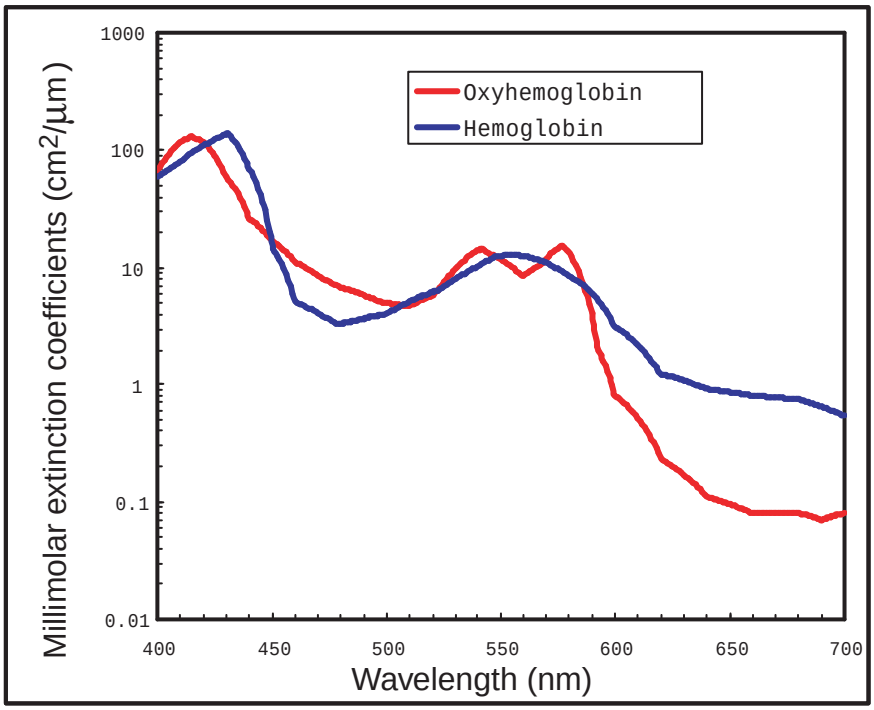

FIGURE 2.6. Millimolar extinction coefficients of hemoglobin and oxyhemoglobin. [1] These values correspond to the optical density per millimeter calculated at the typical hemoglobin concentration of 15g/ml.

Points in Figure 2.6 where the curves intersect are termed isobestic wavelengths, spectroscopic wavelengths at which the absorbance of two substances, one of which can be converted into the other, is the same. There are four intermediate states of hemoglobin and there is evidence that there are no true isobestics. [24] Retinal oximetry techniques typically use at least one isobestic wavelength as part of the measurement process. At least one measurement wavelength must be chosen such that ε_{Hb} - ε_{HbO_2} is large. Smith provides a discussion of optimal oximetric wavelength choices for use in retinal oximetry. [25]

Rewriting Equation 2.8 specifically for blood analysis is accomplished by inserting the millimolar extinction coefficients and relative concentrations of oxyhemoglobin

and hemoglobin as shown below.

$$D = \varepsilon_{Hb} * c_{Hb} * l + \varepsilon_{HbO_2} * c_{HbO_2} * l \tag{2.12}$$

Incorporating Equation 2.1 into Equation 2.8 yields the fundamental equation for use in performing spectroscopic oximetry measurements.

$$D = [(1 - s) * \varepsilon_{Hb}(\lambda) + s * \varepsilon_{HbO_2}(\lambda)] * l * c_{Tot} \tag{2.13}$$

Measuring the OD at two wavelengths allows the dependency on concentration and pathlength to be removed. The saturation based on two wavelength techniques results in a very simple formula for oxygen saturation as given in Equation 2.14. This formulation assumes a strict adherence to the linear, homogenous, isotropic requirements demanded by the Lambert Beer law. This equation is only accurate for hemolyzed blood samples.

$$s = \frac{D(\lambda_1) * \varepsilon_{Hb}(\lambda_2) - D(\lambda_2) * \varepsilon_{Hb}(\lambda_1)}{D(\lambda_2)(\varepsilon_{HbO_2}(\lambda_1) - \varepsilon_{Hb}(\lambda_1)) + D(\lambda_1)(\varepsilon_{Hb}(\lambda_2) - \varepsilon_{HbO_2}(\lambda_2))} \tag{2.14}$$

To account for scattering, it is necessary to introduce an extra term into Equation 2.13. Many variations to this approach have been offered over the years, ranging in both simplicity and effectiveness. [26, 27, 28] The extra scattering term introduced in Equation 2.13 adds another unknown to the equation, necessitating the introduction of at least a third measurement wavelength. Three wavelength algorithms allow for compensation of the contribution to the measured OD signal for scatter. Algorithms of this nature have been used to calculate oxygen saturation with varying degrees of success. For the oximetry measurements made in this dissertation, a different approach was taken: multiple illumination wavelengths in the spectral range of 460-590nm were used and the resulting transmittance spectra was fitted to a nonlinear model based on a modified Lambert Beer law, taking into account both scatter and straylight effects. Details of this technique are provided in Chapter 5.

2.2.2 Prior Work on Retinal Oximetry

The first published study of retinal oximetry was performed in 1962 by Hickam, Frayser, and Ross [3]. The instrument designed by Hickam was a dual wavelength imager. Retinal images were obtained at two narrow wavelength bands and recorded on photographic film. Microdensitometry techniques were used to analyze the film and determine OD across vessels. Hickam determined that the fraction of the light reflected from the blood in the vessel was relatively small by experiments conducted on a model vessel. He therefore concluded that the light collected by his system consisted primarily of double pass light; the light traversed the vessel and reflected from the underlying fundus back through the vessel and into the camera. Although they were able to demonstrate the concept, numerous difficulties resulted from using photographic measurements and from the fact that the collected light was an unknown mixture of double and single pass light.

Cohen and Laing refined Hickam's technique with another dual wavelength imager dubbed the Photographic Eye Oximeter (PEO). [29, 30] They also employed narrow wavelength light sources and microdensitometry techniques in their analysis of retinal images. The PEO attempted to account for scattered light from the blood column by using Twersky's theory. Resulting oximetry measurements yielded results accurate to around 5% for oxygen saturations above 90%, but suffered large errors at lower saturations.

Delori developed the first scanning retinal oximeters illuminating with multiple wavelengths obtained with narrow band interference filters [31]. Delori replaced the microdensitometry techniques with a photodetector, and a scanning mirror was introduced into the arm of a fundus camera to image only a single line across a retinal vessel. OD profiles were obtained at three wavelengths in the range of 569-586nm provided by a filtered tungsten halogen lamp. Delori carefully characterized the spectroscopic and autofluorescing properties of the fundus and developed improved

algorithms for saturation calculations. [32] Despite several years of effort, consistent accuracy better than 10% was not achieved, in part due to the difficulties associated with handling the glint caused by the vessel apex reflection.

Another scanning laser technique was introduced to retinal Oximetry by Denninghoff, Smith, and Chipman who built a series of three noninvasive, transcorneal Eye Oximeters [25, 33, 34, 35, 36]. However, the vessel reflex causes the vessel transmission profile to appear W-shaped rather than the expected (parabolic) U-shaped. Smith tried several algorithms and optical techniques to remove this central vessel reflex including (1) extrapolated the intensity into the reflex region, (2) measured on the vessel beside the reflex, (3) illuminating with polarized light and detected through a crossed polarizer, and (4) a confocal system with an annular aperture in the detection path to eliminate directly backscattered light and enhance the laterally scattered light component. Only modest improvements in accuracy were observed. The crossed polarizers reduced the light level by about 88% and although diminished, a significant vessel reflex remained.

Recently, several groups have constructed spectrometers and spectrographs for retinal oximetry. Schweitzer and Hammer, *et.al.* used a diffraction grating to acquire a spectrum of a line from 400 to 700 nm in 3 nm steps and then applied multiwavelength curve fitting technique for saturation determination [27]. Another spectrograph with a scanning line measurement was developed by Tiedeman, Beech, et. al. who also studied the effects of retinal reflectivity on retinal oximetry measurements [37, 38].

2.3 Fundus Reflectometry

Clinical diagnosis of ocular disease by observation of the ocular fundus began with the invention of the ophthalmoscope in 1850. Introduction of spectrometric analysis of the ocular fundus provided a means of quantitatively recording the appearance of the fundus, leading to *in vivo* reflectometry being used to describe the physiological

state of the fundus and to observe pathologic processes. Fundus reflectometry is used to measure the concentrations of ocular pigments such as melanin, xanthophyll, and hemoglobin in the retinal pigment epithelium, choroid and retina. Detailed characterization of the reflectance properties of the fundus is of paramount importance in techniques such as fundus photography, photocoagulation, fluorescein angiography and retinal oximetry.

2.3.1 Fundamentals of Fundus Reflectometry

Measurement of the spectral reflectance of the fundus requires the illumination of the fundus with light of known spectral content and the subsequent imaging of the reflect light by a spectrally selective method. Many versions of reflectometers have been employed for this purpose, ranging from reflectometers that gather spectral reflectance information from a small test area on the fundus, to imaging reflectometers that provide both spatial and spectral distribution of reflected light. The latter type of reflectometers employ either a fundus photography approach in the gathering of fundus reflectance (i.e., imaging the retina at multiple wavelengths onto photographic film or CCD array) or a scanning laser ophthalmoscope(SLO)using multiple lasers. SLO techniques use a laser beam as the illumination source and move the beam in a raster pattern over the retina at high rates of speed. Use of multiple lasers provides spectral information.

The reflection from the fundus including the retina, RPE, choroid and sclera combine to contribute form the spectral fundus reflectance. The sensory retina is essentially spectrally transparent, the only pigments contributing to a spectral reflectance signature are the hemoglobin and oxyhemoglobin molecules found in the retinal vessels and capillary beds. The RPE and choroid are heavily pigmented with melanin and xanthophyll, and the choroid contains a large amount of blood that contributes to the spectral reflectance signature. The reflectance from the sclera is essentially

specular and spectrally flat.

2.3.2 Prior Work on Fundus Reflectometry

Several studies of the spectral reflectance properties of the fundus have been performed. [39, 40, 32, 41, 42, 43, 44, 45] Knighton and Berendschot provide excellent reviews on fundus reflectance studies. [46, 47]

Van Norren and Tiemeijer measured the reflectance from the foveal and peripheral fundus and mathematically modeled the fundus. [40] They used a modified Zeiss fundus camera equipped with a photomultiplier detector. Their reflectance model was based on the Lambert-Beer law and used two reflective and four absorbing layers to describe the fundus. Their model provided stable results, but the results did not correspond with known values from psychophysical or in vitro measurements. The shortcomings of this model have as a basis the disregard of the model of scattering effects.

Delori and Pflibsen performed in vivo spectral reflectance measurements on human subjects with a wide range of fundus pigmentation and applied the model of van Norren and Tiemeijer to the resulting data. [32] Delori used a modified Zeis fundus camera in which the retinal image was focused onto an optical fiber placed at a plane conjugate to the entrance pupil. The output of the fiber served as the entrance slit to a monochromator. Delori succeeded in measuring the spectral reflectance in the range of 4000-900nm at a spectral resolution of 7.5nm. Delori and Pflibsen also developed an alternate, more complex model that consisted of a scleral reflector, an absorbing-scattering layer meant to simulate the choroid, a blood layer, a melanin layer for the retinal pigment epithelium, and a spectrally flat reflector. They applied the equations of Kubelka and Munk to their data and achieved a better fit to measured spectra. [32] Kubelka and Munk introduced a two-constant theory for the description of the reflectance properties of a material; the absorption coefficient and the scattering

coefficient. [48] Delori's adaptation of the model of Kubelka and Munk treats the choroid as a diffuse absorbing scatterer backed by a reflecting sclera. [32]

Hammer *et al.* performed high spectral resolution studies with a imaging spectroscopy at high spatial resolution along a bar-shaped field on the retina. [42, 41] The instrument they used was a modified Zeis fundus camera to image the fundus onto a spectrograph. Retinal images were obtained for the 400-710nm range at a spectral resolution of 2nm. They developed a four layer model to describe the reflectance of the ocular fundus: the retina containing macular pigment in the foveal region, the RPE pigmented with melanin, the choroid containing blood and melanin and the sclera. [42] The approach used for this model was the adding-doubling method as an approximate solution of the radiation transport equation for the reflectance.

Simultaneous measurement of foveal spectral reflectance and cone-photoreceptor directionality was achieved by Zagers. *et al.* Their instrument was equipped for measurement of the foveal spectral reflectance versus position on a horizontal section of the pupil plane. Spectral reflectance was calculate using a spectrograph with its entrance slit conjugate to the pupil plane of a human eye. This instrument sampled a 1.9° spot on the retina in 1s, providing spectral and spatial profile data in one image by use of a dispersive element that spread a bar shaped retinal image across a CCD.

2.4 Summary

This chapter has presented the anatomical features of the retina and retinal blood circulation. The fundamentals of retinal oximetry and fundus reflectometry, complete with a summary of the pertinent history of work performed in these two related fields, is also included. The research presented in this dissertation builds on this previous work and supplies additional contributions to the fields of study using a completely new illumination system. Retinal oximetry and fundus reflectance are not mature technologies. Remaining areas for future research include careful modelling of light

paths and characterization of glints from all ocular structures.

Chapter 3

Imaging Spectroscopy of the Enucleated Swine Eye

We present the results of spectroscopic analysis of the fundus of enucleated (i.e, excised postmortem) swine eyes. Intravitreal illumination of the swine fundus with a scanning monochromator was used to obtain spectral images of retinal vessels filled with saline solution and blood of various oxygen saturation levels. In addition, fundus reflectance measurements on areas free of major blood vessels were performed. Vessel optical density profiles were constructed from multispectral data sets. The spectral characteristics of oxyhemoglobin and deoxyhemoglobin are evident in all data. Intravitreal illumination resulted in minimal extraneous reflections from the anterior portion of the eye. Because of advantages that are detailed in this and other chapters, retinal spectroscopy with intraocular illumination may be of great value despite being highly invasive.

3.1 Experimental Methods

Fundus spectroscopy is performed on two American Yorkshire porcine eyes. Each experiment used a different CCD camera; otherwise the same experimental protocol is used for both experiments.

3.1.1 Optical System

Light from a scanning monochromator (Oriel Spectral Luminator) is coupled into a fiber optic intraocular illuminator (Alcon Laboratories) which is inserted into the vitreous to illuminate the retina. The monochromator is operated at a spectral resolution of 10 nm. The output power from the fiber optic intraocular illuminator

is approximately 100 microwatts per 5nm wavelength band. Light is reflected from the fundus and passes through the pupil and cornea. The reflected light is focused onto a CCD camera using a 3.3X macro zoom lens (Edmund Scientific 56-524). Two cameras are used for the experiments: for eye 1, the camera is a Basler 600f series digital monochrome camera (640 by 480 pixels), and for eye 2, a Dalsa Ca-D1 12 bit high speed digital monochrome camera (120 by 120 pixels). The eye and illumination system are immobilized during the measurement process resulting in negligible image registration problems among the monochromatic images comprising the spectral image set. Figure 3.1 shows an illustration of the optical system.

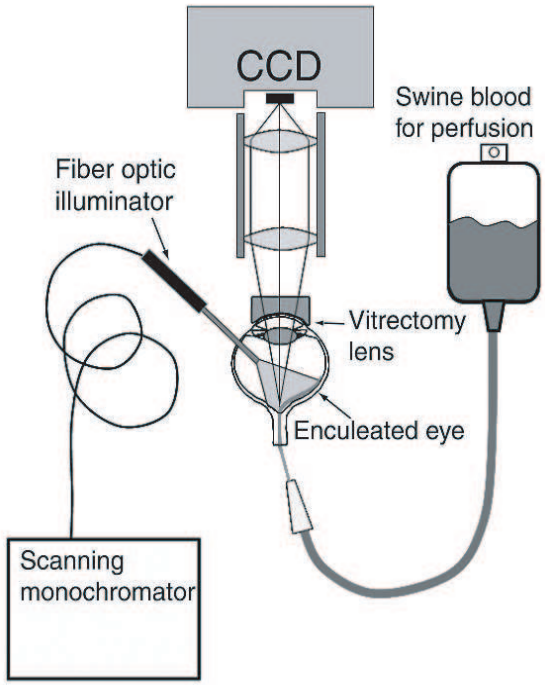

FIGURE 3.1. Schematic of the optical system.

A custom optomechanical mount with a threaded ball joint is used to hold the enucleated eye during imaging as shown in Figure 3.2. A similar mount is used to hold the fiber optic intraocular illuminator. The "ball and socket" movement of these

mounts allows for a continuous range of illumination and measurement angles. The fiber optic intraocular illuminator is approximately 2mm in diameter and is encased in a stainless steel sheath. The upper portion has a plastic "handle" approximately 8mm in diameter which is mounted to our fiber optic illuminator mount.

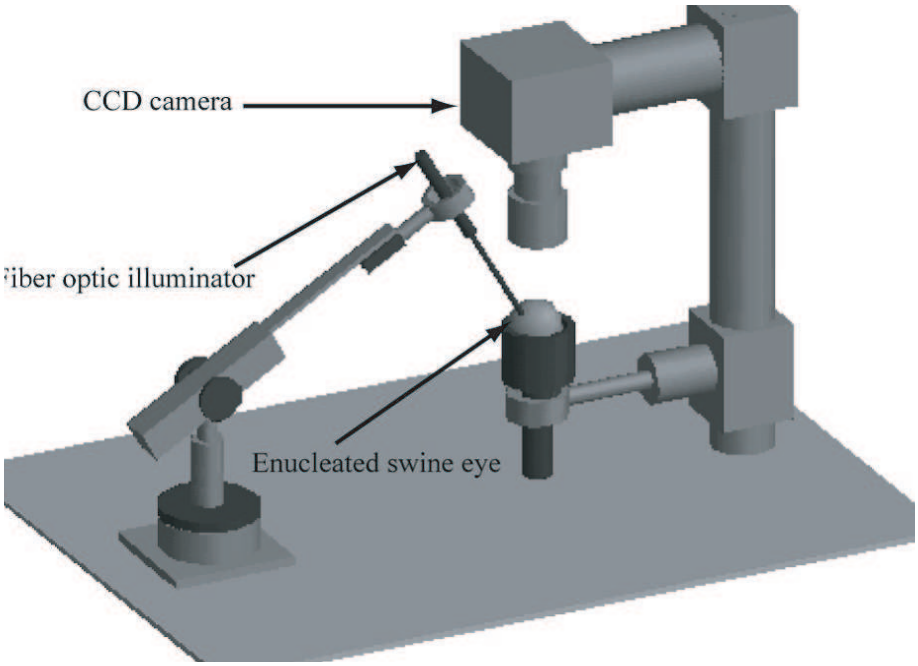

FIGURE 3.2. Custom mounts for holding enucleated eye and fiber optic illuminator for imaging.

3.1.2 Eye Preparation

American Yorkshire swine eyes and swine blood are obtained from the University of Arizona Meat Sciences Laboratory. Experiments are performed 6-12 hours after the death of the animals.

The swine eye is mounted in a custom apparatus and is secured with silk or nylon suture. Figure 3.3 shows the mounted eye. A 4mm infusion cannulum is placed through the pars plana and is sutured into place. The infusion cannulum is

attached to a balanced salt solution (BSS: Alcon Laboratories) gravity feed system to maintain the intra-ocular pressure (IOP) at levels comparable to in vivo conditions. Cannulation of the central retinal artery is performed next. A 24 gauge catheter is inserted into the central retinal artery and sutured into place. Figure 3.4 shows a picture of the cannulated eye.

A surgical contact lens ring (Bausch and Lomb) is sutured into place and a vitrectomy lens (Bausch Lomb: F36202.08) is placed onto the cornea using a viscoelastic coupling agent. The vitrectomy lens improves imaging of the fundus by removing the power and aberrations of the cornea.

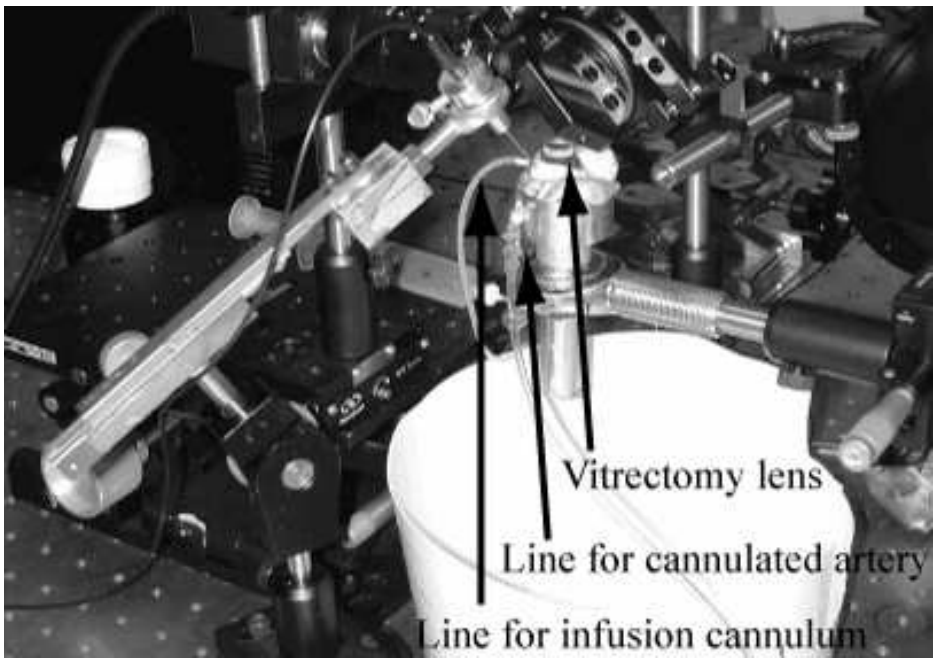

FIGURE 3.3. Photograph of a cannulated eye mounted in the eye holder.

3.1.3 Intravitreal Illumination

The fiber optic illuminator is inserted through an incision in the pars plana into the vitreous chamber and is used to illuminate the fundus at an approximate angle of

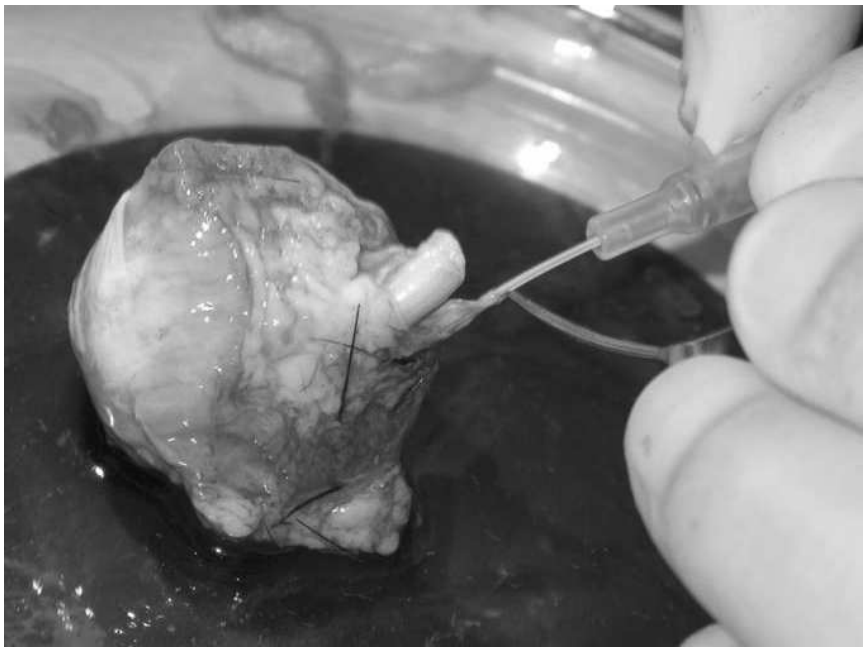

FIGURE 3.4. This is a photograph of a cannulated eye. The 24 gauge catheter is inserted into the central retinal artery.

45 from one side. The side illumination removes the central glint along the tops of retinal vessels common in fundus camera images. As the side illumination directly illuminates the retinal pigment epithelium (RPE) directly behind the vessel, the RPE directly under the vessel is not shadowed by the vessel. Instead the shadow of the blood column on the RPE is translated to the far side of the vessel (Figure 3.5). Four light paths result from this type of illumination: (1) light reflects from the background fundus and into the imaging system (S_1), (2) light reflects from the fundus and traverses the vessel in single pass (S_2), (3) light traverses the vessel in single pass and reflects from the fundus into the imaging system (S_3), and light that is laterally scattered from the blood column and into the imaging system (S_4).

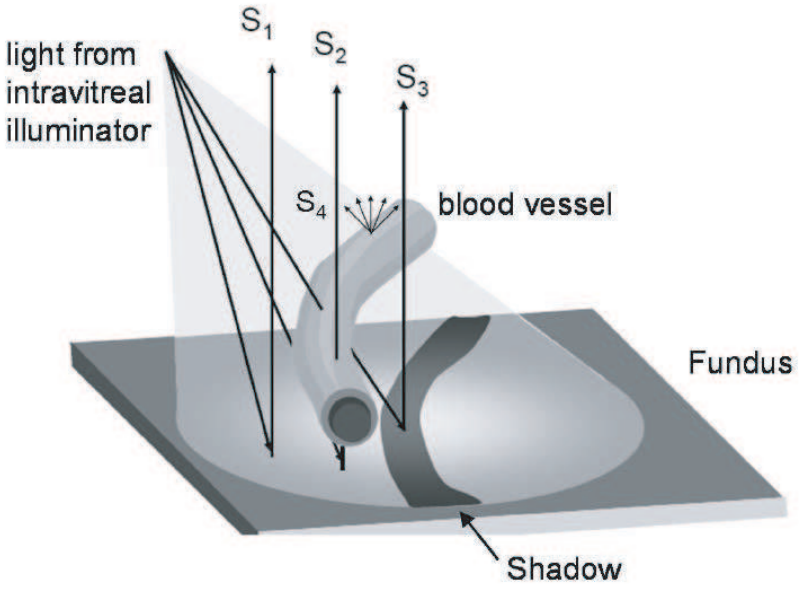

FIGURE 3.5. The intravitreal illumination technique eliminates the extraneous reflections, or glint, caused by the anterior components of the eye. The three light paths are differentiated in the illustration above and are assigned the monikers S_1, S_2, and S_3. S_1 corresponds to "background" fundus reflectance only. S_2 is light that is collected after traversing the vessel in single pass. S_3 is composed of light from the shadow region. This light has traversed the vessel once and reflected off the fundus background once. S_4 is light that is laterally scattered from the blood column.

3.1.4 Data collection: Perfusion experiments

The mounted and cannulated eye is positioned under the camera. The camera is focused through the cornea and lens onto the fundus with the illumination wavelength set to 520 nm. The eye is translated until a number of large blood vessels are in the camera's field of view. Balanced saline solution (BSS) is then infused into the central retinal artery and through the retinal blood vessels by means of constant pressure applied to a syringe. Vessels visibly clear of blood. 31 monochromatic images are recorded at the wavelengths given in Table 3.1. The entire multi-spectral image set

TABLE 3.1. Illumination wavelengths for spectral image sets.

Wavelength Range	**Spectral Stepsize**
440nm-540nm	20nm
543nm-600nm	3nm
620nm-700nm	20nm

is recorded within 5 minutes, without any movement of the camera or eye other than slight motion caused by the fluid flow through the vessels.

Swine blood that is collected at the time of slaughter and heparinized (10mL/ 1.5L of blood) is then infused into the vessels via the central retinal artery. Prior to infusion of the blood, analysis of the swine blood is performed using the ISTAT Personal Clinical Analyzer (Heska Corporation). This blood is essentially deoxygenated (measured oxygen saturation is 26% and 39% for Eye 1 and Eye 2, respectively). After pumping the blood through the retinal vessels, spectral image sets are taken of retinal vessels.

A separate quantity of swine blood is oxygenated. Analysis with the ISTAT PCA is performed on this blood to verify that the saturation is greater than 95%. The saturated blood is then forced into the vessels and spectral image sets are obtained at the wavelengths given in Table 3.1.

This data collection process is used for spectral images collected with both the Basler 600f series and the Dalsa Ca-D1.

3.1.5 Calibration and Data analysis

Upon completion of the data collection process, a calibration image set is measured at the wavelengths given in Table 3.1. A Spectralon lined integrating sphere is illuminated by the fiber optic illuminator and the exit pupil of the sphere is imaged by the camera system. This calibration set is used to correct for the spectral intensity

variation in the illuminating source and the spectral response of each CCD.

Mathematica is used to perform image processing of the image sets Each spectral image set is corrected for variation in the spectral response of the CCD and the spectral power variation in the illumination system using the calibration image sets. Normalized spectra are built from a region of interest in an image by compiling the respective pixel intensity values from each of the monochromatic images comprising the spectral image set. Spectral data are normalized to the brightest pixel in the calibration corrected image set. Software allows construction of both the spectrum from a single pixel intensity in the region of interest and an average spectrum of pixel intensities surrounding the point of interest. Averaging can be performed along a line, a rectangle or a square, depending on the shape of the region of interest. For example, to calculate the transmittance of a section of a retinal vessel, the most appropriate averaging scheme is that of a line average. Similarly, analysis of a vessel free region on the fundus requires an average over a square or a rectangle.

Of particular interest in this study is the transmission of the retinal vessels. The intravitreal illumination technique allows this quantity to be determined with little ambiguity as to the light path involved. The majority of the light contained in S_2 (Figure 3.5) traversed the retinal vessel in single pass. The contribution from S_4 adds to and is not separable from the S_2 signal. This contribution is believed to be small and is thus not modeled. [3] Therefore, vessel transmittance is calculated by dividing the background (S_1) out of the spectrum obtained through a given vessel, or S_2. In equation form this is given as:

$$T(\lambda) = \frac{S_2(\lambda)}{S_1(\lambda)} \tag{3.1}$$

where S_1 and S_2 are as given in Figure 5, and T_v is the vessel transmittance.

Averaged spectra are created for retinal vessels that are perfused with BSS, deoxygenated blood (saturation = 20-40%), and oxygenated blood (saturation = 95%). For

TABLE 3.2. Experimental conditions for perfusion experiments.

	Deoxygenated Blood Saturation Level	**Oxygenated Blood Saturation Level**	**Camera**
Eye 1	39%	100%	Basler 600f
Eye 2	25%	95%	Dalsa Ca-D1

these same perfusion conditions, averages spectra for vessel free areas of the fundus are constructed.

3.2 Results

Table 3.2 lists the SO_2 levels for the blood infused into the two porcine eyes and the camera used. Figure 3.6 contains a few monochromatic retinal images obtained with the Dalsa Ca-D1. In the 660nm image, the large vessels appear brighter than the surrounding tissue to scattering from red blood cells. The dark spot near the right margin of the four images is appears to have been caused by hemorrhages of smaller capillaries during blood infusion.

Note the absence of retinal vessel glints resulting from the intravitreal illumination. The absence of glint is demonstrated in Figure 3.7, which shows a series of vessel intensity profiles across a single vein at illumination wavelengths of 460, 520, 555, 582, and 600 nm. The glints in standard fundus photographs (transcorneal illumination) result in a local maximum near the center of vessel intensity profiles. These intravitreal illuminated intensity profiles have a single clearly defined minima associated with the retinal vessel. The region to the right of the vessel is the vessel shadow, S_3 which is noticeably darker than the foreground S_1.

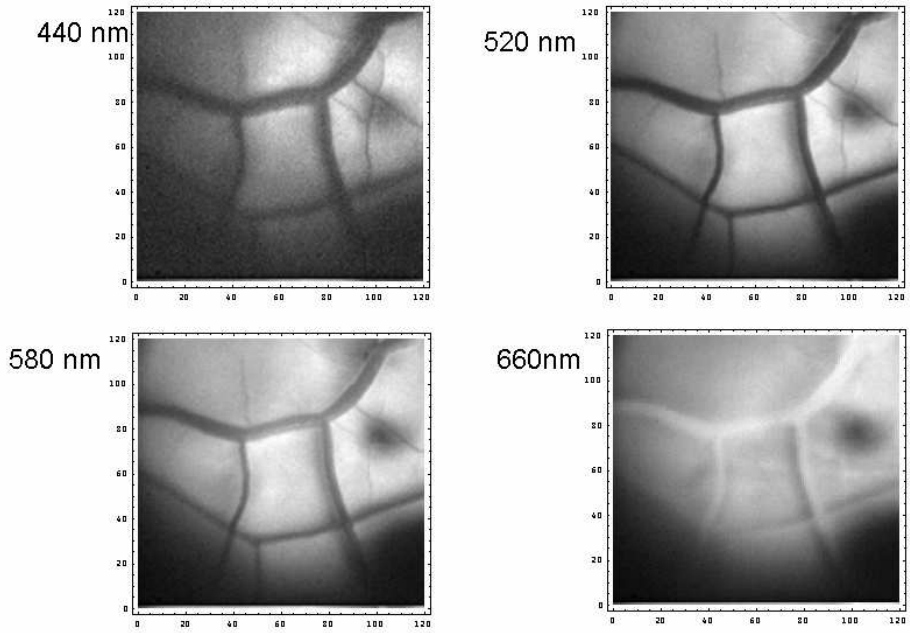

FIGURE 3.6. Monochromatic images taken from a spectral image set. The images were obtained using the Dalsa Ca-D1.

3.2.1 Spectral analysis of retinal vessels

Results from eye one and eye two are shown in Figures 8 and 9, respectively. The white bars in the images on the lower left side of Figure 3.8 and Figure 3.9 identify the one-by-nine pixel regions along the vessel centers where spectra were measured. Images were rotated to align the vessel vertically prior to data analysis.

The solid lines in Figure 3.8 and Figure 3.9 correspond to the spectra obtained for the BSS filled retinal vessels from Eye 1 and Eye 2. Both spectra are essentially flat across the visible. The transmittance spectra shown in Figure 3.8 has a high frequency ripple from 550-600nm, a highly sampled wavelength region (Table 3.1). This is likely an artifact of the spectral response of the Basler 600f series camera, which exhibits a similar high frequency variation across the visible spectrum. We deemed that this ripple in the Basler's spectral response renders the camera unfit

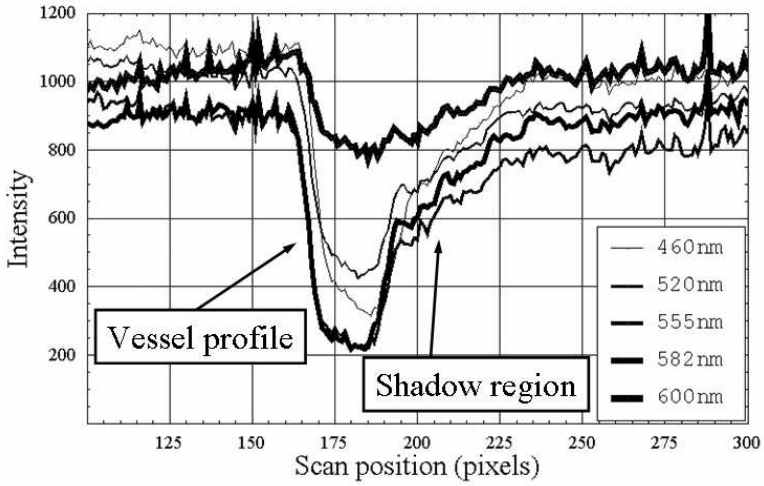

FIGURE 3.7. Retinal vessel intensity profiles for Eye 2 obtained with intravitreal illumination. The glint which is usually present in fundus photographs is absent; the minima of the profiles are easily identifiable.

for precision imaging spectroscopy. Upon discovering this ripple, we switched to a camera without such spectral oscillations, the Dalsa camera, for the second and all successive experiments. The data from the Basler camera is included in this paper because to date only two eyes have been successfully cannulated and perfused out of approximately eighty attempts. The closely dashed lines in Figure 3.8 and Figure 3.9 correspond to the spectra obtained for the deoxygenated blood filled retinal vessels from Eye 1 and Eye 2. The highest transmittance occurred in the 620-700 nm range. A minimum value was located at 555 nm for eye one and 520 nm for Eye 2. Both transmittance curves increase sharply from 570-620nm. The remaining curves Figure 3.8 and Figure 3.9 correspond to the spectra obtained for the oxygenated blood filled retinal vessels from Eye 1 and Eye 2 (more widely spaced dashes). The vessel transmittance spectra for oxygenated blood filled vessels in Figure 3.8 and Figure 3.9 contain a bimodal minimum in the 550-600nm range, characteristic of oxygenated blood. Maximum transmittance for both curves occurred in the 620-700nm range

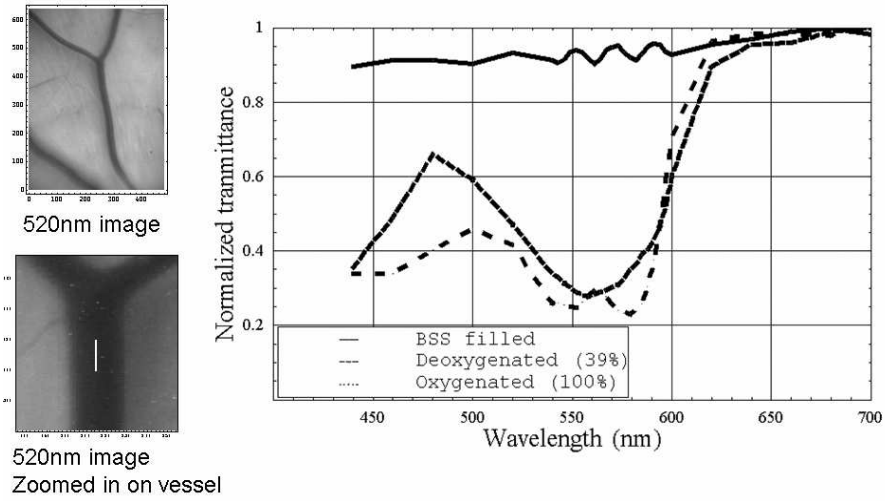

FIGURE 3.8. Image of the region of interest for Eye 1. Spectra were acquired at the center of the vessel marked in white. Spectral transmittances of a retinal artery filled with BSS (solid line), deoxygenated blood (39% saturated) (closely dashed line), and oxygenated blood (100%) (widely dashed line). Illumination is from the right. Ripples in the 540 to 600 nm region BSS spectrum are due to the spectral sensitivity variations of the Basler 600f camera.

as expected for oxyhemoglobin. Both transmittance curves increase sharply from 580-620nm.

3.2.2 Fundus reflectance measurements

Fundus reflectance measurements were performed for each of the three perfusion conditions for both eyes. Intensities were averaged in vessel free regions of the two eyes for the 5 by 5 array of pixels indicated in black in the lower left hand images to construct the fundus reflectance. The solid curves shown in Figure 3.10 and Figure 3.11 correspond to the data obtained for BSS filled blood vessels. Fundus reflectance measured for vessels perfused with deoxygenated blood are given by the closely dashed curves in Figure 3.10 and Figure 3.11. The remaining two curves (widely dashed lines) in Figure 3.10 and Figure 3.11 correspond to reflectance measured when the

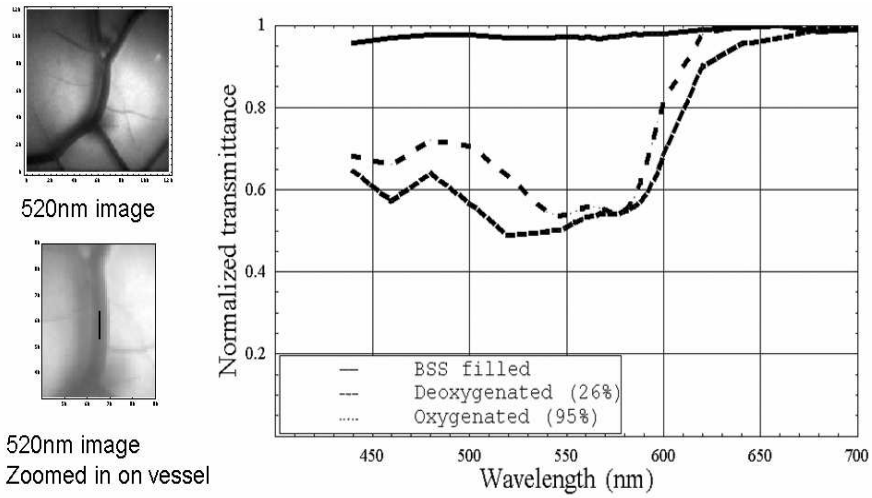

FIGURE 3.9. Eye 2 results. Relative spectral transmittances of a filled retinal vein filled with BSS (solid line), deoxygenated blood (26% saturated) (closely dashed lines), and oxygenated blood (95%) (widely dashed lines). Illumination is from the right and a small gap is visible between the vessel and its shadow to the left. Spectral images were taken on the second enucleated eye with the Dalsa Ca-D1 digital monochrome camera.

vessels were perfused with oxygenated blood

The behavior of the fundus reflectance appeared to be nearly independent of the perfusion conditions. The fundus reflectance curves for eye one (Figure 3.10) have maximum value at 660 nm. A high frequency ripple is evident in all the fundus reflectance curves for Eye 1 in the 550-600 nm range. A minimum reflectance appears to be located somewhere in the 560-600 nm wavelength range, the spectral region containing the high frequency ripple. The reflectance monotonically increased from 600-700 nm for all curves obtained for Eye 1. The fundus reflectance for BSS filled retinal vessels is approximately 15% higher in the 440-600nm range. For fundus reflectance curves calculated from spectral images sets obtained from Eye 2 (Figure 3.11 and Figure 3.11), the maximum reflectance values were located at 480 nm. Maximum reflectance occurred at 480 nm for the three perfusion conditions. Minimum

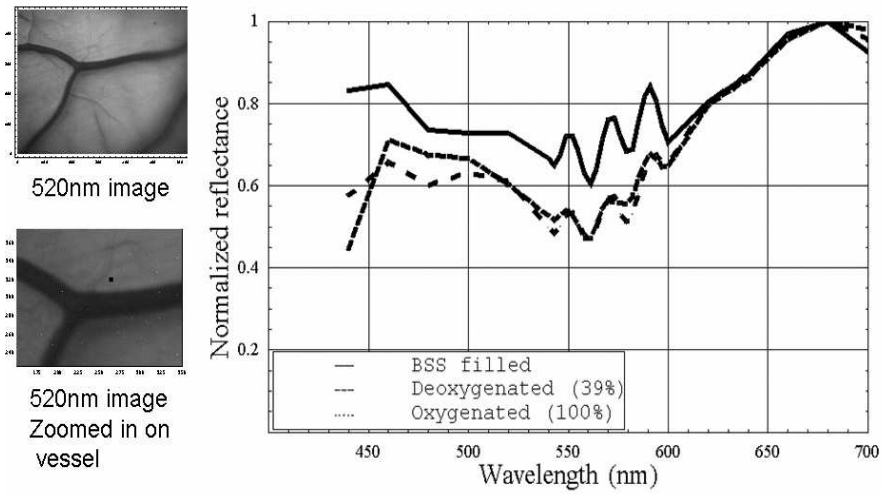

FIGURE 3.10. Eye 1 results. Fundus reflectance spectra for a vessel free area acquired while the adjacent retinal vessels were filled with BSS (solid line), deoxygenated blood (39%) (closely dashed line), and oxygenated blood (100%) (widely dashed line). Reflectances were calculated from spectral image sets taken on the first enucleated eye with the Basler 600f series digital monochrome camera.

reflectance occurred at 585 nm in all cases for Eye 2. The reflectance monotonically increased from 585-700 nm for all curves obtained for Eye 2.

3.3 Discussion

Comparison of our vessel OD measurements with the absorption spectra of oxyhemoglobin and deoxyhemoglobin is shown in Figure 3.12 and Figure 3.13. In Figure 3.12 , the spectra obtained for vessels perfused with deoxygenated blood are compared to the absorption spectrum of hemoglobin (deoxyhemoglobin) obtained by van Assendelft.1

The spectrum from the vessels of eye one is nearly identical to van Assendelft's deoxyhemoglobin absorption curve in the 540-640nm wavelength range. A local maximum absorption occurs at 555nm for both curves. A local minimum absorption

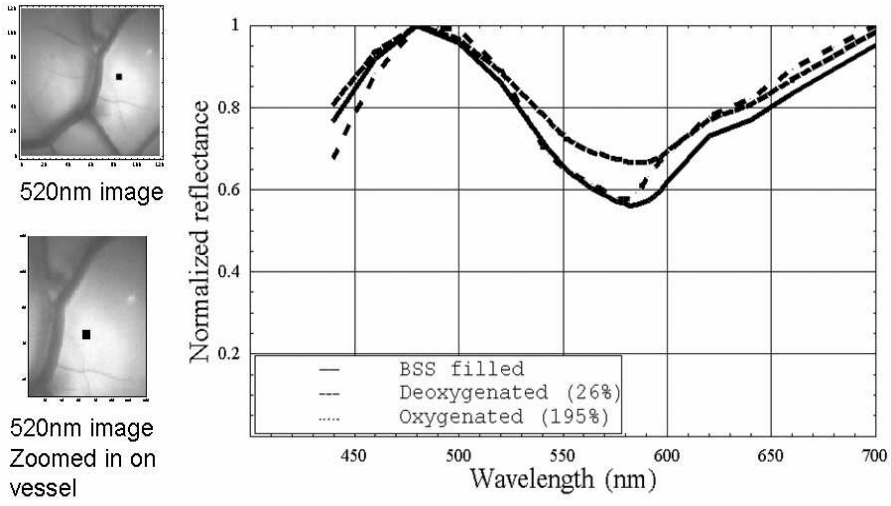

FIGURE 3.11. Eye 2 results. Fundus reflectance measurements for a vessel free area acquired while the adjacent retinal vessels were filled with BSS (solid line), deoxygenated blood (26%) (closely dashed line), and oxygenated blood (95%) (widely dashed line). Reflectances were calculated from spectral image sets taken on the second enucleated eye with the Dalsa Ca-D1 digital monochrome camera.

occurs at 475nm for both curves. The spectrum from the vessels of eye two shares some characteristics with van Assendelft's deoxyhemoglobin absorption data. The spectrum from eye two has a maximum absorption value at 520nm, shifted from the deoxyhemoglobin absorption by 35nm towards the blue. Both curves deviate from the absorption curve for deoxyhemoglobin below 460nm and above 620 nm. In Figure 3.13, the spectra we measured for retinal vessels perfused with oxygenated blood are compared to the absorption spectrum obtained by van Assendelft for oxyhemoglobin. The spectrum from Eye 1 and Eye 2 are very similar to van Assendelft's data for oxyhemoglobin in the 500-580nm wavelength range. A bimodal absorption maximum is seen for data from both eyes in the 550-600nm wavelength range. Both curves deviate from the absorption curve for oxyhemoglobin below 500nm and above 590 nm.

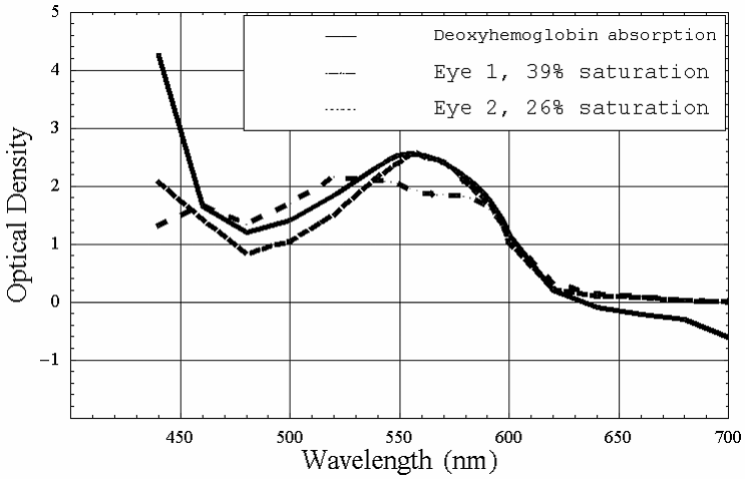

FIGURE 3.12. Optical density of retinal vessels perfused with deoxygenated blood for eye one (dashed) and eye two (dash space) shown superposed with van Assendelft's the absorption spectrum for hemolyzed deoxygenated hemoglobin (solid line).1

3.4 Summary and Conclusions

Spectral analysis of enucleated swine retinal vessels and fundus spectral reflectance is obtained via the use of intraocular illumination and retinal imaging. Perfusion of the retinal vessels with BSS, deoxygenated blood and oxygenated blood is accomplished by cannulation of the central retina artery. The success rate for successful postmortem perfusion is less than 3%. The spectra obtained from these measurements indicate the strong influence of oxyhemoglobin and deoxyhemoglobin absorption. The measured spectra in vessel free areas were shown to be affected by the presence of fundus pigmentation, primarily deoxyhemoglobin. The current results are preliminary since only two eyes have been perfused and studied. These measurements are ongoing and a larger study will be published after a statistically significant number of retinas have been spectroscopically analyzed. A new technique of intravitreal illuminated retinal spectroscopy shows promise for mapping the chromophores of the retina. Intravitreal illumination nearly eliminates the problem of extraneous reflections (glints) from

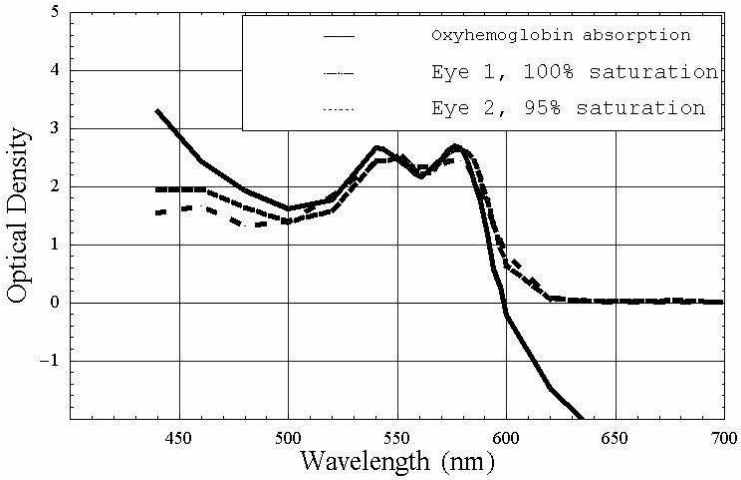

FIGURE 3.13. Optical density of retinal vessels perfused with oxygenated blood for eye one (dashed) and eye two (dash space) shown superposed with van Assendelft's absorption spectrum for hemolyzed oxygenated hemoglobin (solid line).1

retinal blood vessels. Compared with conventional fundus images, vessel intensity profiles exhibit clearly defined minima at the vessel center. Thus retinal spectroscopy with intraocular illumination may be of great value despite being highly invasive.

Chapter 4

Multispectral Diffuse Reflectance Measurements of the Porcine Fundus

Intravitreal illumination was used for the purpose of measurement of fundus reflectance in enucleated swine eyes. The use of intravitreal illumination allows for variation of illumination angle, eliminates the corneal and retinal vessel glints, and reduces the errors in quantitative spectro-radiometry arising from multiple passes through the anterior ocular structures; our technique results in light reflected from the fundus undergoing a single pass through the anterior chamber. The illumination direction is varied and measurements of fundus reflectance are made from a fixed viewing angle. Reflectance measurements for various illumination angles are compared to each other and to the predictions of the Lambertian model. This work as been published in Investigative Ophthalmology and Visual Science. [49]

4.1 Methods

Multispectral fundus spectroscopy is performed on two American Yorkshire porcine eyes for multiple angles of illumination. The same experimental protocol is used for both eyes, although the illumination angles are different for each eye.

4.1.1 Eye Preparation

Two enucleated American Yorkshire swine eyes are obtained from the University of Arizona Meat Sciences Laboratory. The eye preparation is identical for both specimens. Experiments are performed 6-12 hours after the death of the animals. A 4mm infusion cannulum is placed through the pars plana and sutured in place. The infusion cannulum is attached to a balanced salt solution (BSS) gravity feed system to

maintain intraocular pressure at levels comparable to in vivo conditions. A contact vitrectomy lens (Bausch and Lomb: F36202.08, Rochester) is placed onto the cornea using an index matching (index of refraction: nd=1.337) viscoelastic coupling agent (Goniosol, Bausch and Lomb, Rochester). The plane formed by the anterior surface of the contact lens is made parallel to the iris plane by suturing the contact lens ring concentrically with the iris. Different illumination angles are accomplished by accessing multiple sclerotomies created along an arc line. Figure 4.1 shows the mounted eye.

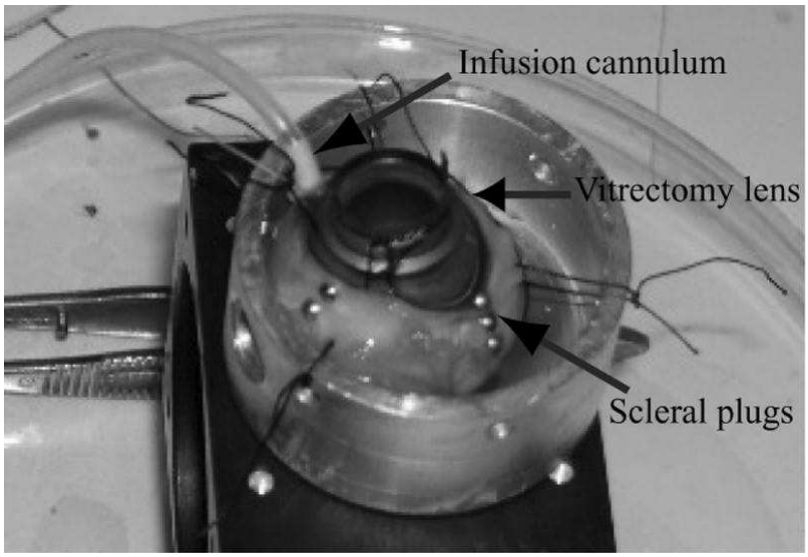

FIGURE 4.1. An enucleated swine eye is sutured to a custom eye mount. The infusion cannulum is inserted into the eye through the pars plana and the sutured contact lens is placed on the cornea. Posterior to the limbus are two columns of scleral plugs marking the location of the sclerotomies.

4.1.2 Imaging system

Light from a scanning monochromator (Oriel Spectral Luminator, Irvine) is coupled into a fiber optic intraocular illuminator (Alcon Laboratories, Fort Worth) which is

inserted into the vitreous to illuminate the retina. The monochromator is operated at a spectral resolution of 10 nm, with an approximately Gaussian power distribution within the spectral band. The output power is approximately 150 microwatts per wavelength band. The measurement area of the fundus is imaged with a 3.3X macro zoom lens (Edmund Scientific 56-524, Edmund Scientific, Barrington) onto the CCD camera, a Dalsa Ca-D1 12 bit high speed digital monochrome camera (Dalsa Corporation, Waterloo, Ontario, Canada). Figure 4.2 illustrates the illumination system.

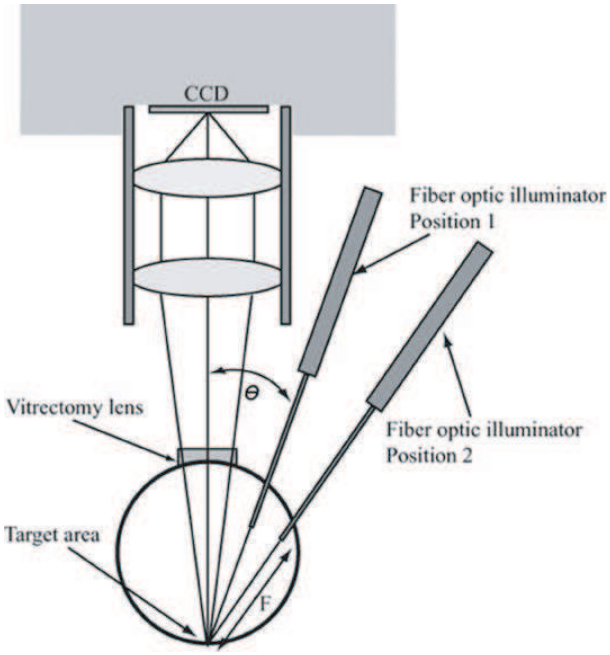

FIGURE 4.2. Diagram of imaging system and illumination configuration. An example of two illumination angles is provided. The fiber optic illuminator is kept a constant distance from the target area.

4.1.3 Data collection

The fiber optic intraocular illuminator is placed in the first sclerotomy, the closest to the pupil. This sclerotomy provides the smallest angle of illumination, θ, between

TABLE 4.1. Illumination wavelengths for multispectral image sets.

Wavelength Range	**Spectral Stepsize**
440nm-460nm	10nm
460nm-540nm	20nm
543nm-600nm	3nm
605nm-615nm	5nm
620nm-700nm	10nm

the fiber optic intraocular illuminator and the "optic axis" for the target area. The illuminated fundus is focused onto the camera. A suitable vessel free target area is identified using the retinal vessels as landmarks. The depth of the fiber optic intraocular illuminator is adjusted to maximize the dynamic range of the camera (i.e. the brightest pixel in the image is nearly saturated). An image is acquired at each of the 36 wavelengths listed in Table 4.1. The wavelengths are referenced with respect to the peak of the in-band spectral power distribution. The reflected light is collected over a solid angle of 0.028 steradians, the solid angle subtended by the eye's pupil, which is the aperture stop of this system.

To determine the angle of the fiber optic illuminator, an image of the experimental apparatus is taken with a digital camera (Nikon Cool Pix 4300, Nikon Corporation, Tokyo) aligned orthogonally to the plane defined by the sclerotomies. Orthogonality is insured by using an optical table equipped with a rail carrier system. The digital image is analyzed to determine the angle of the fiber optic illuminator in the eye. We estimate the systematic error in angular measurement at $\pm 2^{\circ}$. This systematic error is indicative of the error in the absolute value of the measured angles, but the relative differences between measured angles are affected only slightly.

The fiber optic illuminator is successively inserted into each sclerotomy and illuminates the target area of the fundus at increasing angles. The multispectral image acquisition process is repeated for each sclerotomy. The appropriate depths of the

TABLE 4.2. Illumination angles used to illuminate the fundus for the enucleated eye samples.

Sample	**Illumination Angles**			
Eye 1	26°	33°	37°	48°
Eye 2	33°	37°	48°	

fiber optic illuminator for the remaining sclerotomies are determined based on illumination geometry such that the end of the illuminator is kept at a constant distance from the fundus. The depth of the fiber optic illuminator is verified by measuring the length of the fiber optic illuminator exterior to the sclera. The only variable between spectral image sets is the angle of illumination in the plane of the sclerotomies. For all sclerotomies, the brightest portion of the illuminating light beam is placed on the target area of the fundus using retinal blood vessels as landmarks. Four angles of illumination are used for the first enucleated swine eye and three for the second eye. Table 4.2 lists the angles of illumination used for the two eyes. A calibration image set is acquired upon completion of data collection. A Spectralon lined integrating sphere is illuminated by the fiber optic intraocular illuminator and the exit pupil of the sphere is imaged by the camera system. This calibration set is used to correct for the spectral intensity variation in the illuminating source and the spectral response of the CCD.

4.1.4 Data analysis

Mathematica is used to perform image calibration, subtraction, averaging, and plotting. Reflected spectra are constructed for each angle of illumination for each eye. The reflectance spectra are averaged over 25 pixels in the target area and are normalized to the value obtained in the brightest image for each eye. The brightest image corresponds to the smallest illumination angle for each eye.

4.2 Experimental Results

Rows one and two of Figure 4.3 show the 520 nm images taken at different illumination angles for the first and second eye, respectively. Row 1 of Figure 4.3 contains 520 nm images that were obtained for illumination angles of 26°, 33°, 37°, and 48°. Row 2 of Figure 4.3 contains 520 nm images taken for illumination angles of 34°, 37°, and 48°. Note the absence of glints along the retinal vessels. The black squares indicate the five-by-five pixel area over which pixel intensity values were averaged for the determination of the reflectance spectra.

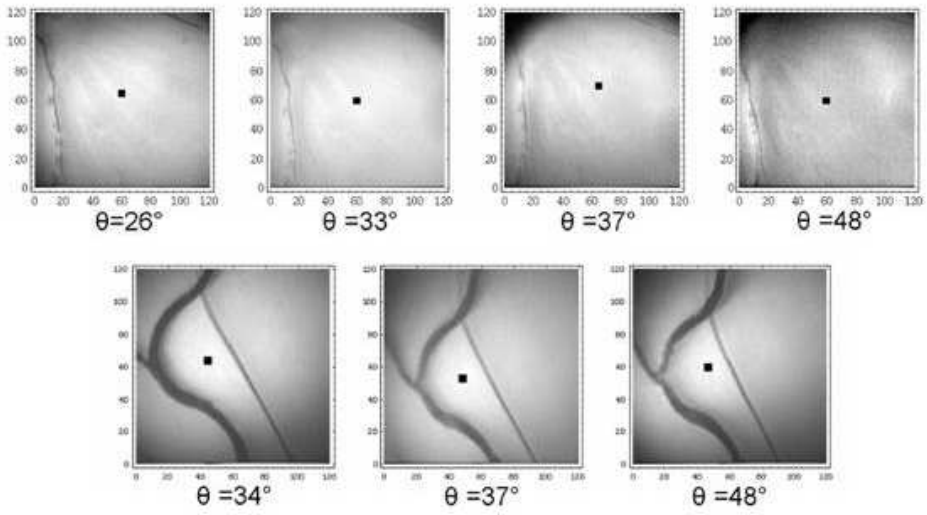

FIGURE 4.3. Row 1: 520 nm images for Eye 1 taken at a set of illumination angles. The values within the black square were averaged for the spectral reflectance calculation. Row 2: 520 nm images for Eye 2 taken at a set of illumination angles.

Figure 4.4 and Figure 4.5 show the normalized fundus reflectance spectra as a function of illumination angle for the two eyes. The curves in Figure 4.4 were normalized to the largest intensity value in Eye 1 taken at 26°. The curves in Figure 4.5 (Eye 2) were similarly normalized. The reflectance monotonically decreases with increasing illumination angle.

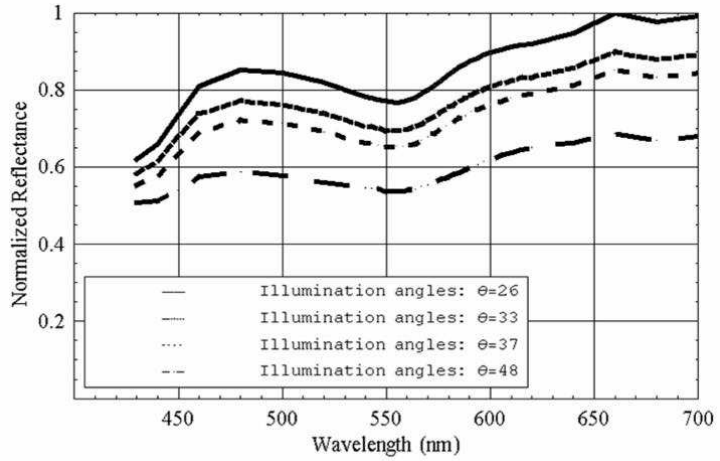

FIGURE 4.4. Normalized reflectance vs. wavelength for Eye 1 for illumination angles 26° (solid line), 33° (closely dashed line), 37° (dashed line), and 48° (widely spaced dashed line). There is a large change from 430 to 480 nm (from 20% to 30% decrease, respectively) over the 22° illumination angle variation. From 480 nm to 700 nm, the change in reflectance decreased by an average of 31.20% ± 0.3%.

Figure 4.6 and Figure 4.7 show the normalized reflectance as a function of illumination angle and wavelength, with a subset of wavelengths shown. Each vertical collection of symbols represents the spectra for a particular illumination angle. The decrease in reflectance with increasing illumination angle is apparent.

Several trends are evident in Figures 4 through 7. Fundus reflectance decreases with increasing illumination angle. Fundus reflectance is lowest in the blue (430 nm) and increases sharply between 430 and 480nm. A local minimum occurs at approximately 555 nm. Reflectance generally increases at wavelengths longer than 555 nm with a reflectance maximum at 660 nm. The smallest variation of reflected intensity with illumination angle occurs in the blue. For wavelengths longer than 450 nm the variation of reflectance with illumination angle increases.

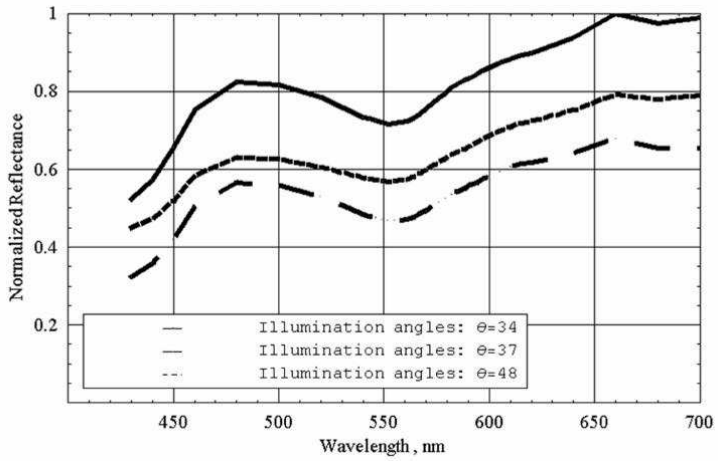

FIGURE 4.5. Normalized reflectance vs. wavelength for Eye 2 for illumination angles 34° (solid line), 37° (closely dashed line), and 48° (widely spaced dashed line). There was again a large change from 430 nm to 480 nm (from 39% decrease at 430 nm to 30% decrease at 480 nm) over the 14° degree illumination angle range for Eye 2. From 480 nm to 700 nm the reflectance decreased by a average of 31.20% ± 1.8%.

4.3 Discussion

The results indicate that the spectral reflectance of the swine fundus deviates from the Lambertian model that is customarily used to model fundus reflectance. A Lambertian reflector has three defining reflectance properties: (1) the angular distribution of reflected flux is independent of illumination angle; (2) for a given illumination angle, reflected intensity is independent of viewing angle; and (3) the total reflected intensity decreases according to Lambert's law (also called the "Cosine law"),

$$I_{diffuse} = I_0 * \cos(\theta), \tag{4.1}$$

where $I_{diffuse}$ is the total reflected intensity, I_0 is the incident intensity, and θ is the angle between the surface normal and the incident light as illustrated in Figure 4.8.

This experiment tests only the third Lambertian property. The reflectance decrease predicted by Lambert's law is compared with the measured reflectance de-

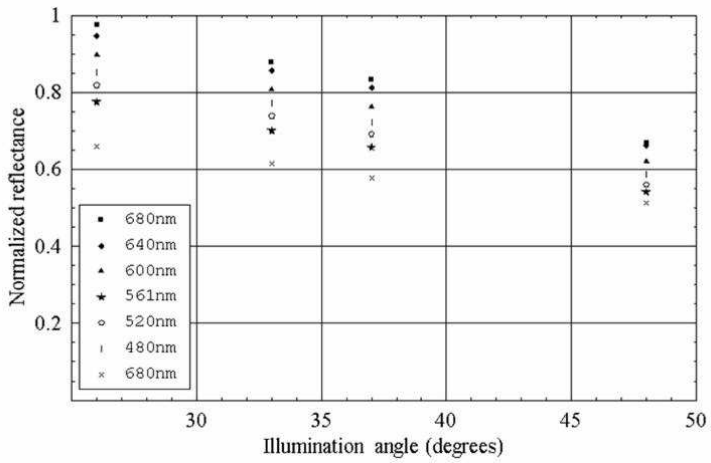

FIGURE 4.6. Normalized reflected intensity vs. illumination angle, Eye 1.

crease. The measured reflectance from the smallest illumination angle (26°) was used to generate the three Lambertian reflectance curves for the remaining illumination angles. The third property of the Lambertian model specifically states that the total reflected intensity varies with the cosine of the respective illumination angles, so the measurements in Eye 1 should vary as the ratio cos(26°) : cos(33°) : cos(37°) : cos(48°), where the symbol ":" indicates ratio. The percent difference between this prediction and the measurement is plotted in the top graph in Figure 4.9. For a Lambertian reflector these percent errors would be zero. The bottom graph in Figure 4.9 is the corresponding plot for Eye 2.

The results of this research indicate the fundus is not a perfectly diffuse reflector because the measured intensity at larger illumination angles is less than that predicted by Lambert's law. In addition, the variation from Lambertian is spectrally dependent. The characteristic spectra of fundus pigments and retinal blood may have a significant dependence on illumination angle. These preliminary findings imply that an accurate model of fundus reflectance requires consideration of illumination angle. Further studies are necessary to determine the analytical form for this term.

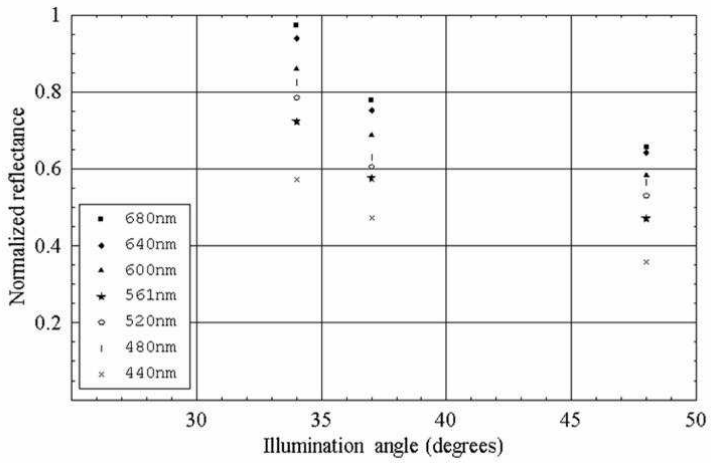

FIGURE 4.7. Normalized reflected intensity vs. illumination angle, Eye 2.

4.4 Conclusions

Fundus spectral reflectance data obtained using intraocular illumination is presented. Intravitreal illumination allows for variation in illumination angle and avoids problems with extraneous reflections, i.e. glints, from the anterior region of the eye and from the retinal vasculature. The invasive nature of this method excludes it from use in clinical settings. The usefulness of this technique as a research tool in enucleated eyes and animal models, however, is clear because of the new capabilities it provides for quantifying fundus reflectance.

The presented results are from two enucleated swine eyes, and only one location on each fundus was measured. Spectral data indicate that fundus reflectance deviates from that of a perfectly Lambertian scatterer: this difference was measured at 5% in one sample and 20% in the second sample. Some variation in fundus reflectance is expected due to the directional reflectance of the retinal never fiber layer (RNFL). For future work, we intend to employ our technique of intravitreal illumination to study the directional reflectance behavior of the RNLF. A further source of error is found

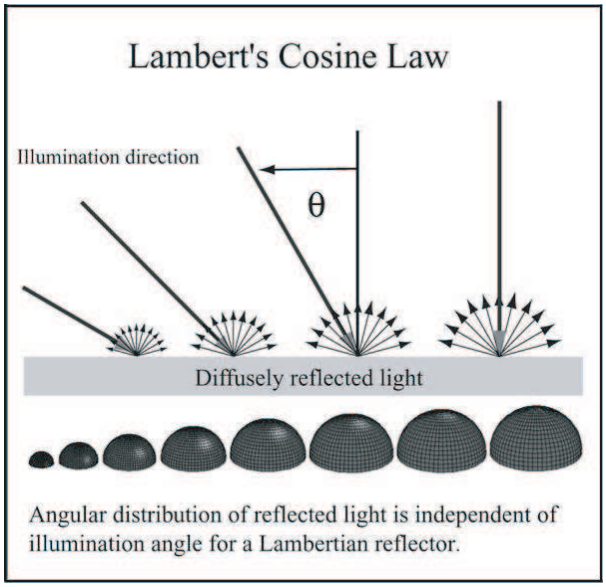

FIGURE 4.8. In the model of perfectly diffuse reflectors called Lambertian surfaces, the diffusely reflected light flux decreases as the cosine of the illumination angle, indicated by decreasing arrow length from left to right. The diffusely reflected light flux is independent of the viewing angle.

in the systematic error we encounter in the measurement of the angle of illumination. This error lowers the accuracy of the absolute value of the measured illumination angle, but affects the relative differences between each measured angle only slightly. Improvement on the technique for measuring the angle of illumination would improve the accuracy of these measurements. Differences from animal to animal, and differences from swine to human are to be expected. These in vitro results likely vary from in vivo measurements. Similar studies with live animal experiments are planned to address these issues.

Swine eyes were selected for their anatomic similarities to the human eye. Reflectance of the human fundus varies significantly from the fovea to the periphery. Thus reflectance measurements performed on a human fundus require knowledge of the proximity of the measurement location to the fovea for proper interpretation.

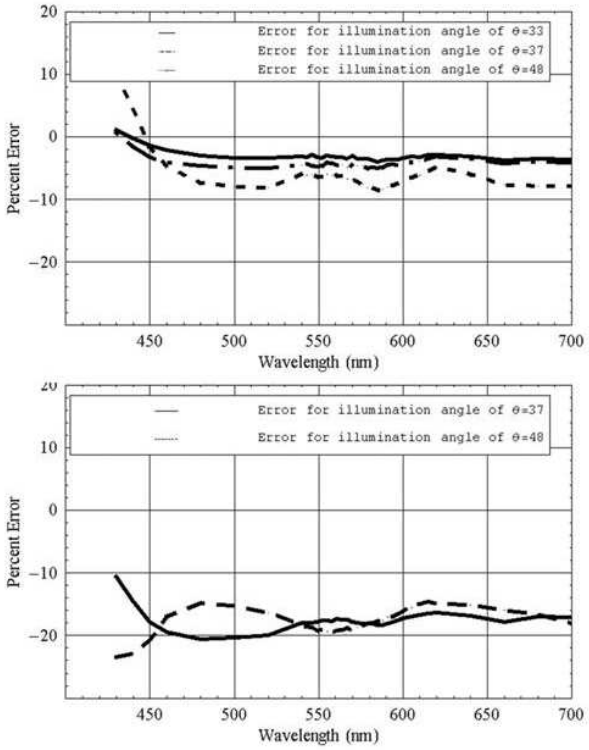

FIGURE 4.9. Top graph: The ratio of the measured decrease in fundus reflectance to the decrease predicted by Lambert's law for Eye 1. The diffuse reflectance of the fundus decreases faster than Lambert's law predicts as the angle of illumination increases. Bottom graph: Percent difference between the measured decrease in fundus reflectance and that predicted by Lambert's law for a perfectly diffuse reflector for Eye 2.

Swine have no fovea, so sensitivity to target position is reduced. To our knowledge no studies have been published which compare the reflectance properties of the human fundus to those of the peripheral swine fundus. The applicability of the results of these swine eye studies to human fovea studies is unknown.

Chapter 5
Retinal Oximetry on Live Swine

The techniques developed from work with enucleated swine eyes were used during a series of live swine experiments. Multispectral fundus images were obtained from the eyes of live swine as the animals' systemic blood oxygen saturation was systematically lowered by controlling the animals respiration. This chapter describes the experimental protocol used for the experiments, as well as presenting the data including the resultant blood oxygen saturation calculated for retinal veins and arteries. Results from this chapter are published in Current Eye Research. [50]

5.1 Methods

Intravitreal surgery was performed on two female American Yorkshire domestic swine, and a series of experiments were performed using intravitreal illumination to measure the retinal blood oxygen saturation. The experimental methods procedure detailed below was performed on both swine. The experimental protocol was approved by the University of Arizona Institutional Animal Care and Use Committee (IACUC).

5.1.1 Surgical Procedure/Animal Preparation

The swine was administered a general anesthesia mixture consisting of air, nitrogen, oxygen, and isofluorane. Swan-Ganz catheters were placed through the femoral vein and artery to monitor blood pressure and arterial oxygen saturation (S_aO_2) and mixed venous oxygen saturation (S_vO_2). The first catheter was placed in the aorta just distal to the heart and the second catheter was placed in the inferior vena cava just proximal to the heart. A peripheral oxygen saturation monitor was also placed in the rectum of the swine and a lid speculum was placed in the operative eye. A

4mm infusion cannulum was placed through the pars plana and sutured in place. The infusion cannulum was attached to a balanced salt solution (BSS) gravity feed system to maintain intraocular pressure. A contact vitrectomy lens (Bausch and Lomb: F36202.08, Rochester) was placed onto the cornea using an index matching (refractive index: nd=1.337) viscoelastic coupling agent. A fiber optic intraocular illuminator (Alcon Laboratories, Fort Worth) and the vitreous cutter were placed in the eye and a complete vitrectomy was performed.

5.1.2 Optical System and Data Collection

Following the surgical preparation of the animal, light from a scanning monochromator (Oriel Spectral Luminator, Irvine) was coupled into a fiber optic intravitreal illuminator which was inserted through the pars plana into the vitreous to illuminate the retina. The spectral resolution of the monochromator was approximately 10 nm. A 12 bit scientific grade CCD camera (Hamamatsu Orca-AG, Hamamatsu City, Japan) with a 3.3X macro zoom lens was used to image the retina. The peak wavelength of 10 nm wavelength band was stepped from 420 nm to 700 nm and an image of the target area was acquired at illumination wavelengths of 420, 430, 440, 460, 480, 490, 500, 510, 521, 532, 540, 545, 548, 552, 555, 558, 561, 565, 570, 575, 580, 590, 600, 615, 630, 645, 660, 680, and 700 nm. Each camera exposure was triggered using a cardiac monitor (Digicare Life Windows, Boynton Beach, Florida) to minimize vessel diameter variations by acquiring all images at the same point during the cardiac cycle; vessel diameter variations can range from 2% to 17% due to the cardiac cycle. [51, 52, 53] By minimizing the effect of vessel pulsation, the associated change in optical path length during the cardiac cycle should also be minimized. Some studies indicate that systemic blood oxygen saturation can vary with cardiac cycle; this effect too is avoided by capturing spectral images at the same point in the cardiac cycle. [54] Finally, the exposure time was adjusted to less than 40 ms (approximately

1/25 of the cardiac cycle) so the blood vessel size did not vary appreciably during the exposure.

The multispectral image sets were obtained over a 5 mm 5 mm region of the illuminated fundus containing a selected vein/artery pair. A dark image (obtained with the monochromator shutter closed) was subtracted from each image upon acquisition to correct for dark current and external light sources.

The measurement series began by setting the inspired respiration mixture to 100% oxygen, 0% medical grade air. Then the animal was allowed to stabilize for 8 minutes and a multispectral retinal image set was acquired. The SO_2, PO_2, PCO_2, pH, and hematocrit were measured from small blood samples collected from the two Swan-Ganz catheters using an ISTAT Personal Clinical Analyzer (Heska Corporation). The inspired air/oxygen mixture was then modified to decrease the swine's blood oxygen saturation in increments of approximately 10% as measured by the rectally-mounted pulse oximeter. The measurement cycle (8 minute stabilization, spectral data acquisition, and blood gas analysis) was repeated at approximately 10% decrements, until the pulse oximeter read approximately 50%. Figure 5.1 illustrates the configuration used to illuminate the retina and obtain images of the retinal vessels.

5.1.3 Data Calibration and Analysis

A calibration data set collected by measuring the output port of an integrating sphere illuminated with the fiber optic illuminator. Then the multispectral images were corrected for spectral variation in the light source and for spectral variation in the CCD by dividing by the calibration spectrum. The inner wall of the integrating sphere is coated with Spectralon, which has a very uniform spectral reflectivity and is commonly used as a calibration standard. The fundus multispectral image sets were registered to correct for any motion of the swine eye which occurred during the data collection. Images were aligned to within a fraction of a pixel using a

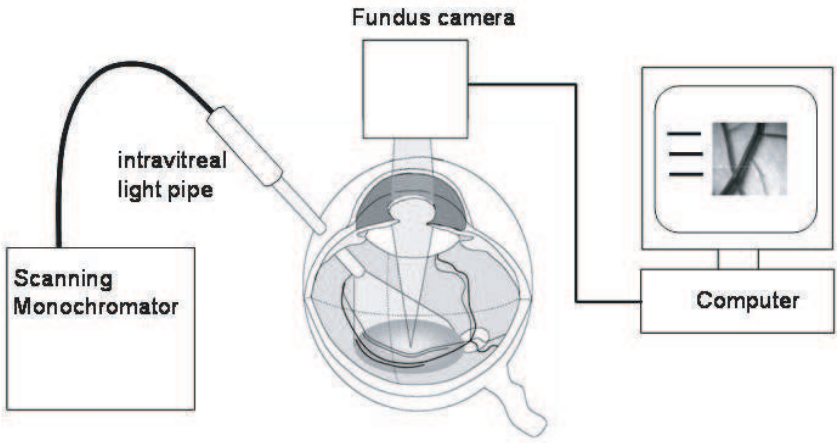

FIGURE 5.1. Illustration of intravitreal illumination method for retinal oximetry measurements.

bicubic spline interpolation in conjunction with a maximum mutual information merit function algorithm. [55]

Figure 5.2 shows the three primary light paths and the associated spectra, S_1, S_2, and S_3, that result from side illumination of a retinal vessel. The fourth light path, S_4, shown in Figure 5.2 represents light that is backscattered from red blood cells.

The relative contributions from S_2 and S_4 to the oximetry signal are unknown at this time, but the relative strengths of these two contributions are an important issue for further research. For the purpose of the current work, we combine these two possible sources as the oximetry signal, S_{ves}.

To summarize, the possible light paths are:

- S_1, light diffusely reflects from the fundus and into the imaging system.
- S_2, light diffusely reflects from the fundus behind a vessel and traverses the vessel in single pass.
- S_3, light traverses the vessel in single pass and diffusely reflects from the fundus

into the imaging system (i.e. the vessel shadow).

- S_4, light that is laterally scattered from the vessel and from red blood cells

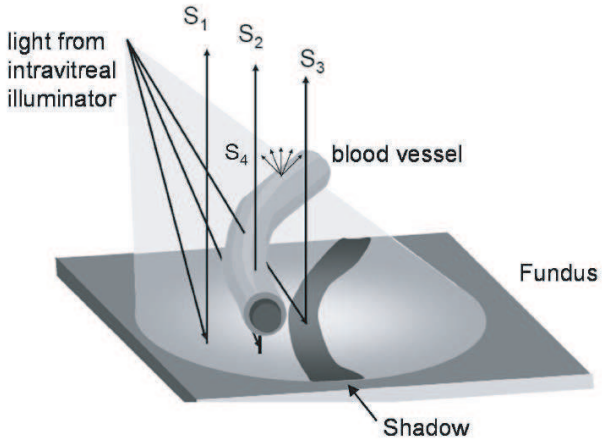

FIGURE 5.2. Several light paths and their associated spectra, S_1, S_2, S_3, and S_4, used in the intravitreal illuminated oximetry measurement.

The relative contributions from S_2 and S_4 to the oximetry signal are unknown at this time, but it is generally agreed that for larger blood vessels illuminated normally, the S_4 term dominates while smaller vessels allow more of the S_2 light to penetrate through the vessel, resulting in a combined S_2+S_4 signal. [33, 56, 57] The relative strengths of these two contributions as a function of illumination conditions are an important issue for further research. The two spectra, S_1 and S_2, differ in that the light in S_2 has taken a single pass through a vessel. Therefore the ratio S_2/S_1 is closely related to the vessel transmittance and provides a starting point for calculating SO_2. Spectra, S_1 and S_2, can be expressed as follows:

$$S_1(\lambda) = R_{fun}(\lambda) + L(\lambda), \tag{5.1}$$

$$S_2(\lambda) = S_{ves} * R_{fun}(\lambda) + L(\lambda). \tag{5.2}$$

Normalized vessel transmittance spectra for retinal artery and vein pairs were calculated using the measured S_1 and S_2 spectra. The measured spectral irradiance in the center of a vessel ($S_{vess]}$) was divided by the spectral irradiance measured from an area of bare fundus (S_1). For the vessel spectra, 11 pixels were averaged along a line that runs down the center of the vessel, and for the bare fundus, pixels are averaged over an area of 11 pixels near the vessel being tested.

5.1.4 Mathematical Model for Oxygen Calculation

S_{ves} is the transmission spectrum of the single pass light that passes through the column of blood in the vessel and R_{fun} is the base spectral reflectivity of the neighboring fundus. The additive *stray light* term, L, characterizes the amount of stray light that couples into the measurement due to scattering from within the eye. Assuming that the majority of scattering is from the fundus with the posterior chamber of the eye acting as an integrating sphere, the stray light has a spectrum close to the fundus reflectance and can be approximated as

$$L(\lambda) = A * R_{fun}(\lambda), \tag{5.3}$$

where A is a multiplicative straylight constant.

The vessel transmission function becomes

$$T(\lambda) = \frac{S_2(\lambda)}{S_1(\lambda)} = \frac{A}{1+A} + \frac{S_{ves}(\lambda)}{1+A} = A_1 + A_2 S_{ves}(\lambda). \tag{5.4}$$

Applying Beer's law in conjunction with the Van Assendelft data on hemoglobin absorption, the transmission function in Eq. (1.3) becomes

$$T(\lambda) = A_1 + A_2 B(\lambda) \exp \frac{1}{M}[-(SO_2)\{\hat{\varepsilon}_{HbO_2}(\lambda;t,c) - \hat{\varepsilon}_{Hb}(\lambda;t,c)\} + \hat{\varepsilon}_{Hb}(\lambda;t,c)] \tag{5.5}$$

where SO_2 is the oxygen saturation and $B(\lambda)$ is a multiplicative factor which encompasses the effects of blood cell scattering. [22, 23] $\hat{\varepsilon}_{HbO_2}$ and $\hat{\varepsilon}_{Hb}$ are the effective extinction coefficients for hemoglobin and oxyhemoglobin corrected for the 10 nm bandwidth of the scanning monochromator. [29, 30] The constant, M=log(e), converts from base 10 logarithms into base e logarithms. $\hat{\varepsilon}_{HbO_2}$ and $\hat{\varepsilon}_{Hb}$ are given by

$$\hat{\varepsilon}_{HbO_2}(\lambda) = -\log_{10}\left\{\int F(\lambda-\lambda_0)\exp\left[-\frac{c\,t}{M}\,\varepsilon_{HbO_2}(\lambda_0)\right]\,d\lambda_0\right\} \tag{5.6}$$

$$\hat{\varepsilon}_{Hb}(\lambda) = -\log_{10}\left\{\int F(\lambda-\lambda_0)\exp\left[-\frac{c\,t}{M}\,\varepsilon_{Hb}(\lambda_0)\right]\,d\lambda_0\right\} \tag{5.7}$$

where $F[\lambda\text{-}\lambda_0]$ is the line spread function of the monochromator, which is approximately Gaussian with a spectral bandpass, $\Delta\lambda$, of 10 nm,

$$F(\lambda-\lambda_0) = \frac{1}{2\pi\Delta\lambda^2}\,\exp\left[-\frac{(\lambda-\lambda_0)^2}{(\Delta\lambda)^2}\right] \tag{5.8}$$

Note that the effects of hemoglobin concentration c and vessel thickness t are encompassed in the effective extinction coefficients, $\hat{\varepsilon}_{HbO_2}$ and $\hat{\varepsilon}_{Hb}$. Oxygen saturation is calculated from this model by fitting the measured spectra to the theoretical transmission, given in Equation 5.5 using the Levenburg Marquardt non-linear fitting algorithm. [58, 59] A model for RBC scattering $B(\lambda)$ must also be specified. In this analysis, $B(\lambda)$ is assumed constant with wavelength.

A more realistic model could be obtained by expanding $B(\lambda)$ in a series of basis functions and fitting the expansion coefficients as additional variables in the non-linear algorithm. The choice of basis function to accurately model this RBC scattering is an area for future research. Spectral transmittance of the anterior chamber (cornea, lens and aqueous humor) also contributes to the measured spectra, although weakly. Measurements of the spectral transmittance of the cornea and lens that show an essentially flat transmittance over the region of our spectral fit for oximetry calculation (460-590nm). [60, 61] The cornea and lens spectral transmittance was omitted from

the described transmittance model, and it is unlikely that inclusion of this spectral transmittance would adversely affect oximetry calculations.

5.1.5 Calibration for Oxygen Saturation Calculation

Oxygen saturation values are calculated using the non-linear fit method described in the previous section applied to the 430 nm to 600 nm spectral region and calibrated to femoral arterial data. Absolute calibration of the $S_{ra}O_2$ measurement is based on the assumption that arterial oxygen saturation values are constant throughout the body and that the S_aO_2 in the aorta will be the same as the $S_{ra}O_2$. [34, 28] Figure 5.3 shows a line fitted to the calculated S_aO_2 values . The slope and y-intercept of fitted line were applied as a correction to all SO_2 measurements.

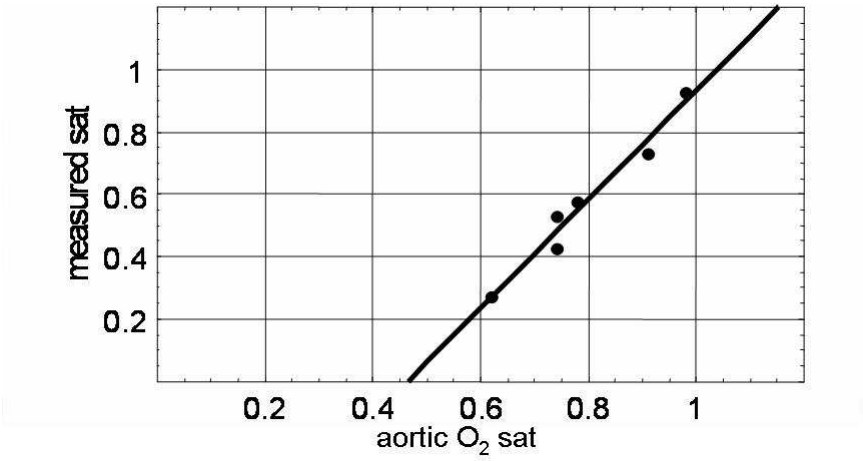

FIGURE 5.3. Arterial calibration for swine eye one.

5.2 Results

This section includes an analysis of the multi-spectral retinal images which are the starting point for the SO_2 measurement. Intensity cross sections through vessels and

TABLE 5.1. Decreasing arterial (top rows) and venous (bottom rows) oxygen saturation levels obtained for swine 1 as measured by the ISTAT PCA. Decreasing saturation levels were obtained by varying the inspired air mixture delivered to the swine.

Swine 1 ISTAT measurements		
S_aO_2 (%)	PO_2 (mm Hg)	pH
100	465	7.395
93	68	7.389
86	55	7.376
80	47	7.380
71	39	7.382
67	35	7.421
S_vO_2 (%)	PO_2 (mm Hg)	pH
89	60	7.360
74	43	7.349
78	46	7.334
62	35	7.360
48	28	7.358
45	27	7.361

the spectra of vessels and the adjacent fundus are analyzed, then the calculation of SO_2 from these spectra is presented.

Spectral images sets were obtained from one eye in each of two swine. Six decreasing saturation levels were obtained for swine one and five levels were obtained for swine two. Table 5.1 and Table 5.2 list the arterial and mixed venous oxygen saturation values taken at the time of each image series acquisition. PO_2 and pH levels are included in these tables; the pH did not vary appreciably for the decreasing saturation levels.

Figure 5.4 shows 430, 532, 600, and 660 nm monochromatic images of a retinal vein/artery pair from the first swine. The intravitreal light pipe was oriented such that the illuminating light is coming from the 7 o'clock orientation thus positioning the

TABLE 5.2. Decreasing arterial (top rows) and venous (bottom rows) oxygen saturation levels obtained for swine 2 as measured by the ISTAT PCA.

Swine 2 ISTAT measurements		
S_aO_2 (%)	PO_2 (mm Hg)	pH
98	98	7.443
91	58	7.442
78	41	7.441
74	38	7.447
62	25	7.619
S_vO_2 (%)	PO_2 (mm Hg)	pH
73	39	7.405
69	36	7.419
52	28	7.416
43	24	7.411
27	17	7.478

vessel shadows above the vessels. Note the absence of central vessel glints, the benefit of this oblique illumination. Narrower and dimmer vessel glints are occasionally visible from the vessel on the side towards the bottom of the image; see for example the center of the 600 nm image and the right side of the 430 nm image. Some areas of the retinal vasculature coincide with the illumination direction to produce specular reflection from the vessel apex that results in a glint artifact. Conditions that result in glint with intravitreal illumination include areas on the retinal vasculature where illumination direction satisfies the condition that the angle of incidence to the local surface normal on the vessel equals the "look" angle of the camera to the same location on the retinal vessel.

Figure 5.5 shows a series of intensity profiles, $I(x,\lambda)$, taken across a single vein at a subset of the illumination wavelengths: 460, 520, 555, 582, and 600 nm. The brighter levels at the left and right correspond to the neighboring fundus; the sharp

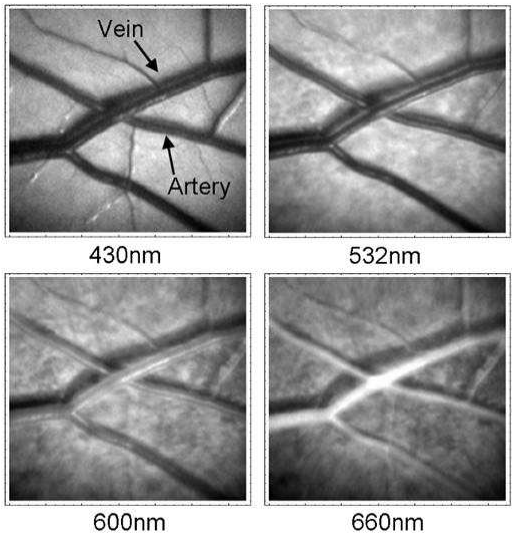

FIGURE 5.4. Spectral images of a vein/artery pair. The glint is substantially reduced. In the 600 and 660 nm red images, increased scatter from blood vessels is apparent.

dips result from the vessel and the vessel shadow.

The spectrum from $S_2(\lambda)$, is taken at the location of minimum transmission. The foreground spectrum, $S_1(\lambda)$, is from a fundus region parallel and next to the vessel under consideration. These intensity profiles have a single clearly defined minima associated with the retinal vessel. By contrast, intensity profiles generated using transcorneal illumination have two minimum on either side of the central glint.

The vessel transmission spectrum, $S_{ves}(\lambda)$, is taken at the location of minimum transmission. The foreground spectrum, $S_1(\lambda)$, is from a fundus region parallel and next to the vessel under consideration. The intensity scans in Figure 5.5a have a smooth vessel profile and clearly defined minima associated with the retinal vessel. In Figure 5.5b, glint degrades the vessel profile, resulting in a less accurate measurement of the minima. Intensity profiles generated using transcorneal illumination typically contain an even stronger glint, commonly having two minima on either side of the central glint. Figure 5.6 demonstrates the spectra generated from the two analysis

locations in Figure 5.5. Figure 5.6a and Figure 5.6b contain the vessel transmittance spectra associated with the glint-free and glint afflicted sites of Figure 5.5, respectively. The spectrum associated with the glint afflicted region (Figure 5.6b) is noticeably noisier than the transmittance measured at the glint free region.

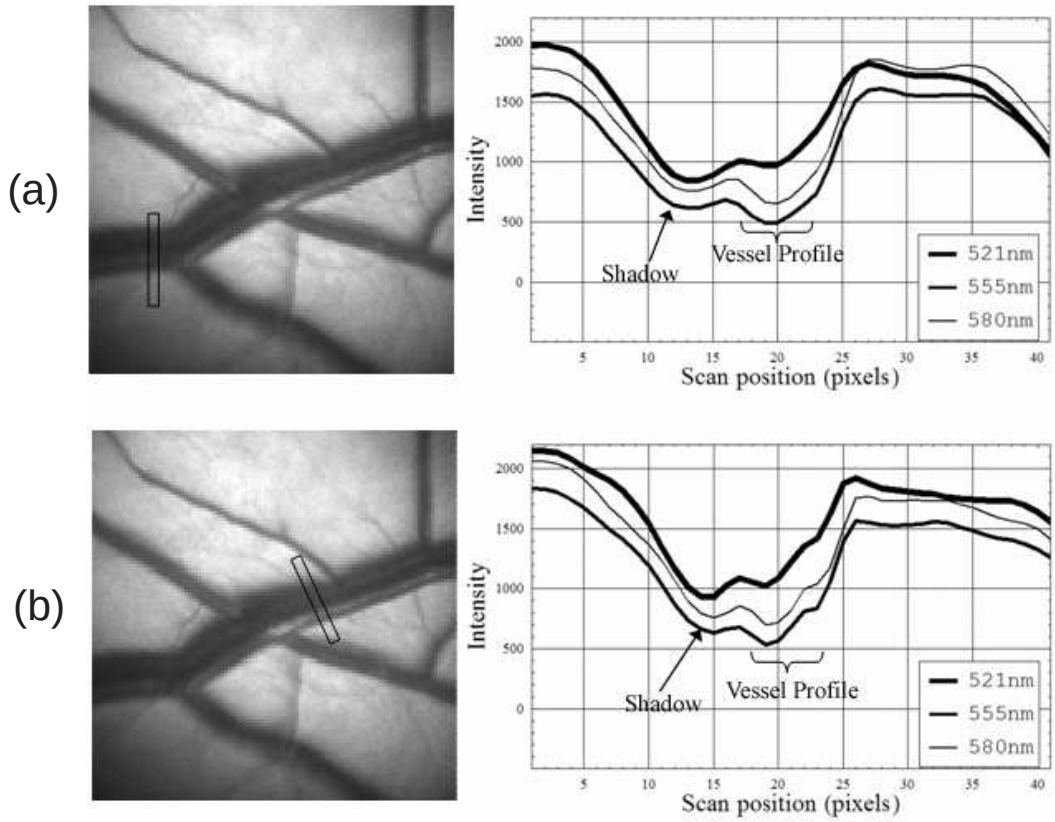

FIGURE 5.5. Intensity profiles obtained perpendicular to a vein at two locations: one where there is essentially no glint (top) and a second position (bottom) that exhibits the deleterious effects of glint. Intensity profiles for three illumination wavelengths are shown in each plot (521, 555, and 580nm). For the the top plot, the minimum of the transmittance measured at the center of the vessel profile is easily identifiable. The intensity profiles at of the bottom plot exhibit more noise, and the true minimum intensity is more difficult to ascertain.

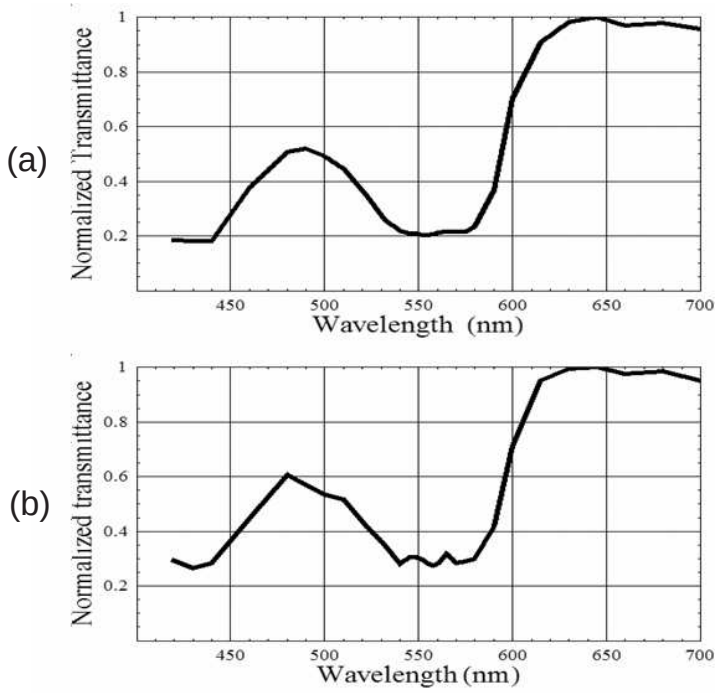

FIGURE 5.6. Normalized vessel transmittance used for oximetric calculations. The top plot depicts a spectrum constructed from the glint free area of the vein in Figure 5.5a. The noisier spectrum depicted in the bottom plot is constructed from the glint afflicted area on the vein shown in Figure 5.5b.

5.2.1 Spectral analysis of retinal vessels

Transmittance spectra were calculated at six artery sites and six vein sites along the vessels for both swine as shown in Figure 5.7. Normalized vessel transmittance spectra for the retinal artery and vein pair from one analysis site in eye one are shown in Figure 5.8a and Figure 5.8b for three inspired air mixtures. Each of the spectra shown in Figure 5.8 corresponds to a different inspired air mixture delivered to the swine and is labeled according to the aortic and mixed venous oxygen saturations measured from blood taken from the Swan-Ganz at the time of spectral image acquisition. Assuming that the arterial SO_2 is constant throughout the circulation, the aortic SO_2 values, listed in the legends of the two plots, should agree with the retinal arterial

saturation, $S_{ra}O_2$. Venous S_vO_2 varies significantly throughout the body depending on O2 consumption in the different organs, so the mixed venous S_vO_2 is unlikely to closely correlate with retinal $S_{rv}O_2$ but is provided for comparison.

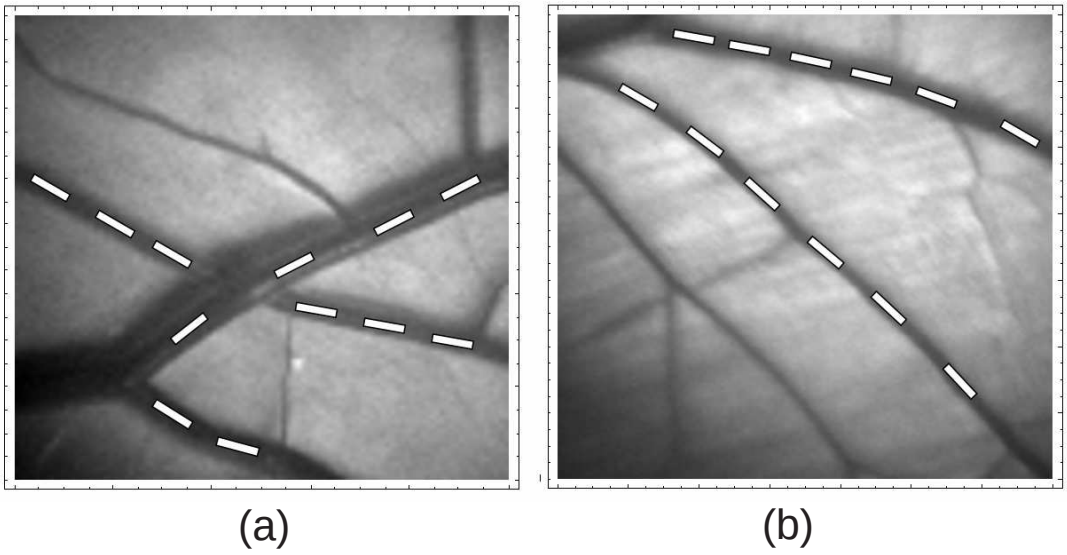

FIGURE 5.7. Analysis sites for the vessel pairs for swine 1 (a) and swine 2 (b). 11 pixels (shown as white bars overlaid on the retinal vessels) were averaged over each analysis location for both eyes.

Two significant changes are noticeable in the arterial spectra: First, the local maximum in the 460-520 nm range shifts from 510 nm to 480 nm as oxygen saturation decreases. Second, as saturation decreases, the two minima at 542 nm and 577 nm begin to converge to a single broad minimum at 555 nm, characteristic of the transition of the spectra of oxyhemoglobin to deoxyhemoglobin.

The retinal $S_{rv}O_2$ did not correlate closely with the mixed venous S_vO_2 co-oximeter measurements. Figure 5.8b, the spectra associated with the mixed venous S_vO_2 (thick solid line, ISTAT $S_vO_2 = 89\%$) shows the characteristic spectra associated with deoxyhemoglobin. The remaining two curves in Figure 5.8b (dashed line, ISTAT $S_vO_2 = 62\%$, and thin solid line, ISTAT $S_vO_2 = 45\%$) correlate more closely

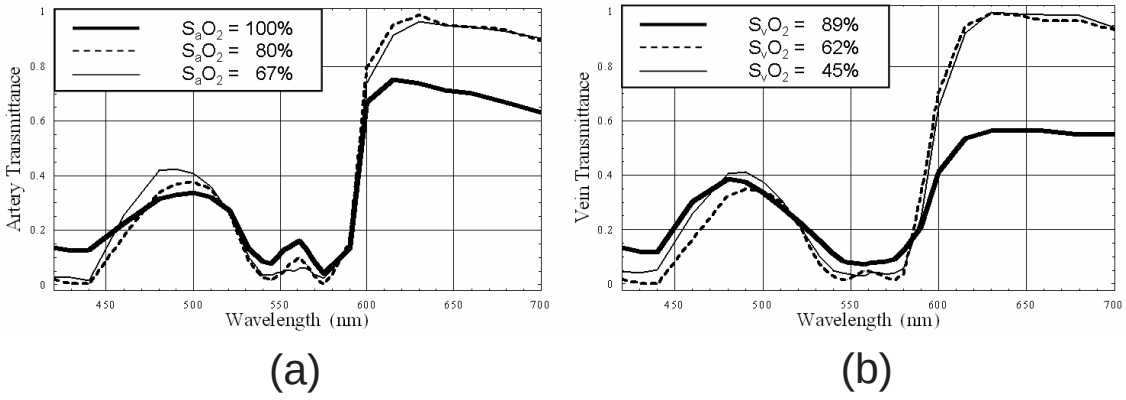

FIGURE 5.8. Vessel transmittance spectra for a retinal artery (a) and vein (b) in swine one are shown for three inspired air mixtures demonstrating sensitivity to oxygen saturation.

with the S_vO_2, although they appear to represent blood oxygen saturation that is of higher saturation than the S_vO_2 measured for the two experimental conditions. More discussion on these results is included in the next section.

5.2.2 Determination of Oxygen Saturation

Figure 5.9 shows the results of retinal arterial and venous oxygen saturation measurements for both swine eyes where SO_2 has been averaged over the 6 analysis sites from Figure 5.7. In the plots, the retinal arterial and venous oxygen saturation is compared to the aortic or mixed venous oxygen saturation as measured with the co-oximeter. Error bars indicate the standard deviation among the six analysis sites. Note the measured retinal arterial oxygen saturation levels are well correlated (r^2 = .86 and r^2 = .99 for swine 1 and swine 2, respectively) to the aortic saturation measurements. The measured retinal venous saturations in swine 1 were unusually low for the first three target S_aO_2 values. The final three measured retinal venous saturations for swine 1 were slightly higher than expected. This trend was repeated for swine 2; the first two measurements were lower than the femoral vein measurements, and the final

three were measurements are higher.

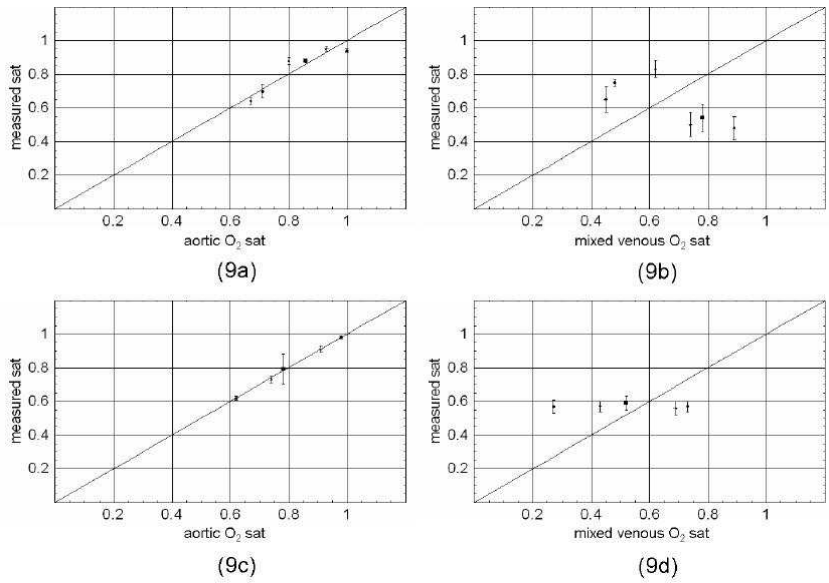

FIGURE 5.9. Calibrated oxygen saturation measurements for swine 1 and swine 2 are shown in rows 1 and 2, respectively. The left column (a, c) represents the comparison between aortic oxygen saturation levels (x-axis) measured with the ISTAT PCA and the measured oxygen saturation using the intravitreal retinal oximeter for each eye. The right column (b, d) represents the data for the retinal veins compared to the mixed venous oxygen saturation levels as measured with the ISTAT PCA. The line y=x is included for comparison.

5.3 Discussion

Oxygen saturation calculations on retinal arteries performed using intravitreal illumination were extremely well correlated with femoral artery data for both eyes. However, retinal venous oxygen saturation calculations yielded somewhat surprising results. All spectral images were obtained between 15 and 90 minutes post vitrectomy. The immediate effects of vitrectomy on retinal physiology are not well known. Replacement of the viscous vitreous gel by BSS has been shown to greatly increase the

amount of oxygen which diffuses from retinal veins into the vitreous cavity. [62, 63] Barbazetto et al. measured the vitreous PO_2 levels 2-3 times normal after steady state conditions were reached (approximately 30 minutes post vitrectomy). [62] This time scale is on the same order as that for which our measurements were performed, with retinal venous saturation measurements rising above femoral vein measurements after 60 minutes. It is possible that after a significant amount of time (30-60 minutes in this case), a steady state situation developed between the PO_2 in the BSS and the veins, effectively removing the pressure gradient that facilitated the diffusion of oxygen from veins into the less viscous BSS solution. Early in the experiment the BSS solution conceivably had a lower PO_2 compared to the veins, creating a diffusion gradient which caused oxygen to diffuse out of the veins. Immediately after vitrectomy, the oxygen saturation measured in the retinal veins was unexpectedly low. As the experiment (and time) progressed, it is possible that this diffusion gradient disappeared between the retinal veins and the BSS solution as steady state conditions were reached. This same trend was found in the $S_{rv}O_2$ measurements for swine 2, although to a lesser degree, as the saturations calculated for swine 2 remained relatively constant. The effects of this increased oxygen diffusion on autoregulation is unknown by the author. It likely contributes to the non-uniformity seen in the $S_{rv}O_2$ measurements but should have little effect on $S_{av}O_2$ measurements.

Complications resulting from vitrectomy are not uncommon, and are likely due to surgical trauma. [64, 65, 66] Retinal trauma resulting from vitrectomy likely causes unpredictable behavior in the autoregulation system of the eye, which could contribute to the unexpected retinal venous oxygen saturations measured.

5.4 Conclusions

Retinal oxygen saturation measurements have been demonstrated using intravitreal illumination for the first time. The removal of the central glint using off-axis illu-

mination in conjunction with the use of multiple wavelengths allows for a significant improvement in the accuracy of the vessel transmittance measurement. Intravitreal illumination results in a greater amount of retinal vasculature that is free of glint, thereby increasing the number of available vessel transmittance measurement sites. The off-axis illumination provides a single-pass light path through the retinal vessels simplifying interpretation of the multispectral images. The invasive nature of intravitreal illumination should exclude this oximetry technique from use in clinical settings. However, the usefulness of this technique as a research tool for use in animal models, and possibly during retinal surgeries, is clear. Retinal oximetry with intravitreal illumination could become a "gold standard" for retinal oxygen saturation measurements. This would aid in the development and calibration of noninvasive retinal oximetry techniques. The benefits of the separation of light paths can be seen when considering the fundamental model developed to describe light extinction due to hemoglobin and reduced hemoglobin. Oximetry calculations that are fit-based can use the separation of light paths to develop a model that is more true to life in the description of hemoglobin and reduced hemoglobin light interaction. Oximetric techniques employ the Lambert Beer's Law include such parameters as interaction path lengths or assumption of single vs. double pass light; these algorithms clearly benefit from the separation of light paths as double pass light encounters a path length of double the vessel diameter. The algorithms used to date to calculate oxygen saturation have been developed using vessel transmittance spectra that contained random data corruption, or "noise", caused by the existence of glint which obscures the true vessel minima. An algorithm developed with vessel transmittance data measured using intravitreal illumination would be largely free of glint "noise", enabling the development of more robust oximetry algorithms. The advantages revealed by oblique illumination should spur the development of transcorneal oblique illumination techniques: techniques in which the angle between illumination direction and measurement direction is maximized. The result could be a transcorneal illumination technique that retains some of

the benefits of intravitreal illumination. To the authors' knowledge, this is the very first paper on retinal oximetry with intravitreal illumination. The benefits provided by the method, namely simplifying light paths, reduction of glint and subsequently more accurate measurement of vessel transmittance, are presented in the manuscript. Retinal oximetry is not a mature field; no retinal oximeters have been built to data that are accurate enough for clinical viability. This illumination technique could be used to develop a variety of oximetric techniques by eliminating at least some sources of error (glint, uncertain light paths). It is likely that the applications for this illumination technique for fundus reflectometry and retinal oximetry will only become evident as the technique is matured through continued research.

Chapter 6

Oximetry on Live Swine Eyes: Oximetry with Subretinal Spectralon and the Effects of Vitrectomy on Oximetry of Retinal Vessels

In this chapter we present further results from two experiments; one performed on swine 1 from Chapter 5 and one experiment performed on a third swine. In the first experiment, a small piece of Spectralon was subretinally inserted beneath the sensory retina. The same retinal vessels are remeasured for a similar set of decreasing systemic oxygen saturation levels. The experiment on the third swine compared retinal vessel oximetric measurements performed both before and after vitrectomy to quantify the effect of vitreous removal on oximetry measurements.

6.1 Oximetry with Subretinal Spectralon

Retinal oximetry measurements are known to be affected by the presence of spectrally absorbing melanins in the retinal pigment epithelium (RPE) and choroidal blood. [32, 67, 41, 42] To isolate the spectral vessel transmittance from the effects of these two spectrally absorbing layers, a small Spectralon chip was inserted beneath the sensory retina. The same vessels examined in Chapter 5 (Swine 1) are again measured for decreasing systemic oxygen saturation and vessel oxygen saturation is calculated.

6.1.1 Experimental Methods

The experiment described in this section is a continuation of the experiment performed on Swine 1 of Chapter 5, therefore the description of the surgical preparation procedure, optical system, data collection and oxygen saturation calculation method

is not repeated here. The additional step performed here is the insertion of the subretinal Spectralon and another systematic lowering of the systemic oxygen saturation

Surgical Insertion of Subretinal Spectralon Following the data collection for the postvitrectomy oximetry described in Chapter 5, the swine was respirated with 100% oxygen and allowed to stabilize. After stabilizing the swine, a retinal detachment was induced near the site of the vessels imaged for the postvitrectomy measurements and a small disk of Spectralon (3mm by 0.5mm) was inserted between the sensory retina and the RPE. Figure 6.1 shows a drawing of the placement of the Spectralon chip.

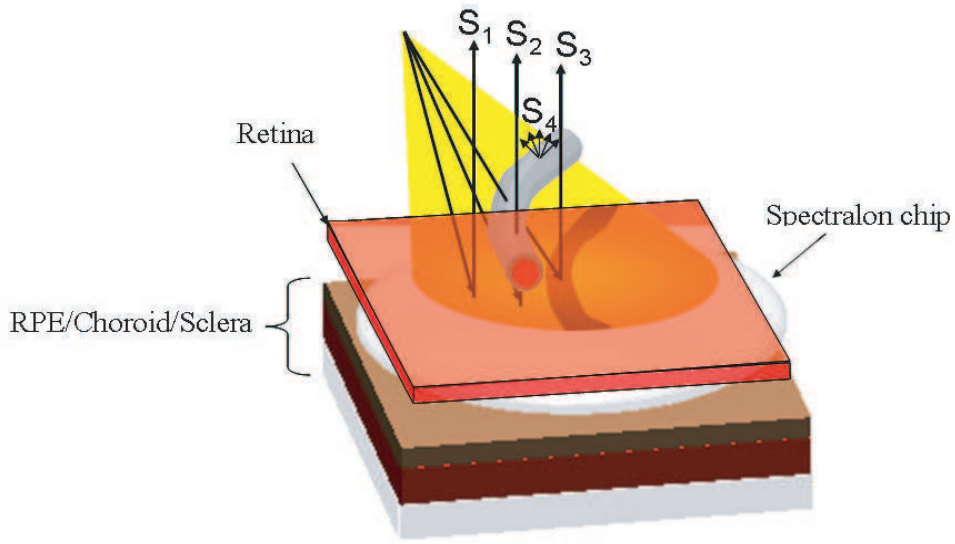

FIGURE 6.1. Illustration of the insertion of the Spectralon chip underneath the sensory retina. The associated light paths and their associated spectra, S_1, S_2, S_3, and S_4, used in the intravitreal illuminated oximetry measurement are shown.

Figure 6.2 shows the 440nm image obtained of the fundus after the Spectralon chip was inserted. Comparison of Figure 6.2 with Figure 5.5 shows that the same vasculature was imaged.

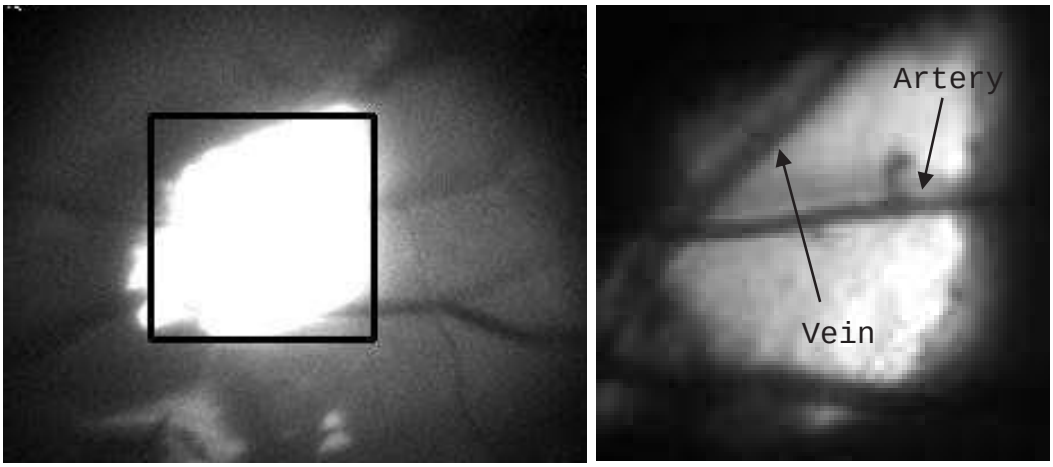

FIGURE 6.2. The 440nm image of the bright Spectralon chip inserted beneath the sensory retina(a). The smaller image shows a zoomed in view of the Spectralon chip (b), where the artery and vein analyzed are identified. This image contains the same vessels shown in Figure 5.5 for Swine 1.

6.1.2 Results: Oximetry with Subretinal Spectralon

This section includes an analysis of the multi-spectral retinal images which are the starting point for the SO_2 measurement. Intensity cross sections through vessels and the spectra of vessels and the adjacent fundus are analyzed, then the calculation of SO_2 from these spectra is presented. Spectral images sets were obtained from swine one after the subretinal Spectralon chip was inserted and multispectral image sets were obtained for six decreasing saturation levels. Table 6.1 lists the arterial and mixed venous oxygen saturation values taken at the time of each image series acquisition. PO_2 and pH levels are included in these tables; the pH did not vary appreciably for the decreasing saturation levels.

Four monochromatic images (430, 532, 600, and 660nm) of the analysis region with the subretinal Spectralon are shown in Figure 6.3. The light pipe is oriented such that illumination is directed from the bottom or 6 o'clock position in the images,

TABLE 6.1. Decreasing arterial (top rows) and venous (bottom rows) oxygen saturation levels obtained for swine 1 with subretinal Spectralon as measured by the ISTAT PCA. Decreasing saturation levels were obtained by varying the inspired air mixture delivered to the swine.

ISTAT measurements		
S_aO_2 (%)	PO_2 (mm Hg)	pH
100	463	7.416
86	52	7.412
76	42	7.390
67	36	7.387
58	31	7.384
42	26	7.378
S_vO_2 (%)	PO_2 (mm Hg)	pH
87	56	7.362
69	37	7.391
61	33	7.382
52	29	7.373
38	23	7.368
25	19	7.480

as can be seen by the shadow present for the artery in the 430 and 532nm images. The vessels become very faint in the 600nm image and are nearly invisible in the 660nm image. This in contrast to the similar monochomatic images presented in Figure 5.4, where the vessels in the 600nm and 660nm images are brighter than the background and clearly visible. The reduced contrast between the vessels and the background is due to the high reflectance of the Spectralon chip as compared to the reflectance of the bare fundus in the wavelength range.

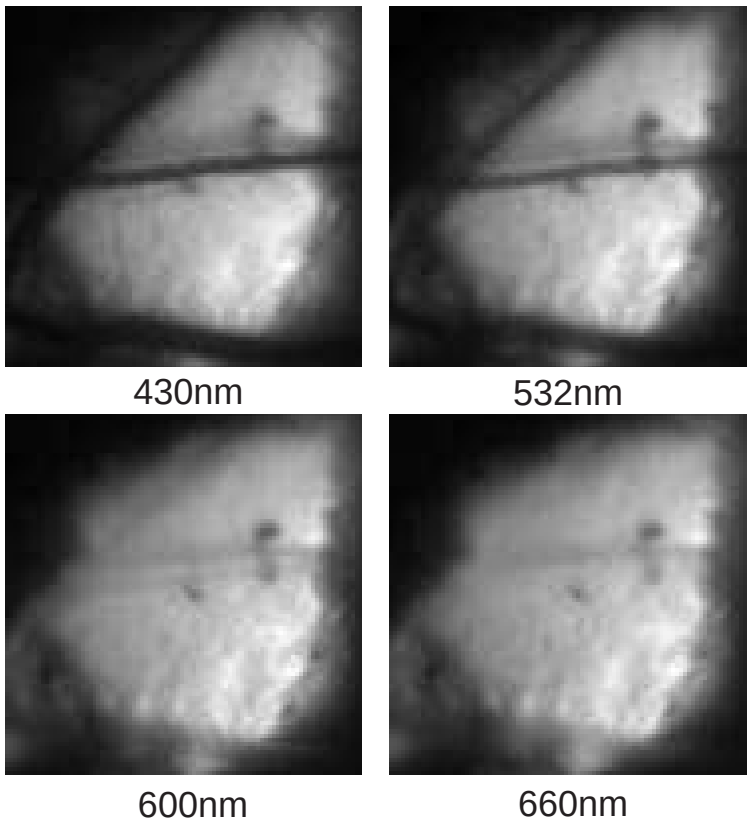

FIGURE 6.3. Spectral images of a vein/artery pair. The glint is substantially reduced. In the 600 and 660 nm red images the vessels are barely visible.

Vessel Intensity Profiles Insight into the wavelength dependent relative strengths of the four primary light paths introduced in Chapter 5 can be achieved by comparing

the spectral vessel profiles for the cases of bare fundus and subretinal Spectralon. The data analyzed for both cases was obtained for an inspired air mixture of 100% oxygen. In the top row of Figure 6.4, four spectral vessel profiles are shown for a crossection of an artery with bare fundus for 430nm, 532nm, 600nm and 660nm illumination wavelengths. The 430nm monochromatic image to the left of the profile shows the section of the vessel (the analysis region is highlighted by the superposed red rectangle) from which the intensity scan was obtained. The bottom row similarly shows the vessel intensity profiles for the vein at the same illumination wavelengths (again, the section of the vein is explicitly shown by the red rectangle superposed on the 430nm image). In both arterial and venous cases, the minimum intensity for the 430nm and 532nm wavelengths is found to occur at approximately the same pixel location, as annotated on Figure 6.4. To the left of this vessel apex, the vessel shadow is apparent as evidenced by a second local minima of slightly higher intensity. In contrast, for the red wavelengths (600 and 660nm), the vessel apex is the brightest structure on the intensity scan, brighter even than the background fundus located to the right of the vessel apex on the intensity profile.

Figure 6.5 similarly depicts the data obtained for the same vessels after the Spectralon was inserted beneath the sensory retina. Approximately the same region of the each vessel is analyzed for its intensity profile behavior. The behavior of the 430nm and 532nm is similar as to the case of the bare fundus, although the intensity profile for the subretinal Spectralon case is noticeably smoother. The very dark region to the extreme left of the vessel apex is due to the transition from the edge of the Spectralon chip to the bare fundus.

The vessel apex is readily apparent, as is the shadow to the left of the apex. The behavior of the intensity profile for the subretinal Spectralon case for the 600nm and 660nm illumination wavelengths is markedly different, however. For these illumination wavelengths, the signal strength from the vessel apex is approximately the same as for the adjacent Spectralon surface. This behavior is also seen in the multispectral

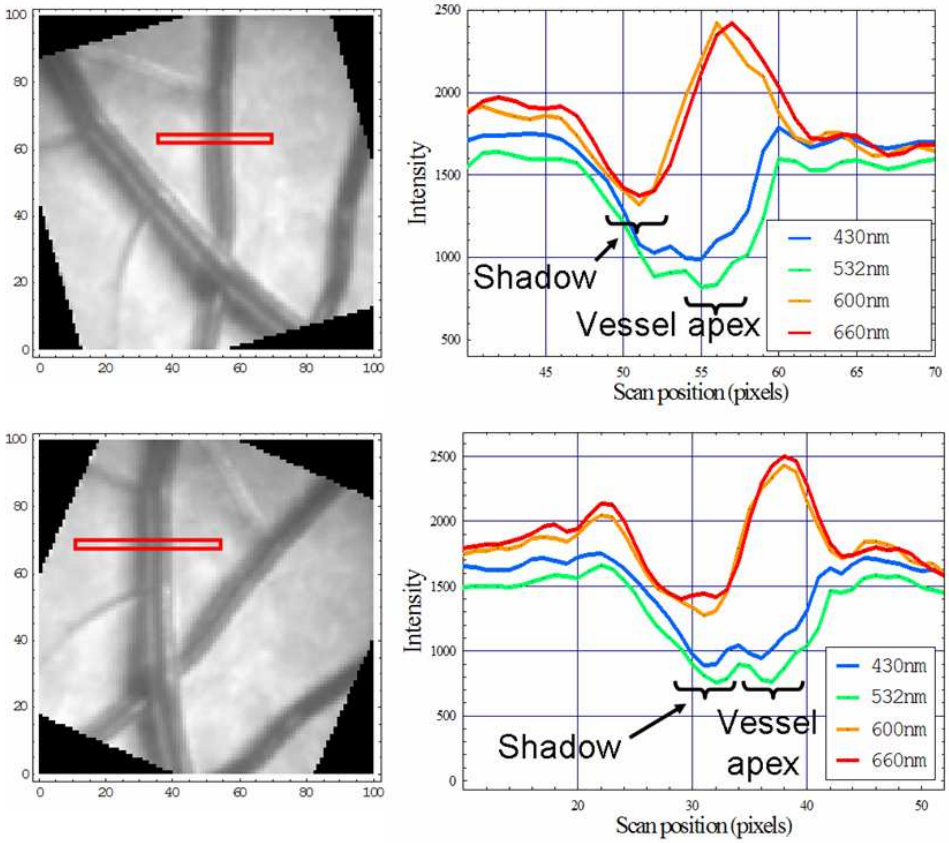

FIGURE 6.4. Vessel intensity profiles for four illumination wavelengths are shown above for the intact eye. The top row is arterial data and the bottom is venous data. The site from which the vessel intensity profiles were obtained is identified in the 430nm image to the left of the intensity profile plots.

images of Figure 6.3, in which the vessels appear to be transparent.

At first inclination, the vessel appears completely transparent to the red light illumination wavelengths and simply passes through with no vessel interaction to bounce off the Spectralon with the same intensity as the background. If this were true, however, then the corresponding behavior without Spectralon would not be possible. For the bare fundus data, the vessel region is brighter, which could not occur if the light simply passed through the vessel and scattered from the bare fundus and back

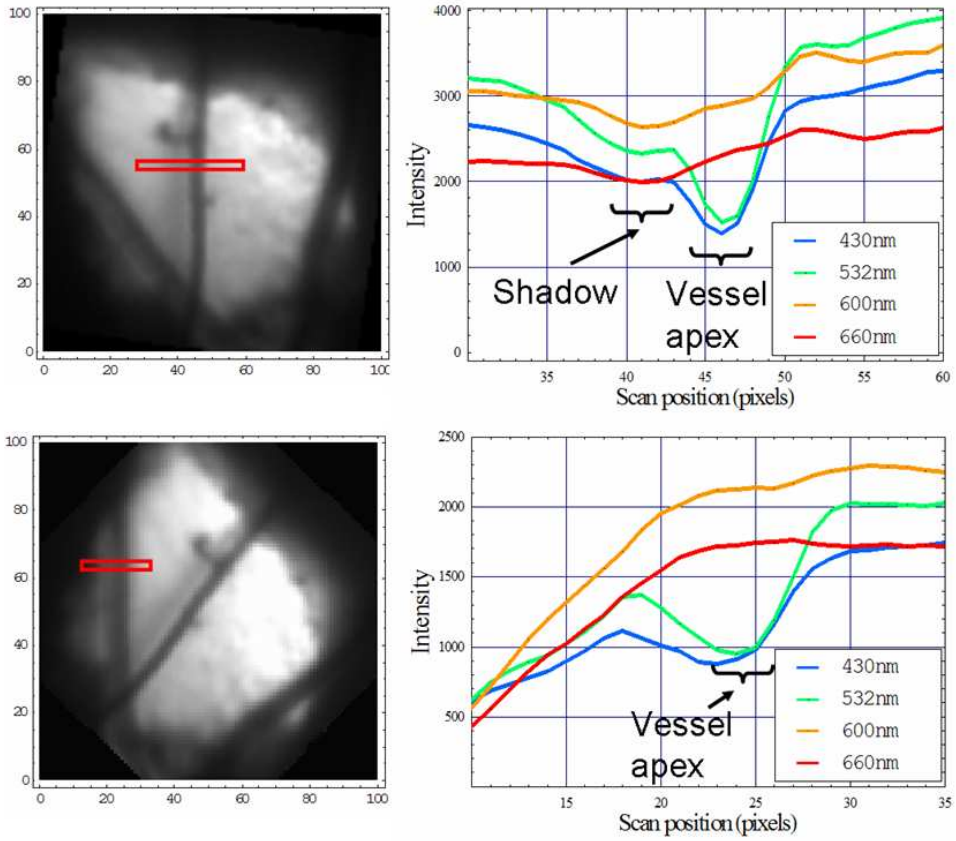

FIGURE 6.5. Vessel intensity profiles for four illumination wavelengths are shown above for the retina after the Spectralon chip was inserted under the sensory retina. The top row is arterial data and the bottom is venous data. The site from which the vessel intensity profiles were obtained is identified in the 430nm image to the left of the intensity profile plots. The data was taken for the same vessels as in Figure 6.4.

through to match the adjacent background intensity. It must be that some of the light reflects from RBC's. This behavior is also wavelength dependent, providing the conclusion that the S_4 spectra is the dominant spectra for the red wavelengths. For the oximetric calculation used in this research, the nonlinear fit was restricted to the 460nm-590nm spectral region in part to avoid the influence of this unknown dominant S_4 term.

One caveat to the conclusions drawn from this intensity profile analysis is that

the illumination conditions were not identical for the bare fundus and subretinal Spectralon cases. The wavelength dependent behavior of S_2 and S_4 spectra is likely illumination dependent. To remove this extra variable, future experiments should use collimated light at identical angles of illumination.

Spectral Analysis of Retinal Vessels Transmittance spectra were calculated at three artery sites and three vein sites along the vessels for both swine as shown in Figure 6.6. Spectra were averaged over 11 linear pixels as shown in Figure 6.6.

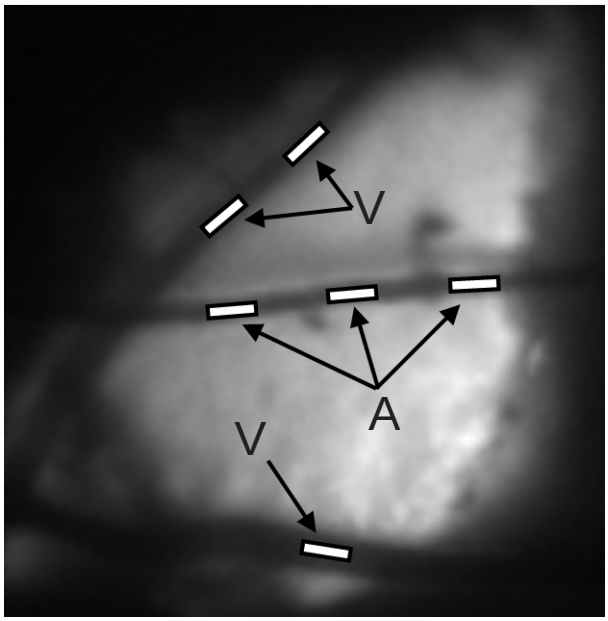

FIGURE 6.6. Analysis sites for the vessel pairs for Swine 1. Eleven pixels (shown as white bars overlaid on the retinal vessels) were averaged over each analysis location.

Normalized vessel transmittance spectra for the retinal artery and vein pair from one analysis site are shown in Figure 6.7 (artery with subretinal Spectralon) and Figure 6.8 (vein with subretinal Spectralon) for three inspired air mixtures. Each of the spectra shown in Figure 6.7 and Figure 6.8 corresponds to a different inspired air mixture delivered to the swine and is labeled according to the aortic and mixed

venous oxygen saturations measured from blood taken from the Swan-Ganz catheter at the time of spectral image acquisition.

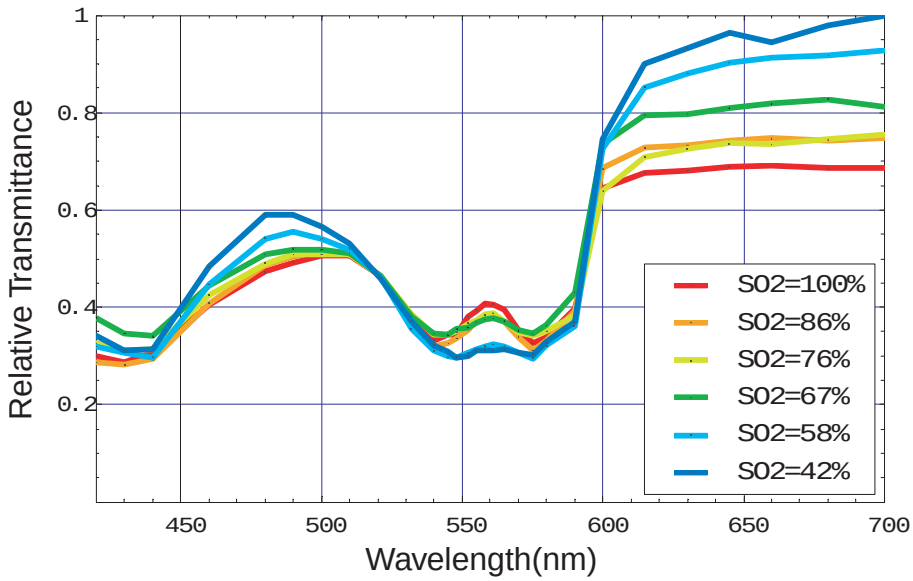

FIGURE 6.7. Relative transmittance measurements from the artery with subretinal Spectralon. The transmittances are normalized to an isobestic wavelength (518nm), and are color coded according to the legend with respect to the systemic arterial saturations measured with the ISTAT PCA.

The spectra for both the artery and the vein exhibit the typical characteristic spectral changes as the blood oxygen saturation level decreases: the local maximum in the 460-520 nm range shifts from 510 nm to 480 nm as oxygen saturation decreases and as the two minima at 542 nm and 577 nm begin to converge to a single broad minimum at 555 nm, characteristic of the transition of the spectra of oxyhemoglobin to deoxyhemoglobin. In addition, the spectra are remarkably smooth when compared with similar data from vessel over bare fundus (see Chapter 5 Figure 5.8).

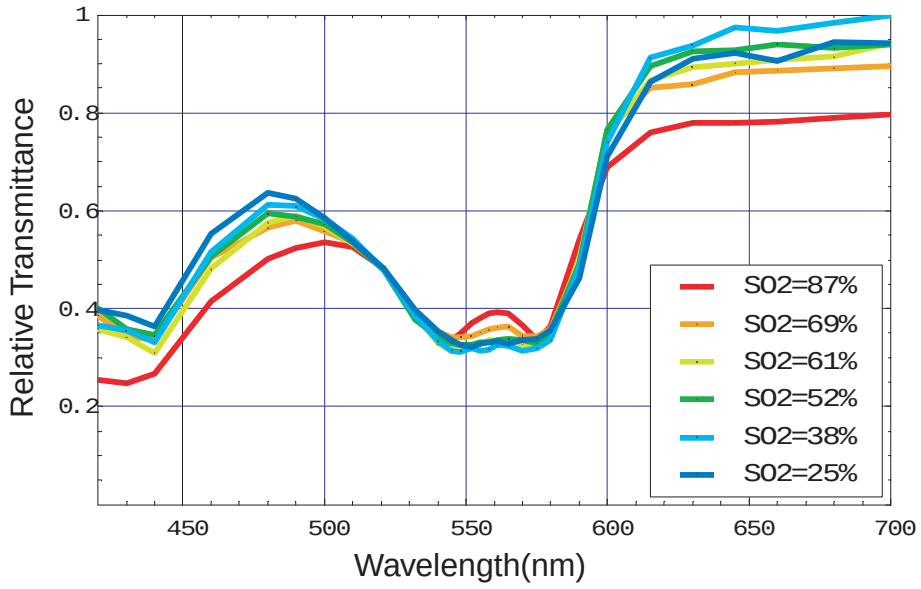

FIGURE 6.8. Relative transmittance measurements from the vein with subretinal Spectralon. The transmittances are normalized to an isobestic wavelength (518nm), and are color coded according to the legend with respect to the systemic venous saturations measured with the ISTAT PCA.

6.1.3 Determination of Oxygen Saturation

Figure 6.9 shows the results of retinal arterial and venous oxygen saturation measurements for the three analysis sites shown in Figure 6.6. In the plots, the retinal arterial and venous oxygen saturation is compared to the aortic or mixed venous oxygen saturation as measured with the co-oximeter. Error bars indicate the standard deviation among the three analysis sites.

6.1.4 Discussion

Correlation between systemic arterial oxygen saturation and retinal arterial oxygen saturation is comparable to that measured in Chapter 5 for the fundus *sans* Spectralon, with correlation of r^2=0.94. In addition, strong correlation is seen between the

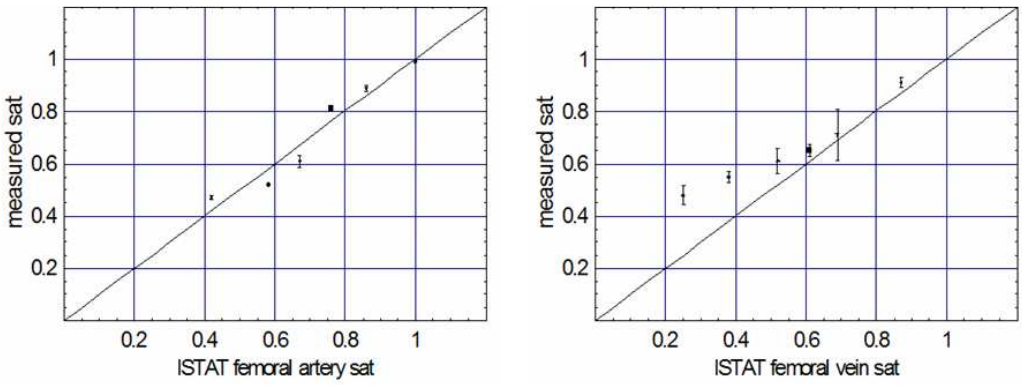

FIGURE 6.9. The average calibrated oxygen saturation measurements for the retinal artery and vein with subretinal Spectralon are shown in columns 1 and 2, respectively. The data are presented as the average calculated saturation for each inspired air condition vs the system artery vein saturation measured with the ISTAT PCA. Error bars are included the represent the standard deviation over the three measurements sites. The line y=x is included for comparison.

systemic venous saturation and the corresponding oxygen saturation measurements made on retinal veins (r^2=0.92). The maximum standard deviation in oxygen saturation calculation over the three analysis sites was 2.1% for the artery and 9.2% for the vein. As evidenced by Figure 6.4 and Figure 6.5, subretinal Spectralon intensity profiles were noticeably less noisy, perhaps contributing to the improved performance. Perhaps more likely, however, is that the somewhat unpredictable influence of the background fundus has been removed from the calculation.

6.2 Effects of Vitrectomy on Oximetry of Retinal Vessels

The unexpected poor correlation between systemic mixed venous blood oxygen saturation and retinal venous oxygen saturation found as a result of the research of Chapter 5 led to an additional swine experiment. This section describes an experiment on a third swine. The surgical methods and procedures were identical to those

TABLE 6.2. Decreasing arterial (top rows) and venous (bottom rows) oxygen saturation levels obtained for swine 3 previtrectomy

ISTAT measurements previtrectomy		
S_aO_2 (%)	PO_2 (mm Hg)	pH
100	493	7.459
99	129	7.424
87	55	7.375
62	33	7.393
S_vO_2 (%)	PO_2 (mm Hg)	pH
85	50	7.414
77	43	7.39
67	38	7.347
51	28	7.387

used for Chapter 5 except for one difference: multispectral images were acquired for systematically decreasing systemic oxygen saturation levels both before and after vitrectomy was performed.

6.2.1 Experimental Methods

Spectral images were obtained for Swine 3 for systematically decreasing oxygen saturation both before and after vitrectomy. Table 6.2 and Table 6.3 list the oxygen saturations and the pH levels measured with the ISTAT PCA for the data taken pre and postvitrectomy, respectively. After data was collected at the previtrectomy systemic oxygen saturation levels the animal was stabilized on 100% inspired air 30 minutes prior to vitrectomy. After vitrectomy, the data process was repeated for the oxygen saturation levels listed in Table 6.3.

TABLE 6.3. Decreasing arterial (top rows) and venous (bottom rows) oxygen saturation levels obtained for swine 3 postvitrectomy

ISTAT measurements postvitrectomy		
S_aO_2 (%)	PO_2 (mm Hg)	pH
100	401	7.453
99	111	7.484
97	80	7.48
92	60	7.451
83	46	7.444
S_vO_2 (%)	PO_2 (mm Hg)	pH
88	55	7.42
83	45	7.44
80	43	7.411
78	41	7.434
70	36	7.419

6.2.2 Experimental Results

Figure 6.4 shows four monochromatic images for the retinal field of view obtained for Swine 3. The artery and vein are identified in the figure.

As can be seen from the figure, strong displaced shadows were not achieved for this experiment. Three sites were analyzed for oxygen saturation in each vessel. These sites are illustrated in Figure 6.11. Spectra were averaged over 11 linear pixels for each site.

Vessel spectra are shown in Figure 6.12 for the pre and postvitrectomy cases. In both cases, the spectra are normalized to 518nm, an isobestic wavelength. Each of the spectra in the figures corresponds to a different inspired air mixture delivered to the swine and is labeled according to the femoral and mixed venous oxygen saturations measured from blood taken from the Swan-Ganz cathether at the time of spectral

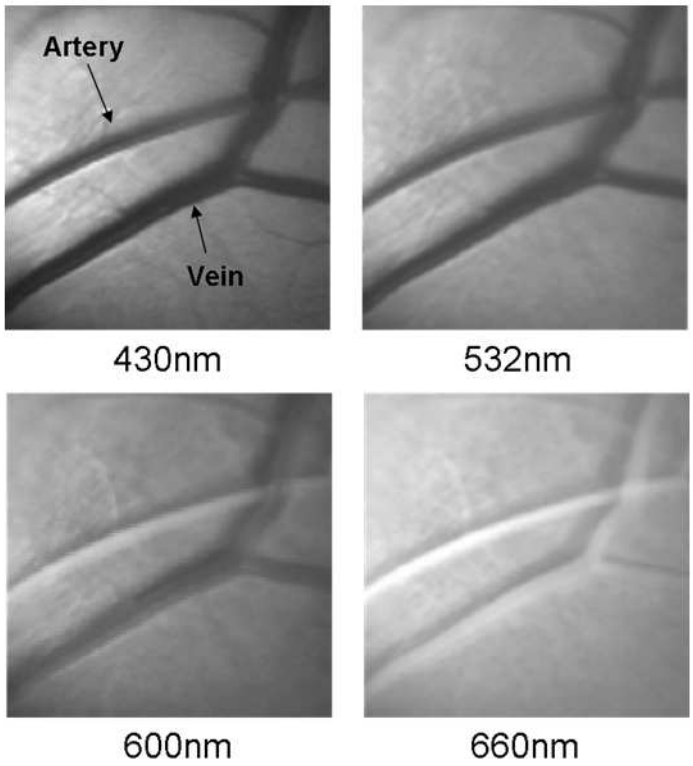

FIGURE 6.10. Spectral images of an artery/vein pair. The smaller vessel in this figure is the artery. Shadows are not as pronounced as those found in Chapter 5 due to the less oblique illumination direction.

image acquisition.

Vessel spectral analysis Figure 6.12a shows the vessel spectra constructed from the multispectral images taken previtrectomy for the artery (top plot in column *a*) and vein (bottom plot in column *a*). The curves are color coded to the systemic arterial and venous saturations as measured with the ISTAT PCA. The characteristic changes in spectra as blood oxygen saturation levels are decreased are seen for both the artery and the vein. First, the local maximum in the 460-520 nm range shifts from 510 nm to 480 nm as oxygen saturation decreases. Second, as saturation decreases, the two minima at 542 nm and 577 nm begin to converge to a single broad minimum at 555 nm,

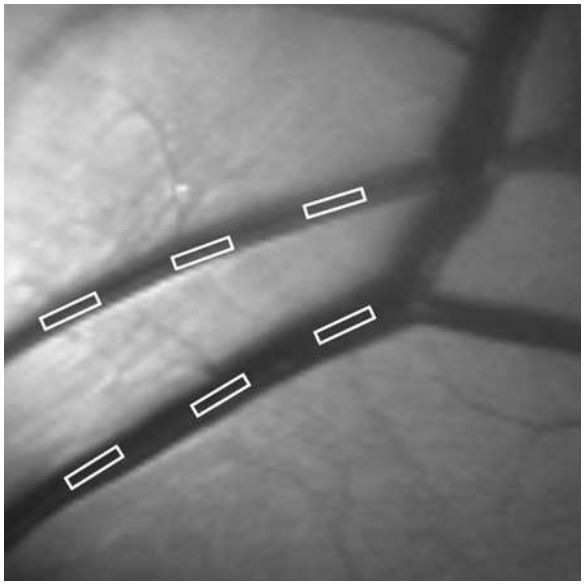

FIGURE 6.11. Analysis sites for the vessel pair imaged for swine 3. 11 pixels (white rectangles overlaid) were averaged to construct the spectra from each site.

characteristic of the transition of the spectra of oxyhemoglobin to deoxyhemoglobin.

Figure 6.12b gives the equivalent resulting vessel spectra for the artery and vein postvitrectomy (again, top row is the retinal arterial spectra and the bottom row is retinal venous data). In the postvitrectomy arterial spectra, the behavior described above is repeated: the vessel spectra changes predictably with decreasing systemic oxygen saturation to resemble the characteristic transmission spectra of deoxyhemoglobin. The retinal venous spectra shows unpredictable results, however. The data taken for the highest systemic venous oxygen saturation appears to resemble the characteristic spectra for deoxyhemoglobin more than spectra taken for lower systemic oxygen saturation calculations, as is readily apparent when comparing the spectra obtained for systemic venous oxygen saturation level of 88% (red curve, Figure 6.12b) and the spectra obtained for systemic venous oxygen saturation level of 80% (green curve, Figure 6.12b). This phenomena is discussed more quantitatively in the next section as it relates to the oxygen saturation calculation performed on the

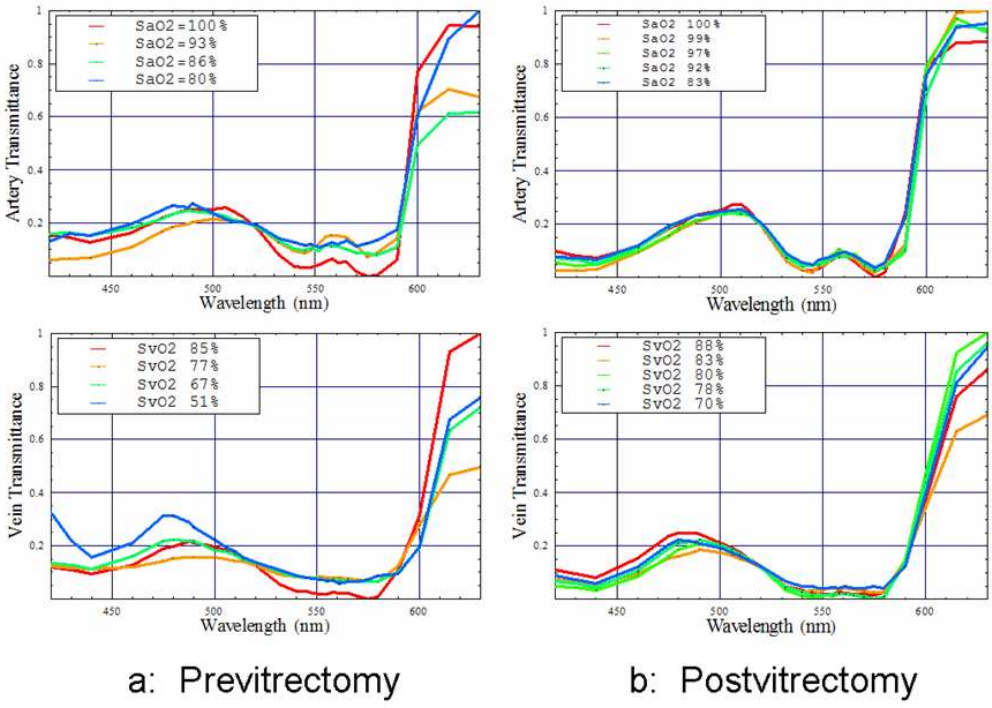

FIGURE 6.12. Vessel spectra for the artery/vein pair at one of the analysis sites shown in Figure 6.11. Column *a* shows the spectra calculated from data obtained pre-vitrectomy. Column *b* shows similar data taken postvitrectomy. The top row is arterial data and the bottom row is venous spectra.

vessel spectra.

Oxygen saturation calculations Figure 6.13 shows the results of retinal arterial and venous oxygen saturation measurements for Swine 3 for the cases of pre and postvitrectomy (Figure 6.13a and Figure 6.13b, respectively) where SO_2 has been averaged over the three analysis sites from Figure 6.11. In the plots, the retinal arterial and venous oxygen saturation is compared to the aortic or mixed venous oxygen saturation as measured with the co-oximeter. Error bars indicate the standard deviation among the three analysis sites.

For the previtrectomy case, both the measured retinal arterial and venous oxygen

saturation levels are relatively well correlated ($r^2 = 0.86$ and $r^2 = 0.87$, respectively) to the systemic arterial and venous oxygen saturation measurements. The error bars for the associated measurements are relatively large, however, with a maximum standard deviation of 6% for the arterial data and 8% for the venous data. It should be noted that the error bars are much larger than the results obtained for the analysis of the Swine 1 and Swine 2 of Chapter 5. The larger error bars are due most likely to the poor contrast achieved with these images and the subsequent difficulty in aligning the retinal images during postprocessing.

The oxygen saturation for the postvitrectomy arterial data is similar to the previtrectomy case. The curves were correlated to a similar degree ($r^2 = 0.83$), and the maximum standard deviation measured for the three sites was again 6%. The retinal venous data was not correlated with the systemic venous oxygen saturation measurements ($r^2 = 0.05$), and extremely large error bars are seen in the data for the three sites (maximum standard deviation was 18%).

6.2.3 Discussion

Vitrectomy does not appear to affect correlation between systemic arterial and retinal arterial blood oxygen saturation, as evidenced by the virtually identical results obtained for retinal arterial saturation in the previtrectomy and postvitrectomy cases. Vitrectomy does, however, appear to adversely affect the correlation between systemic and retinal venous blood oxygen saturation. Experiments on three swine consistently showed this effect, which occurs most likely do to a physiological change in the eye induced as a result of the vitrectomy. These results are preliminary; only one experiment was performed with decreasing oxygen saturation levels on an intact eye. Further research is necessary to corroborate the findings of this initial work.

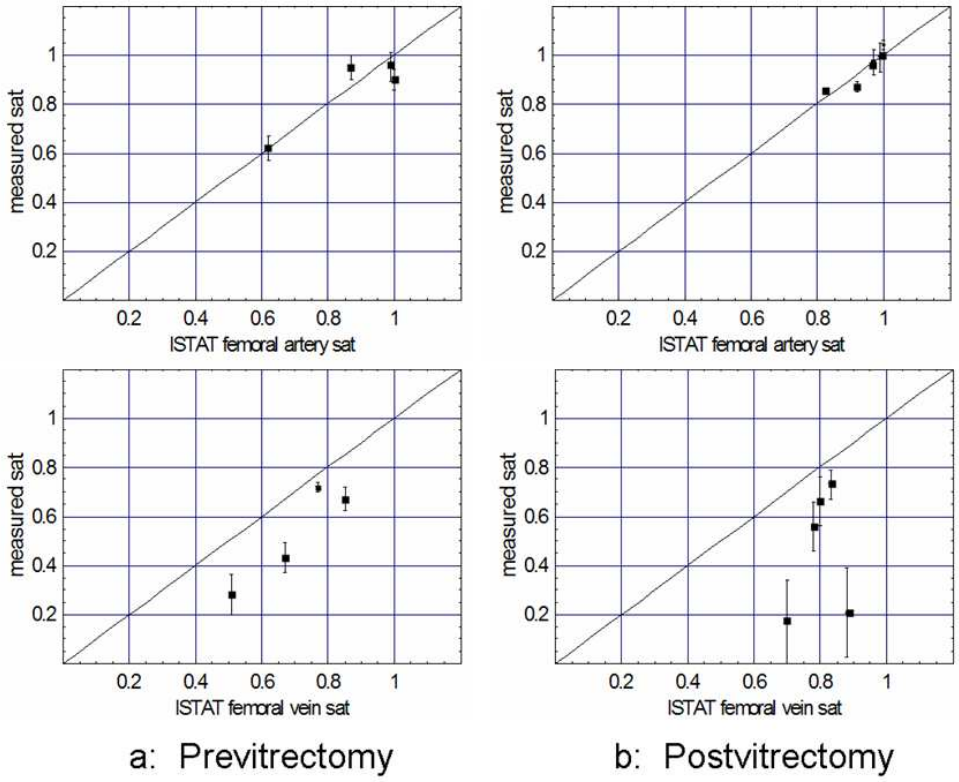

FIGURE 6.13. Vessel spectra for the artery/vein pair at one of the analysis sites shown in Figure 6.11. Column *a* shows the spectra calculated from data obtained previtrectomy. Column *b* shows similar data taken postvitrectomy. The top row is arterial data and the bottom row is venous data.

6.3 Summary and Conclusions

The results of Chapter 6.1 (oximetry performed with subretinal Spectralon) indicate a strong correlation between both systemic arterial and venous oxygen saturation with retinal arterial and venous blood oxygen saturation, respectively. These results appear contradictory with the results of section 6.2 because the Spectralon was inserted *after* vitrectomy was performed. At least two scenarios are possible to explain this apparent discrepancy. First, the length of time between the vitrectomy procedure on Swine

1 and the point in time at which data collection on subretinal Spectralon occurred could have minimized the affects of physiological changes induced by the vitrectomy procedure (as discussed in Chapter 5.3). The second possibility is that the accuracy of the oximetric calculation of the retinal vessel oxygen saturation was increased after the subretinal Spectralon chip was inserted, resulting in stronger correlation between retinal venous and systemic venous blood oxygen saturation. The former appears more likely, however, because the latter explanation should have affected arterial data as well as venous.

More research is necessary to establish the relationship between vitrectomy and correlation between systemic venous and retinal venous oxygen saturation. Further, it is likely more appropriate to evaluate the accuracy of retinal oxygen saturation measurement techniques applied to retinal arteries when a vitrectomy has been performed.

Chapter 7
Diffuse Fundus Measurements using Spectralon

This chapter focuses on the fundus spectroscopy of the live swine experiments. The spectral reflectance of fundus areas free of large vessels was measured. Spectralon was inserted both super and subretinally to isolate the spectral reflectance characteristics of the bare fundus and to provide a model for quantifying the amount of stray light encountered when imaging the retina and retinal vessels. Measurement of *in vivo* sensory retina transmittance was obtained.

7.1 Experimental Methods

Intravitreal surgery was performed on a 4 months old female American Yorkshire domestic swine. The experimental protocol was approved by the University of Arizona Institutional Animal Care & Use Committee (IACUC). The surgical preparation of the swine was performed as described in Chapter 5.

7.1.1 Fundus Imaging Apparatus and Data Collection

Multispectral imaging and data acquistion was performed as described in Chapter 5 so a description of these experimental techniques is not repeated here. Spectralon was placed on top and under the sensory retina for some of the multispectral data sets collected. Figure 7.1 shows the placement of the Spectralon subretinally.

7.1.2 Data Calibration and Image Alignment

A calibration data set was collected by measuring the output port of an integrating sphere illuminated with the fiber optic illuminator. The multispectral images were

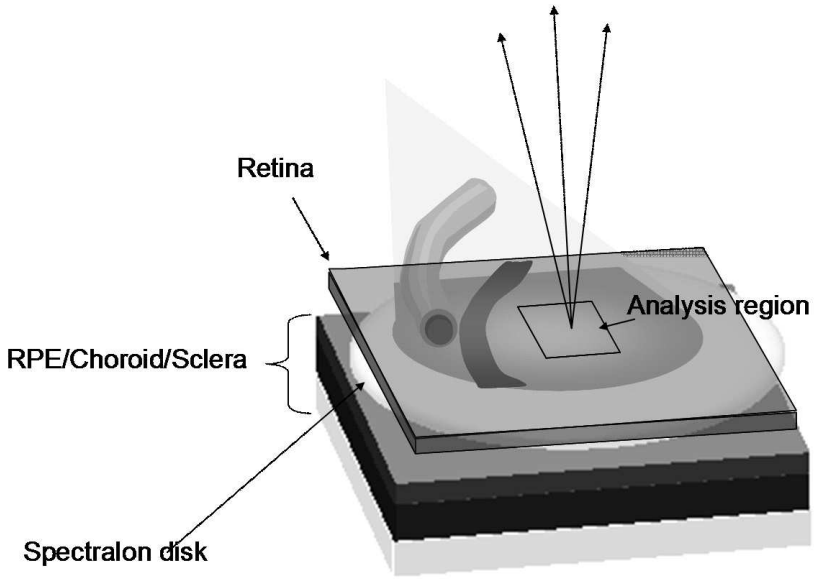

FIGURE 7.1. Illustration of the subretinal insertion of the Spectralon disk.

corrected for spectral variation in the light source and the spectral response of the CCD by dividing by the calibration spectrum. The inner wall of the integrating sphere is coated with Spectralon, which has a very uniform spectral reflectivity and is commonly used as a calibration standard. The fundus multispectral image sets were registered to correct for any relative motion between the swine fundus and the imaging camera which occurred during data collection. Images were aligned to within a fraction of a pixel using a bicubic spline interpolation in conjunction with a maximum mutual information merit function algorithm. [55]

7.1.3 Image processing and data analysis techniques

Three sites relatively free of large vessels were chosen for analysis of fundus reflectance for the four experimental conditions (Figure 7.2). The spectral signals captured by the imaging system were constructed for each image set by averaging the intensity values over a small region (150 by 150 microns) of the fundus contained in the FOV

for each of the 29 monochromatic images measured.

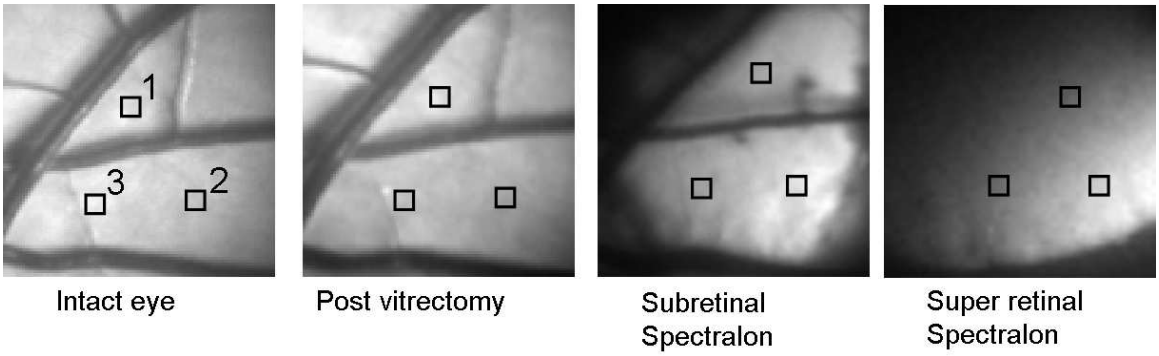

FIGURE 7.2. The 523nm image for each of the 4 experimental conditions is shown. Reflectance spectra were averaged over each of the analysis sites indicated in the image by the superposed squares.

The signal recorded by the CCD camera is a product of the spectral irradiance of the light source, the spectral response of the imaging system, and the spectral transmittance or reflectance of any structures that may interact with the light captured by the imaging system. This relationship is expressed in equation form for each of the four experimental conditions (S_{IE} the signal for the intact eye, S_{PE} the signal for the eye postvitrectomy, S_{sub} the signal for the subretinal Spectralon, and S_{super} the signal captured for the super retinal Spectralon) described above:

$$S_{IE}(\lambda) = P_{IE} * \Theta(\lambda) * R_{fundus}(\lambda) \tag{7.1}$$

$$S_{PE}(\lambda) = P_{PE} * \Theta(\lambda) * R'_{fundus}(\lambda) \tag{7.2}$$

$$S_{PE}(\lambda) = P_{sub} * \Theta(\lambda) * T_{SR}(\lambda) * R''_{fundus}(\lambda) * R_{Spectralon}(\lambda) \tag{7.3}$$

$$S_{PE}(\lambda) = P_{super} * \Theta(\lambda) * R_{Spectralon} * R''_{fundus}(\lambda) \tag{7.4}$$

P_i*$\theta(\lambda)$ is a multiplicative power term describing the spectral power distribution of the illumination and the spectral response of the imaging system. The P_i parameter represents the absolute power term and $\theta(\lambda)$ provides the relative spectral irradiance of the light illuminating a particular region of the fundus for each experimental

condition. P_i was not directly measured using this experimental configuration; the calibration process only measures $\theta(\lambda)$, the relative spectral power distribution. P_i parameter was estimated for each of the experimental conditions and the results are included in the paper.

The remaining terms are as follows: $R_{fundus}(\lambda)$ is the fundus reflectance, $R'_{fundus}(\lambda)$ is the fundus reflectance after vitrectomy, $T_{SR}(\lambda)$ is the transmittance of the sensory retina in double pass, $R_{Spectralon}$ is the reflectance of the Spectralon disk , and $R''_{fundus}(\lambda)$ is the reflectance of the fundus not shadowed by the Spectralon chip. Values for $T_{OM}(\lambda)$ were obtained from van de Kraats et al. [2] The reflectance of the Spectralon chip is Lambertian, so $R_{Spectralon}$ is constant with wavelength and equal to 0.91 for a 1mm thick piece of Spectralon.

Low pass filtering and light/fundus relative motion correction Despite attempts to immobilize the swine's head during data collection, small relative motion between the illumination beam and the fundus occurred as a result of the swine's breathing motion during data collection. This motion is secondary to the relative motion between the fundus and the camera, which was corrected for using the maximization of the mutual information as described in "Data Calibration and Image Alignment". Low pass filtered images reveal the relative motion between the illumination and the swine fundus; although the physical structures of the fundus were aligned for all the spectral images, the location of the peak illumination region varied among the spectral images. Figure 7.3 contains four filtered spectral images (420, 523, 560, and 680nm) from the image set obtained for the intact eye.

Frequency domain filtering with a Gaussian low pass filter was performed on each of the monochromatic images. The filter, H(ξ,η), is a Gaussian low pass filter with a spatial domain kernel size of 56 pixels for a 102 by 102 pixel image (FWHM = 56 pixels). In equation form, the low pass filtering of an N by N pixel spectral image

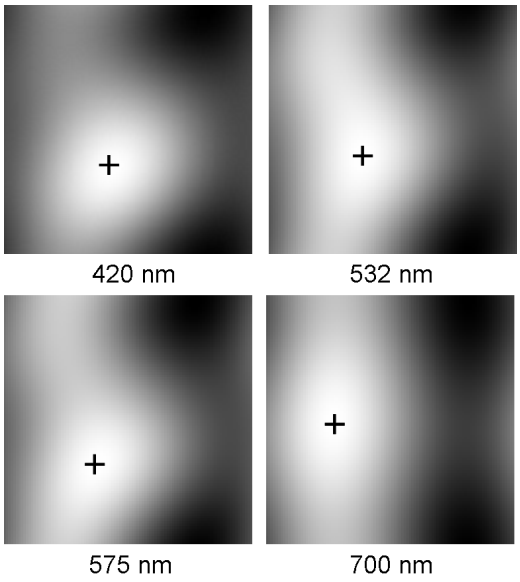

FIGURE 7.3. Four spectral images obtained for the fundus reflectance of the intact eye. The small cross on each image marks the location of the maximum intensity. The maximum intensity location varies spatially over the four images, indicating relative motion of the illumination cone of light with the reflecting surface (the fundus in this case). Each maximum corresponds to the axis of the fiber optic illuminator, or the peak intensity of the incident cone of light.

takes the form:

$$I(\xi,\eta) = \frac{1}{N^2}\sum_{x=1}^{N-1}\sum_{y=1}^{N-1} I(x,y)e^{-i2\pi*(\frac{\xi x}{N}+\frac{\eta y}{N})} \tag{7.5}$$

$$H(\xi,\eta) = exp(-\left[\frac{(\xi-\frac{N}{2})^2+(\eta-\frac{N}{2})^2}{2*\sigma^2}\right]) \tag{7.6}$$

$$I_{filtered}(x,y) = F^{-1}\{H(\xi,\eta)*i(\xi,\eta)\} \tag{7.7}$$

In 7.5 the frequency domain representation of the image, i(ξ,η) is obtained by applying the discrete Fourier transform (DFT) to the spatial domain image I(x,y). H(ξ,η) is the mathematical descriptor of the low pass filter, and $I_{filtered}$(x,y) is the filtered image. Frequency domain filtering is performed by multiplication of the frequency space image, i(ξ,η) by the filter, H(ξ,η). The inverse Fourier transform of the filtered

frequency domain image cube results in the filtered spectral images. Figure 7.4 shows the frequency (Figure 7.4a) and spatial domain (Figure 7.4b) representation of the filter:

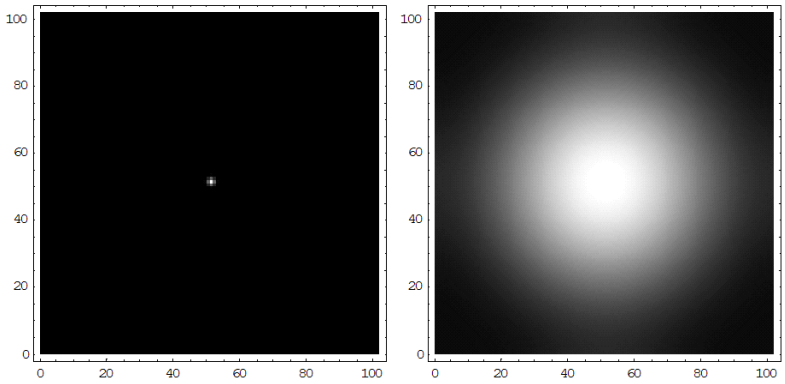

FIGURE 7.4. Low pass filter in the frequency (a) and spatial domain (b) (the convolution kernel).

The filtered images represent the lowest orders of the reflected light and map the position of the illuminating cone of light from the fiber optic illuminator. The beam centroid motion as a function of illumination wavelength is apparent in the filtered images (Figure 7.3). This small relative motion causes error in the measured spectrum, thus a correction algorithm was developed to correct for the difference in illuminating irradiance caused by the motion. The algorithm corrects the reflectance measured at a given analysis site in the following manner. In the filtered base image (552nm image for example), the ratio between the maximum of the image and the value at the analysis site is calculated, as well as the corresponding ratios for all the filtered images comprising the spectral image set. Based on the differences between the ratio for the base image and each remaining spectral test image, a correction factor, cf=r_{base}/r_{test} , is applied to the reflectance measured at the analysis site for each spectral image. The implicit assumption here is that the mode profile does not change appreciable over the visible spectrum. Figure 7.5 illustrates the results of the

motion correction for one of the reflectance curves.

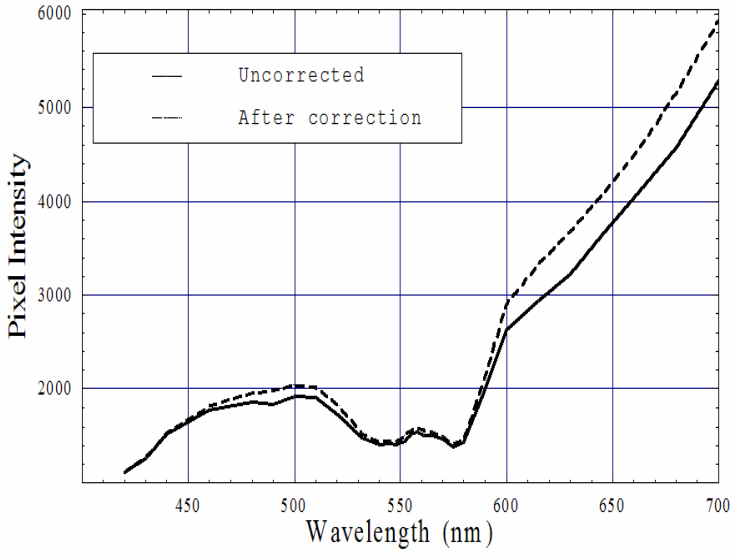

FIGURE 7.5. The plot above provides an example of the results obtained after illumination motion correction. The solid line is the signal recorded by the CCD, and the dashed line is the corresponding motion corrected spectra.

Relative spectral fundus reflectance Using Equations 7.1-7.4, the relative fundus reflectance can be estimated to within the multiplicative constant P_i as shown in Equa-

tions 7.5-7.8:

$$\Re_{fundus}(\lambda) = P_{IE} * R_{fundus}(\lambda) = \frac{S_{IE}(\lambda)}{\Theta(\lambda)} \tag{7.8}$$

$$\Re'_{fundus}(\lambda) = P_{PE} * R'_{fundus}(\lambda) = \frac{S_{PE}(\lambda)}{\Theta(\lambda)} \tag{7.9}$$

$$\Im_{SR}(\lambda) = P_{sub} * T_{SR}(\lambda) = \frac{S_{sub}(\lambda)}{\Theta(\lambda) * R_{Spectralon} * R''_{fundus(\lambda)}} \tag{7.10}$$

$$\Re''_{fundus}(\lambda) = P_{super} * R''_{fundus}(\lambda) = \frac{S_{super}(\lambda)}{\Theta(\lambda) * R_{Spectralon}} \tag{7.11}$$

The quantities described in Equations 8-11 constitute the relative spectral reflectances (or transmittance) measured for the four experimental conditions (relative spectral values denoted by script symbols). Relative reflectance spectra were calculated for the analysis sites shown in Figure 7.2 and are included in the Results section.

Power compensation: Estimation of absolute reflectance The constant term P_i in Equations 1-4 was calculated to provide a measure of the absolute fundus reflectance and sensory retina transmittance. A description of the calculation of P_i is provided for the case of the intact eye (the other three conditions were analyzed similarly). By taking the logarithm of 7.1, a set of linear equations for all λ_i can be formed:

$$Log_{10}\left[\frac{S_{IE}(\lambda)}{\Theta(\lambda) * T_{OM}(\lambda)}\right] = Log_{10}[P_{IE}] + Log_{10}[R_{fundus}(\lambda)], \tag{7.12}$$

where all known or measured terms are grouped on the LHS . An appropriate model $R_{fundus}(\lambda)$ provides an over-determined set of linear equations that can be used to solve for P_{IE}. $R'_{fundus}(\lambda)$, $T_{SR}(\lambda)$, and $R''_{fundus}(\lambda)$ can be similarly modeled and the resulting linear equations solved for P_i. A simplified fundus reflectance model was used to model the measured quantity for all four experimental conditions. Models

of fundus reflectance are based on the assumption that a finite number of reflecting, transmitting, and absorbing layers with known spectral extinction coefficients shape the spectral profile of light reflecting from the fundus. The primary ocular structures that contribute to the measured spectral signal are the ocular media (lens, cornea), hemoglobin and melanin, although several other absorbers in smaller concentrations are likely to be present. [32, 2] In equation form, the reflectance model is:

$$R_{fundus} = T_{OM}(\lambda) * A_{Hb}(\lambda) * A_M(\lambda) * A_{MP}(\lambda) \tag{7.13}$$

where T_{OM} is the transmittance of the ocular media, A_{Hb} is absorption due to blood (and is dependent on the oxygen saturation), A_M is absorption due to melanin, and A_{MP} is the absorption due to macular pigments. Figure 7.6 illustrates the absorption curves:

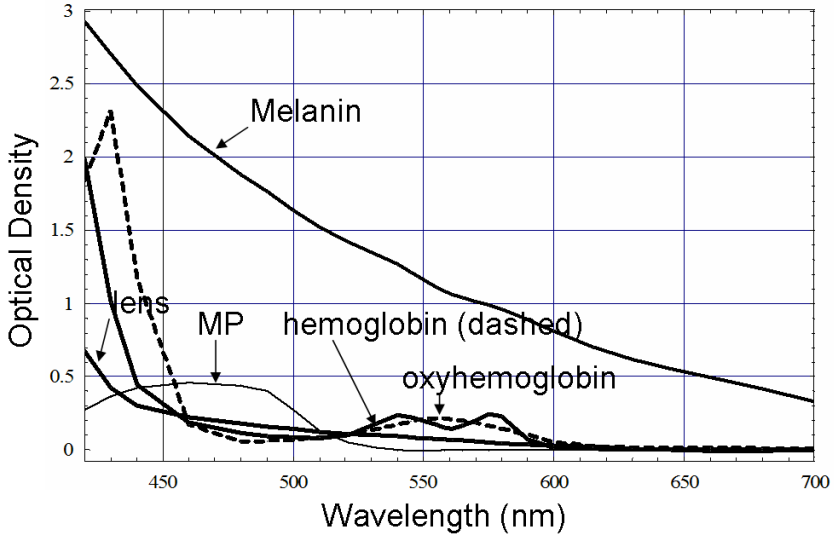

FIGURE 7.6. Optical density of the various spectrally absorbing structures of the eye. [1, 2]

Close examination of Figure 7.6 shows that for the wavelength range 575-700, the only components with substantial absorption are melanin and blood. Using the

fundus reflectance model in the afore mentioned wavelength range, 7.12 can then be rewritten to include the fundus reflectance model:

$$\hat{D}_{IE}(\lambda) = \hat{P}_{IE}\hat{A}_{Hb}(\lambda) + \hat{A}_M(\lambda) \tag{7.14}$$

$$\hat{A}_{Hb}(\lambda) = \varepsilon_{Hb}(\lambda) * c * d \tag{7.15}$$

$$\hat{A}_M(\lambda) = M(\lambda) * Y \tag{7.16}$$

where $\hat{D}$ represents the LHS of 7.12, the absorption due to blood is $\hat{A}_{Hb}$ (above and hereafter, the symbol $\hat{}$ denotes the base 10 logarithm of the quantity) and described by the product of the millimolar extinction coefficient (ϵ_{Hb}), the concentration of hemoglobin (c), and the effective interaction path length (d). The oxygen saturation of the blood in each of the four cases was calculated using the method described by Denninghoff et al. to be 85%, 52%, 92%, and 92% for the four cases and the corresponding millimolar extinction coefficients were used in 7.15. [68] $\hat{A}_M$ is the absorption due to melanin (found mainly in the RPE), which is a product of M, the millimolar extinction coefficient, and the relative concentration of melanin (Y). Writing 7.14 for the illumination wavelengths from 575-700nm provides a set of over-determined linear equations which was solved using the pseudo-inverse technique to provide the least squares solution for the P_i parameter.

7.2 Experimental Results

Relative and absolute reflectance spectra are presented in this section. Included are spectra calculated for the three analysis sites shown in Figure 7.2.

7.2.1 Diffuse relative reflectance measurements

Figure 7.7 shows that the measured relative fundus reflectance for the four experimental conditions: intact eye (a), postvitrectomy (b), subretinal Spectralon (c) and super retinal Spectralon (d). Figure 7.7a and Figure 7.7b show similar behavior for

the intact eye and the postvitrectomy data: reflectance is lowest in the blue light and increases until 510 nm for the intact eye and 480 nm for postvitrectomy. Oxyhemoglobin is evident by the appearance of bimodal local minima at 542 and 576 nm; these minima correspond to the absorption maxima of oxyhemoglobin. The reflectance increases by a factor of approximately 6 for all three curves in each plot in the 420-700nm range, and by a factor of approximately 2 for the 590-700 nm range. Figure 7.7c and Figure 7.7d show markedly different behavior, although some similarities exist. For both the sub and super retinal Spectralon, a local maximum exists at 510nm, and again, the oxyhemoglobin absorption spectrum is evident. The reflectance in this case however, reflectance increases by a factor of approximately 4 in the 420-700nm range, and a factor of approximately 1.75 in the 590-700 range.

7.2.2 Absolute diffuse relative reflectance measurements

Using the technique described in the Methods section, the relative reflectance data was converted to absolute reflectance by solving for the P_i terms from Equations 8-11. The results of the calculations for the reflectance curves measured at the three analysis sites are included in Table 7.1, and the power corrected curves are shown in Figure 7.8. The relative melanin Y values calculated for the intact eye and the postvitrectomy eye are much larger than the corresponding Spectralon values for all three locations in the data. This behavior is to be expected: the light striking both the subretinal and super retinal Spectralon should see only a small fraction of the melanin encountered for the first two conditions. In fact, the only avenue for melanin absorption in the super retinal Spectralon data is scattered light. The values obtained for the oxyhemoglobin c*d products correspond to a blood thickness interaction length of 40-100 microns.

The absolute reflectance data shown in Figure 7.8 is arranged such that the stacked plots in the left hand column display the data from the three analysis sites. For

TABLE 7.1. The results of the power correction parameters derived as per the description in the Methods section. The cd product gives a measure of the amount of blood at a test site, the Y term a measure of the amount of melanin, and the P term is the resulting absolute power term

Intact Eye				**Postvitrectomy**			
	c*d	Y	P		c*d	Y	P
Location 1	0.0049	0.669	9386	Location 1	0.0028	0.649	13489
Location 2	0.0070	0.655	9379	Location 2	0.0025	0.682	12990
Location 3	0.0054	0.644	9770	Location3	0.0016	0.634	13023
Average	0.006	0.656	9512	Average	0.002	0.655	13167
Std Dev	.001	0.013	224	Std Dev	0.001	0.024	279
Subretinal Spectralon				**Super retinal Spectralon**			
	c*d	Y	P		c*d	Y	P
Location 1	0.0049	0.221	76096	Location 1	0.0074	0.157	59206
Location 2	0.0036	0.175	88136	Location 2	0.0094	0.182	46814
Location 3	0.0033	0.231	71605	Location 3	0.0076	0.147	46284
Average	0.004	0.209	78612	Average	0.008	0.162	50768
Std Dev	.001	0.030	8548	Std Dev	0.001	0.018	7312

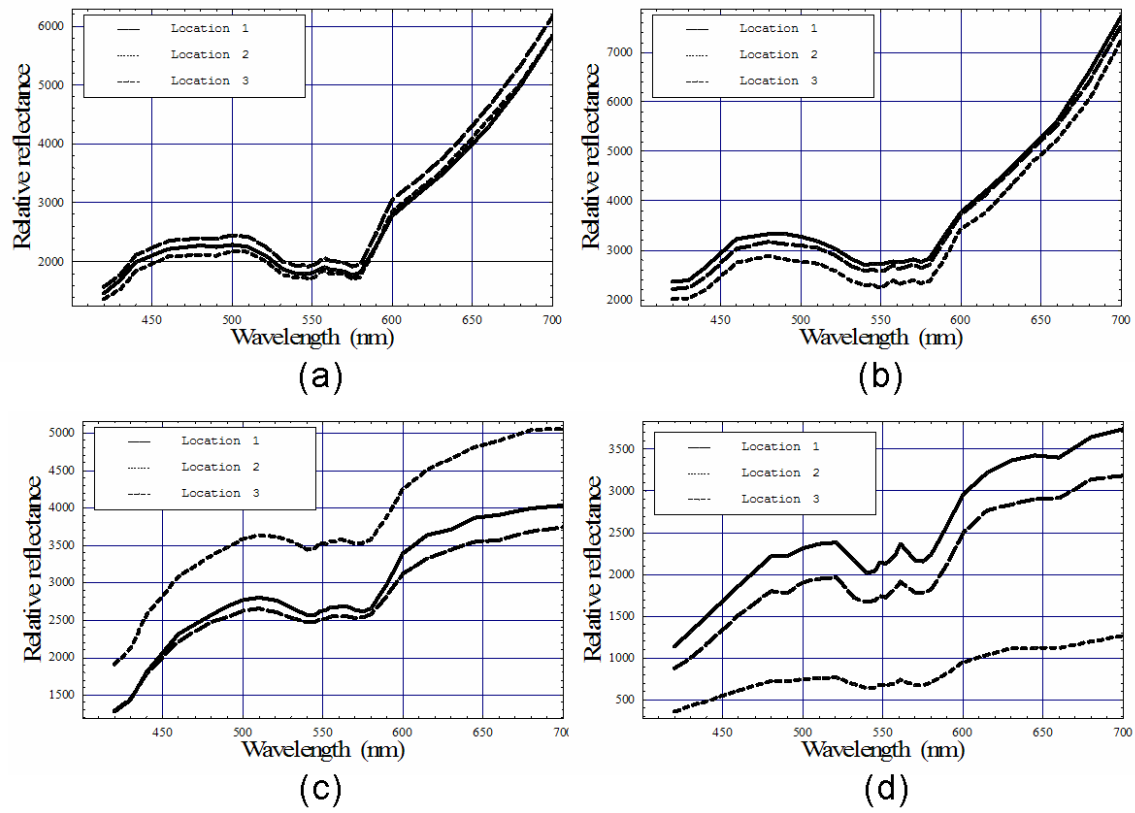

FIGURE 7.7. Relative reflectance measurements for (a) the intact eye, (b) postvitrectomy, (c) subretinal Spectralon, and (d) super retinal Spectralon.

all three locations, the reflectance for the first two cases is similar (intact eye and postvitrectomy), with the primary difference between the two curves being a difference in oxygen saturation (measured at 85% and 52%, respectively). The reflectance is approximately 17% at 420nm, rises to local maxima of approximately 25% at 497nm and 485nm for the intact eye and postvitrectomy eye, respectively. From there, both curves decrease to bimodal local minima at 542 and 576 nm, and then increase monotonically from a value of $\approx$ 30% at 590nm to $\approx$ 60% at 700nm. The subretinal Spectralon data shows more variation among the plots in Figure 7.8, ranging from a reflectance of $\approx$ 19-25% at 420. From this point, the reflectance increases to a local

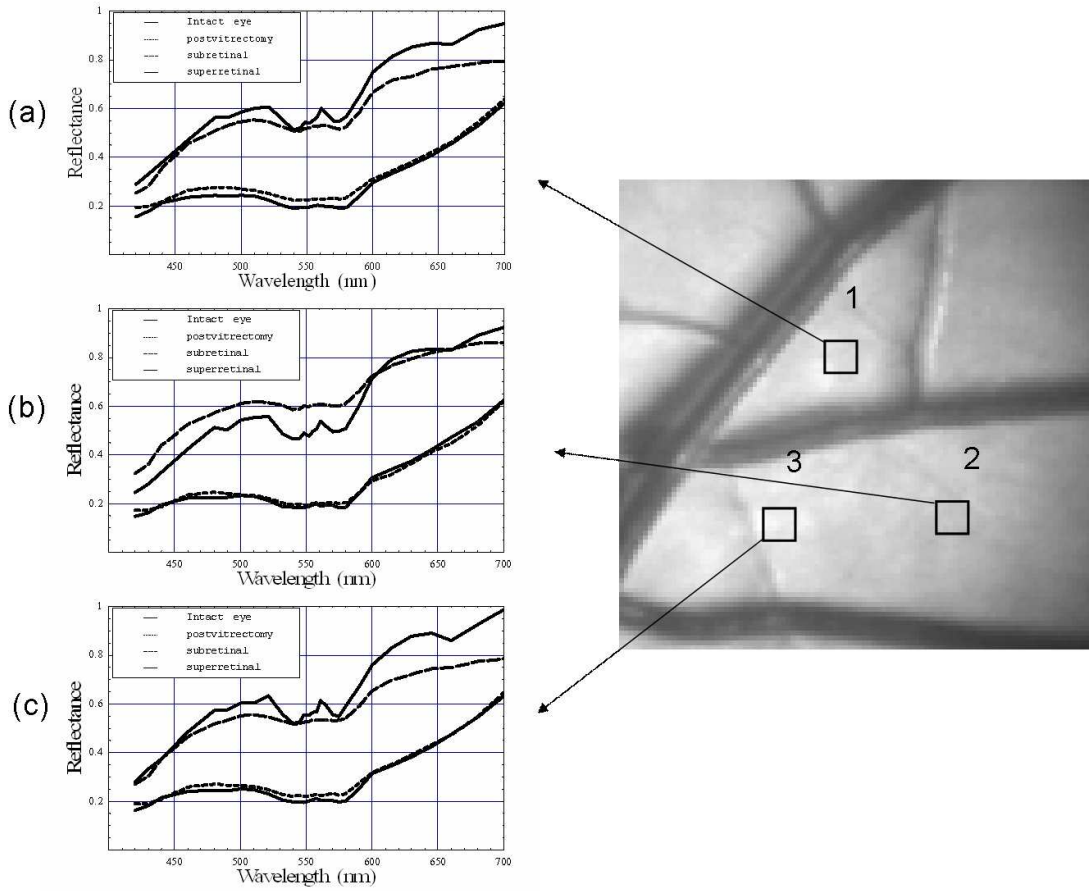

FIGURE 7.8. Absolute diffuse reflectance measurements at the three analysis locations (a-c).

maximum of ≈ 48-62% at 500nm. The characteristic bimodal maxima are located at 542 and 576nm. The reflectance again increases from the 575 -700nm range by 55-62% to 75-80%. The super retinal Spectralon spectrum contains considerably more noise than the other spectra, possibly due to the fact that the exposure time was lowered for data collection. The super retinal Spectralon should be the highest recorded reflectance spectra in all 3 cases of Figure 7.8, but in Figure 7.8b was corrected to a value lower than that of the subretinal Spectralon data. In most cases, however (Figure 7.8a,b,c) the super retinal Spectralon data recorded a higher reflectance.

The transmittance of the sensory retina in single pass can be obtained by taking the square root of the subretinal Spectralon data in Figure 7.8, which were taken in double pass. Figure 7.9 represents the transmittance of the sensory retina averaged over all three locations based on the power corrected Equation 7.10. The spectrum overestimates the influence of both melanin and hemoglobin due to scattered light from the globe. Equation 7.11 can be used, however, to calibrate for this scattered light term. By dividing 7.10 by 7.11, the scatter corrected in vivo transmittance of the sensory retina can be obtained. Figure 7.10 displays the expected transmittance of the sensory retina, i.e., essentially flat across the visible spectrum with an absolute transmittance >90% for all illumination wavelengths.

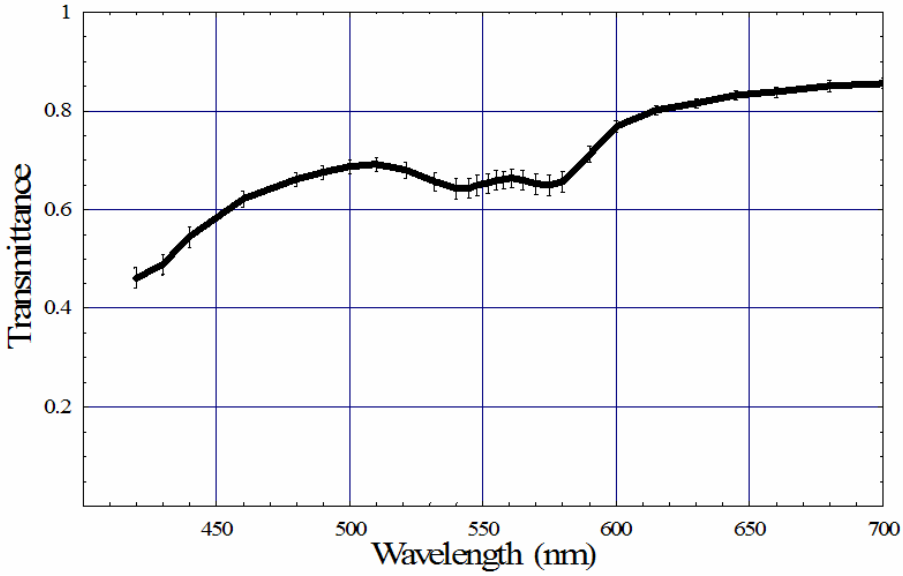

FIGURE 7.9. Single pass transmittance of the sensory retina, averaged over the three locations measured from the subretinal Spectralon data.

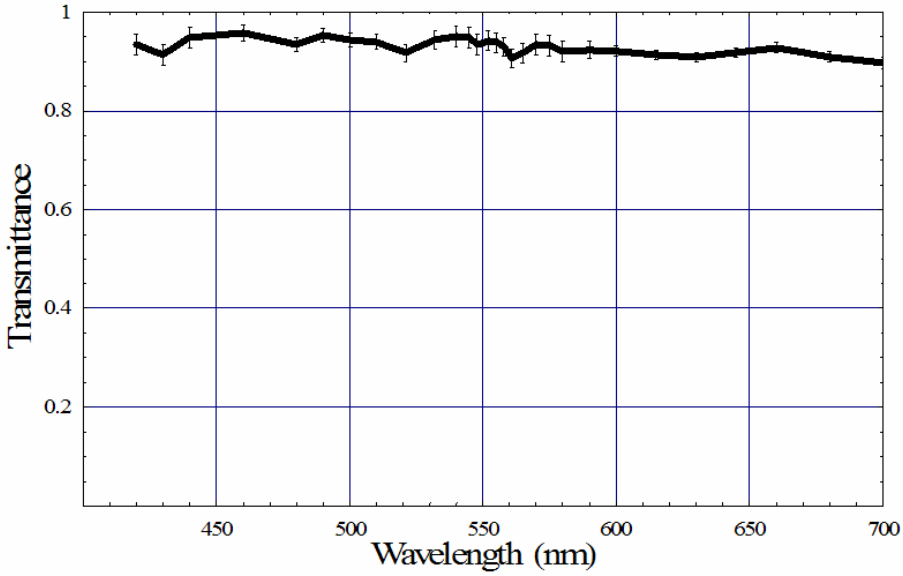

FIGURE 7.10. Single pass transmittance of the sensory retina, averaged over the three locations measured from the subretinal Spectralon data and corrected for the influence of scattered light using the super retinal data.

7.3 Discussion

The absolute measured reflectance in this paper is significantly higher than that found by other authors, although the spectral shape is similar. Explanations for this difference lie in the illumination and imaging method used in our study: intensity from a point on the fundus is integrated over a solid angle determined by the dilated pupil of the swine. The solid angle is proportional to the square of the pupil diameter, and is thus very sensitive to pupil size. Also, intravitreal illumination is a diffuse illumination technique which adds a large amount of scattered light to the measured signal. This illumination technique results in two effective light sources: the direct light from the fiber optic illuminator, and a glowing "integrating sphere" of illumination arising from scattered light. Figure 7.11 illustrates the two mechanisms that illuminate the fundus. The relative amount of this second "source" is unknown at this time; modeling this

system with an appropriate stray light analysis software package may help to provide an estimate of the magnitude of the contribution.

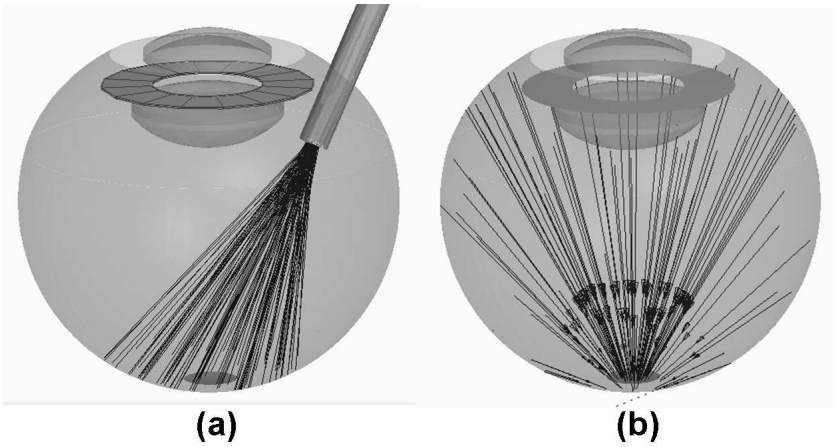

FIGURE 7.11. Illumination is produced on the test site by two mechanisms, illustrated in this figure. The first drawing illustrates the illumination proved directly by the fiber optic illuminator; the second shows the irradiance contributed by the glowing integrating sphere resulting from the scattered light.

The reflectance in the blue green wavelength range is much larger than can be explained based on our analysis with the ocular absorbers as the primary contributors to the spectral signal. As indicated in Figure 7.12, where the logarithm of the reflectance is shown superposed with the "model" reflectance determined using the calculated contributions of melanin and blood. The fit is very good for wavelengths longer than 550nm, but the reflectance is much larger than predicted in the blue region. The data indicates the presence of a relative reflector prior to the melanin layer that preferentially effects the blue region and is nearly transparent for wavelengths longer than $\approx$ 550nm. In addition, the discrepancy is much larger for the intact and postvitrectomy eye, indicating that this reflecting layer is posterior to the sensory retina, or is eliminated during retinal surgery.

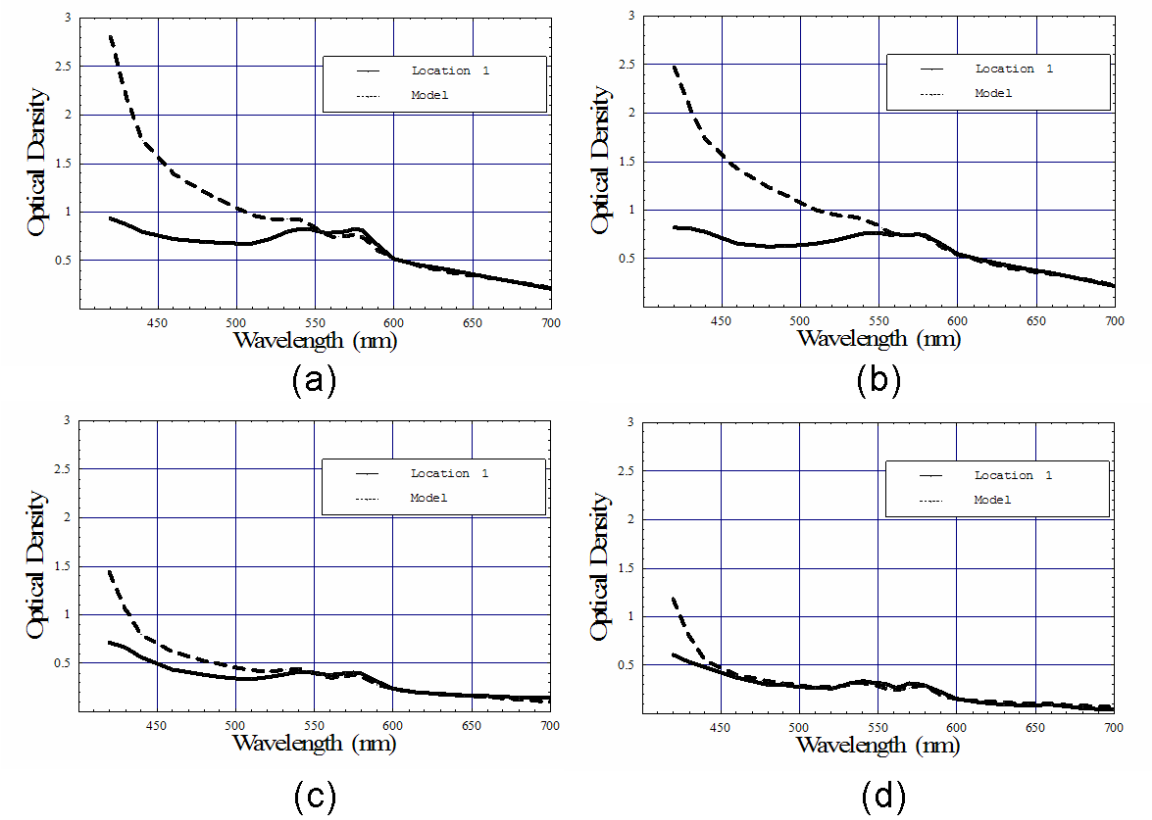

FIGURE 7.12. Measured log reflectance vs. the predicted reflectance based on Equation 12 for the (a) intact eye, (b) the postvitrectomy eye, (c)the subretinal Spectralon, and (d) the super retinal Spectralon.

7.4 Summary and Conclusions

Fundus reflectance measured using intravitreal illumination showed relative spectral behavior typical of past fundus measurements, but the absolute reflectance was 2-3 times higher than previously reported values. Pupil size strongly affects the amount of diffuse reflectance that is measured. In addition, the influence of scattered light could be a large contributor to the measured reflectance. The scattered light throughout the globe behaves like an integrating sphere and this physical phenomenon must be included in retinal spectroscopy model equations. The *in vivo* spectral transmittance

of the sensory retina was essentially flat across the visible spectrum, with an average transmittance $> 90\%$.

We have demonstrated the first in vivo sensory retina transmittance measurements and fundus reflectance measurements using intra ocular Spectralon as a calibration source. Intravitreal illumination effectively removed the contributions from extraneous reflections arising from light interaction with the anterior portions of the eye. The motion and power compensation techniques presented are general in nature and their use may extend to other illumination and data collection schemes.

Chapter 8

The Spectral Absorption and Transmittance Properties of Vitreous: The role of ascorbic acid

Chapter 8 presents the results of an experiment that measured the spectral transmittance of swine vitreous, vitreoretinal replacement fluid (BSS), BSS with various concentrations of ascorbic acid. Blue light absorption is known to cause damage to the retina and the role of vitreous as a protective filter is an important question for patients that undergo vitreoretinal surgery. This research aims to establish the role of ascorbic acid as the missing ingredient in normal BSS for blue light protection.

8.1 Blue light: physiological effects on the retina

The transparent anterior segment structure of the vertebrate eye spectrally filters light as it forms an image onto the retina. This filtering effect protects the retina from the deleterious effects of ultraviolet rays. [69, 70] The human retina is protected from short-wavelength UV rays by cornea and lens, which strongly absorb wavelengths shorter than 295 nm and 400 nm, respectively. [69] The cornea absorbs up to 97% of UV-B rays (270-320nm), and the crystalline lens absorbs the remainder of the UV-B radiation and in addition 94% of UV-A rays (320-400nm). [71, 72] The ageing crystalline lens also blocks potentially photo toxic blue light with end absorption extending to 500 nm. [69, 73, 74, 75] The aqueous humor absorbs UV-A in the range of 320 - 400 nm. [76] The human vitreous absorbs 20% of UV light at 350 nm and about 10% of blue light radiation between 400 nm to 500 nm. [73]

The absorption of the UV light by cornea, aqueous humor and vitreous has been attributed to the presence of ascorbic acid(AA). [77, 78, 12, 79, 80, 81, 82] The corneal

epithelium has the highest concentration of ascorbic acid followed by aqueous and vitreous humor. The concentration ratio of AA between corneal epithelium and plasma is as high as 300:1 [77], aqueous and plasma is (20:1) [78] and between vitreous and plasma is 10:1. [83] AA is evenly distributed within the human corneal epithelium and can absorb up to 77% of the UV-B and UV-C rays. [77] The work of Ringvold et al suggests the role of AA in absorption of shorter wavelength UV light by the corneal epithelium. They demonstrated a higher concentration of AA in the corneal epithelium of diurnal animals that encounter the highest environmental levels of UV radiation as compared to nocturnal animals. [80] They also observed higher level of AA in the pupillary area than in the periphery. [81] Reddy et al showed that the presence of AA in aqueous humor protects the lens epithelium against UV induced DNA damage. [82] Blue light (400-500 nm) can cause significant photo toxic damage to the retina similar to that caused by UV radiation. [84, 85] Noell et al demonstrated the damaging effects of visible blue radiation on the neurosensory retina and the pigment epithelium. [84] Ham et al showed that short exposure of 12 hours to intense light between 400-450 nm, termed "blue light hazard", can produce photo toxic damage to the retinal pigment epithelium (RPE). [85] Recent epidemiological studies have emphasized the role of blue light in the pathogenesis of Age Related Macular Degeneration (AMD). In particular, a survey of watermen in the Chesapeake Bay area concluded that chronic exposure to blue light may be related to the development of AMD. [86] Similarly, the Beaver Dam Eye Study showed that visible light rather than UV may be associated with AMD. [87] AA is an important antioxidant in the extracellular fluid and its major function is to scavenge free radicals and reactive oxygen species (ROS). It efficiently scavenges singlet oxygen radicals [88], hypochlorite [89], hydroxyl radicals [90], superoxide anions [91], etc. Since these radicals are implicated in a number of diseases, AA is used to treat diseases where oxidative stress is involved. [92] Presence of AA within ocular structures such as vitreous humor offers significant antioxidant protection to the retina by suppressing free radicals generated

through photo oxidation via exposure to sunlight. [93]

The current study was undertaken to compare the spectral transmittance properties of BSS Plus to those of in vitro vitreous, and to further investigate the transmittance properties of BSS Plus as a function of AA concentration. This study is of importance as BSS Plus is commonly used as a vitreous substitute following retinal surgery, and studies have not been done to determine whether the protective blue light filtering properties of the eye have been compromised as a result. The chemical composition of BSS Plus is different from that of vitreous; of particular interest to this study is the absence of ascorbic acid. In this study, the spectral transmission of BSS Plus is analyzed in the range 420 to 700nm and compared with that of in vitro porcine vitreous. Porcine vitreous is readily available and the extensive similarities between human and porcine eyes have been noted. The transmittance of mixtures of BSS Plus and ascorbic acid solution was measured as a function of AA concentration.

8.2 Materials and Methods

All experiments were conducted in accordance with the ARVO statement for the use of animals in ophthalmic and vision research.

8.2.1 In Vitro transmittance experiment

Freshly enucleated eyes from four American Yorkshire domestic swine were obtained from the University of Arizona Meat Sciences Laboratory. The conjunctiva and extraocular muscles were separated from the globe. The globe was cut through the pars plana and the vitreous was extracted and then deposited into a rectangular (20mm by 10mm) glass cuvette (Starna Cells, Inc., Atascadero). The time interval between enucleation and collection of vitreous sample was under 2 hours. The volume of the vitreous sample collected from each eye was approximately 4 ml. Care was taken to

prevent the spilling of pigments into the sample. The cuvette containing the vitreous sample was positioned at the exit port of an integrating sphere [Labsphere] that was illuminated by light from a scanning monochromator (Oriel Spectral Luminator, Irvine) coupled to a fiber optic illuminator (Alcon Laboratories, Fort Worth). The path length through the cuvette was 10mm. The spectral resolution of the monochromator was approximately 10 nm. A 12 bit scientific grade CCD camera (Hamamatsu Orca-AG, Hamamatsu City, Japan) with a 3.3X macro zoom lens (Edmund Scientific 56-524, Edmund Scientific, Barrington) was used to image the front surface of the cuvette. The peak wavelength was stepped from 420 nm to 700 nm and an image of the target area was acquired at illumination wavelengths of 420, 430, 440, 460, 480, 490, 500, 510, 521, 532, 540, 545, 548, 552, 555, 558, 561, 565, 570, 575, 580, 590, 600, 615, 630, 645, 660, 680, and 700nm. A dark image (obtained with the shutter closed) was subtracted from each image upon acquisition to correct for dark current and external light sources. The cuvette was emptied and a spectral image of the empty cuvette was obtained to be able to calibrate and correct for the spectral properties of the experimental setup. Spectral images were obtained for vitreous samples extracted from eight enucleated swine eyes. All images were obtained under dark room conditions. Figure 8.1 illustrates the experimental setup used to acquire the spectral images.

8.2.2 Ascorbic Acid Experiments

Ascorbic acid (1000 mg /2 ml) ampoules were purchased from Abbott Laboratory, IL (Batch number NDC 0074-3397-32). The BSS Plus/ascorbic acid solution measurements were performed under dark conditions to minimize the effects of stray light on ascorbic acid oxidation.

Ascorbic acid was added to BSS Plus to achieve a concentration of 1.2 mol/ml , which is the reported concentration of ascorbic acid in porcine vitreous. [94] Similar concentrations have been reported in human vitreous in patients with premacular

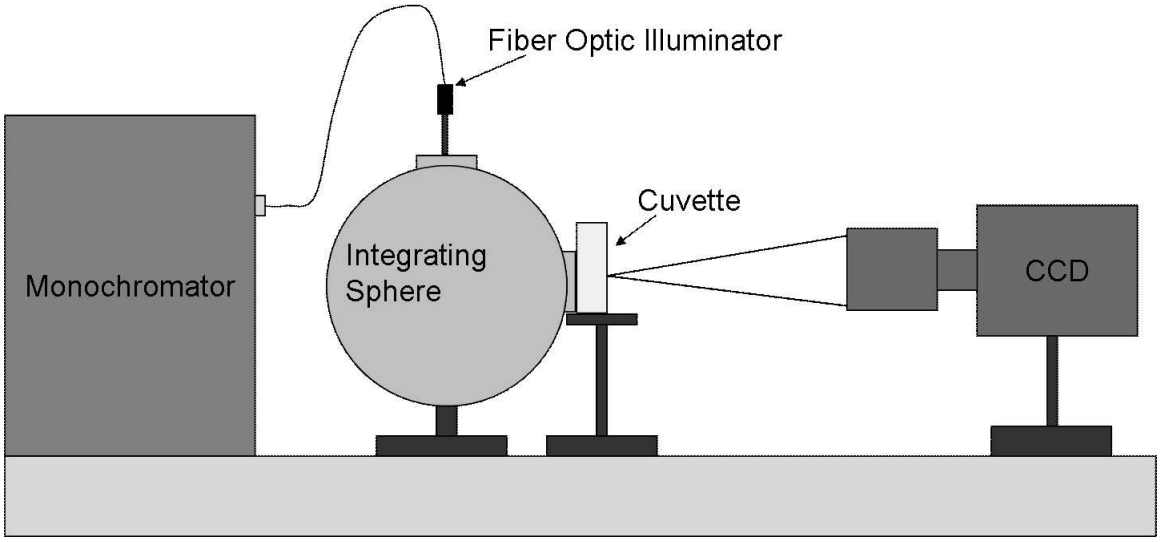

FIGURE 8.1. The experimental setup used to acquire multispectral images. Illumination was provided by the exit port of the integrating sphere.

fibrosis. [95] The solution (4 ml) was transferred to the cuvette and multi spectral images were obtained at the same series of wavelengths as for the in vitro vitreous transmittance measurements. The sample was discarded and the cuvette was cleaned. The experiments were repeated with three higher concentrations of ascorbic acid: 3.6 mol/ml (3X), 7.2 mol/ml (6X), and 10.8 mol/ml (9X). All the experiments were performed as triplicates.

8.2.3 Data Calibration and Analysis

The multispectral images were corrected for spectral power variation in the light source, spectral response variation in the CCD and spectral transmittance of the glass cuvette by measuring the spectral transmittance of the empty cuvette in the experimental geometry. Mathematica was used to analyze the multispectral images. Figure 8.2 shows a typical monochromatic image with four pigment-free analysis sites identified by black outline squares. The small black specks in the image are pigment

fragments within the vitreous.

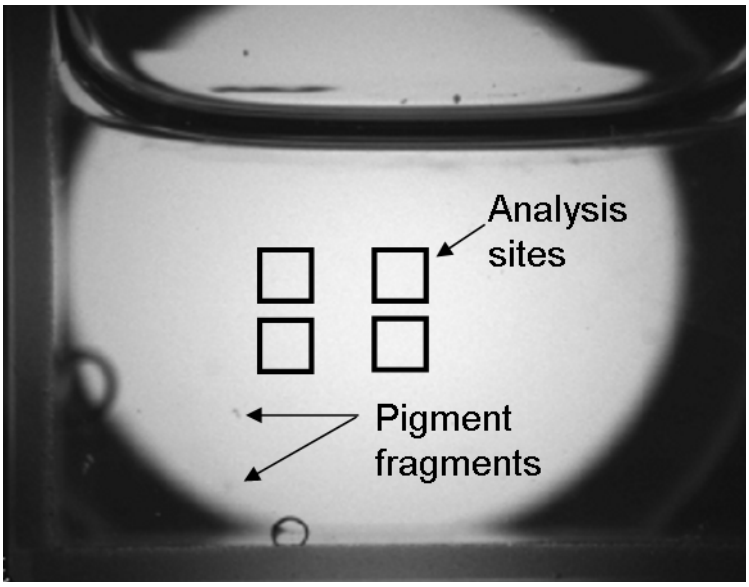

FIGURE 8.2. Enucleated vitreous in glass cuvette. The illumination wavelength was 420 nm. Black squares (each 252 pixels) indicate 4 analysis sites over which transmittance was averaged. Areas with black specks were avoided in the selection of measurement areas. The dark area at the top of the image is the vitreous meniscus.

For a given dataset, the intensity measured by the CCD camera from four pigment free areas of each spectral image was used to construct the spectral profile of the sample in the following way. First, each of the four analysis sites (25 x 25 pixels) was averaged to give a site average intensity, and then all four site average intensities were averaged to obtain an overall intensity average. This overall intensity average at each wavelength was used to construct the average uncorrected vitreous transmittance for a given vitreous sample.

This data analysis process was repeated for each experiment: enucleated porcine vitreous, BSS plus, BSS plus/ascorbic acid solutions, and empty cuvette. A corrected spectral transmittance was calculated from each uncorrected spectrum by dividing by the empty cuvette (calibration) spectrum.

$$S_{corrected}(\lambda) = \frac{S_{uncorrected}(\lambda)}{S_{calibration}(\lambda)}. \quad (8.1)$$

8.3 Results

8.3.1 In vitro vitreous spectral analysis:

Figure 8.3 shows the averaged normalized spectral transmittance of in vitro vitreous of eight porcine eyes. Error bars indicate the standard deviation calculated from the 8 measured values at each illumination wavelength. The transmittance of light was in the range of 91-92% between 420-450 nm. There was a 2% increase in transmittance from 450 nm to 500nm. The transmittance reached a maximum at around 615 nm and there was a decline in transmittance between 650 and 700 nm to approximately 96-98%. The 420-575 nm region of the transmittance spectrum showed a standard deviation that was a factor of 2 larger than that of the 580-700 nm range.

8.3.2 Spectral transmittance of BSS Plus:

Figure 8.4 shows that BSS Plus has a very uniform spectral transmittance of about 99% throughout the visible region, with a very small standard deviation (approximately 0.1%). The top curve in the figure indicates the spectral transmittance of BSS Plus and is overlaid on the curve depicting the spectral transmittance curve for the averaged in vitro vitreous transmittance. The BSS Plus transmittance is more similar to the vitreous transmittance in the 600 nm to 700 nm range.

8.3.3 Spectral transmittance of BSS Plus with physiological ascorbic acid level:

The spectrum of AA shown in Figure 8.5 shows a decrease in the transmittance of blue light by 4 -5% between 420 nm to 450 nm. AA did not appreciably change the

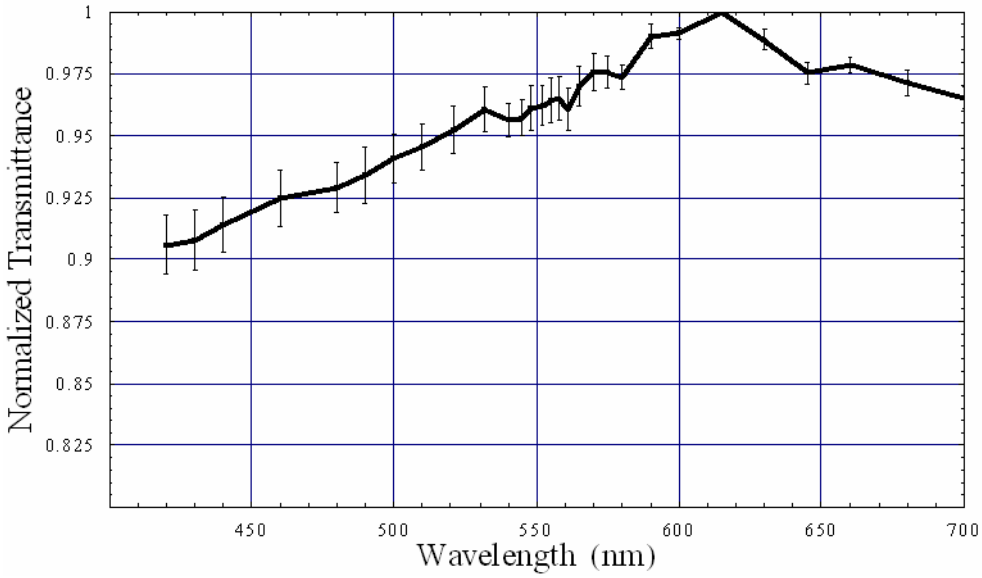

FIGURE 8.3. In vitro vitreous transmittance. The spectral transmittance curve represents the average over vitreous samples from 8 eyes. Error bars indicate the standard deviation over the 8 samples.

transmittance of BSS from 500 nm to 700 nm .

8.3.4 Spectral transmittance of BSS Plus with Higher concentration of Ascorbic acid:

Figure 8.6 indicates that ascorbic acid in BSS Plus decreases the transmittance of blue light in a dose dependent manner. In this figure, superposed are the spectral transmittance curves for the following concentrations of AA in BSS Plus: 1.2 mol/ml (physiological concentration of AA in vitreous), 3.6 mol/ml (3X), 7.2 mol/ml (6X) and 10.8 mol/ml (9X). All four curves show similar relative behavior across the visible spectrum beginning with the lowest transmittance in the 420-450nm range. The transmittance gradually increased to at 450 nm and remained stable to 480 nm. The transmittance gradually increases from 500-600 nm. The transmittance pattern is similar between the four levels of ascorbic acid beyond 600 nm. Decreased trans-

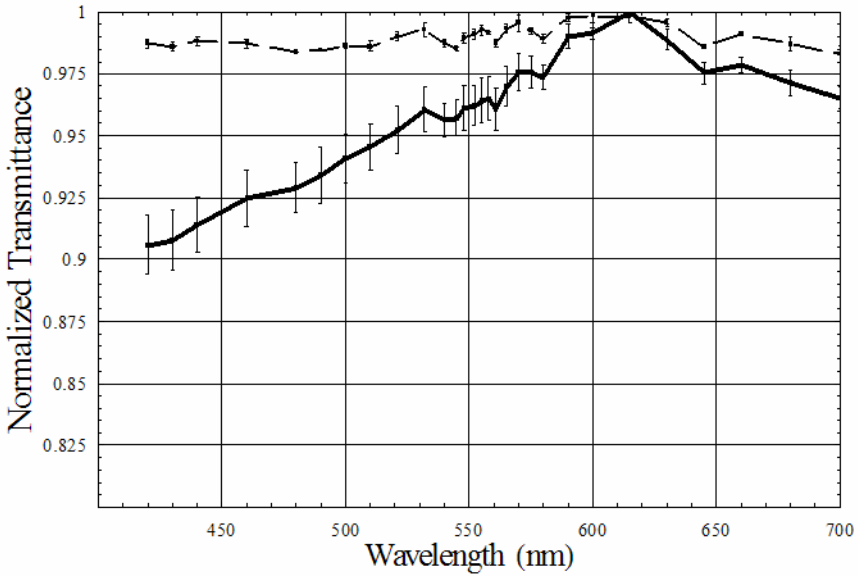

FIGURE 8.4. BSS Plus (dashed curve) and average vitreous transmittance (solid curve).

mittance in the 400-480nm range is apparent in all four curves and may be directly dependent on AA concentration.

8.4 Discussion and Conclusions

The optical transmittance of the in vitro porcine vitreous measured with our technique is in good agreement with published data of the transmittance of human vitreous measured with a spectrophotometer. [73] The higher standard deviation observed in the blue light range indicates a large variation in absorption of blue light by the vitreous, possibly due to the additional effect of scatter in the blue light region. The decreased spectral transmittance of blue light by the vitreous is likely due to the presence of ascorbic acid, amino acids like tryptophan and tyrosine, and hyaluronic acid. [79] Our data indicates that ascorbic acid plays a significant role in the heightened absorption of light in the 420-450 nm range in the vitreous.

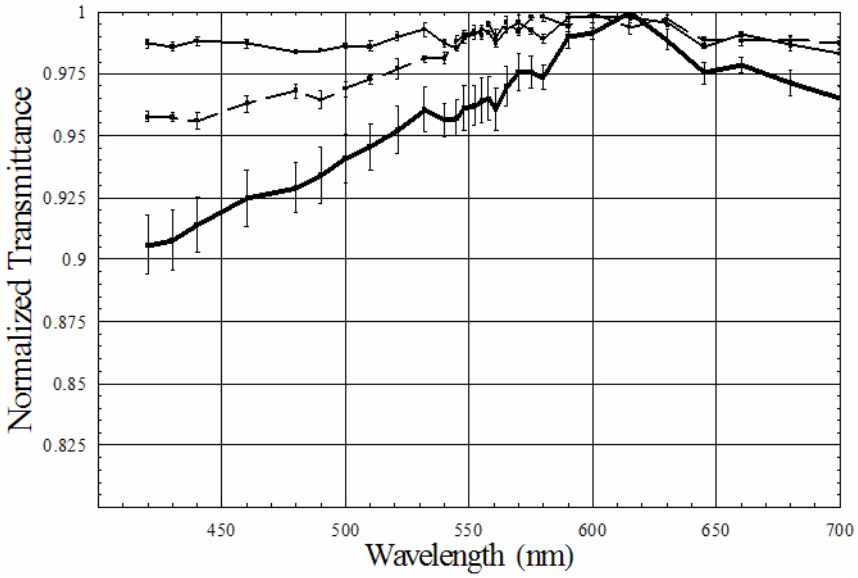

FIGURE 8.5. Spectral transmittance of 10 mm of BSS Plus (solid thin curve), BSS Plus 1.2 mol/ml ascorbic acid (dashed curve), and for in vitro porcine vitreous (solid thick curve).

BSS Plus is a commonly used substitute for vitreous during retinal surgery. The question that motivated this study is simply: does BSS Plus increase the intensity of blue light at the retina of a vitrectomy patient? The spectral transmittance data show that BSS Plus transmits uniformly across the visible spectrum. Addition of ascorbic acid decreases the blue light transmittance in a manner similar to but more weakly than the in vitro vitreous. Higher concentration of AA (up to 9 times the physiological levels) was required to bring the blue light (420-450nm) absorption close to the absorption measured in vitro vitreous samples, indicating that the presence of physiological levels of ascorbic acid does not fully account for the decreased blue light transmittance found in the vitreous.

The source of AA in human vitreous is still controversial and it is not known whether ascorbic acid is secreted into BSS Plus during and after vitrectomy in human eyes. The rat and guinea pig eye experiments have suggested that AA enters the

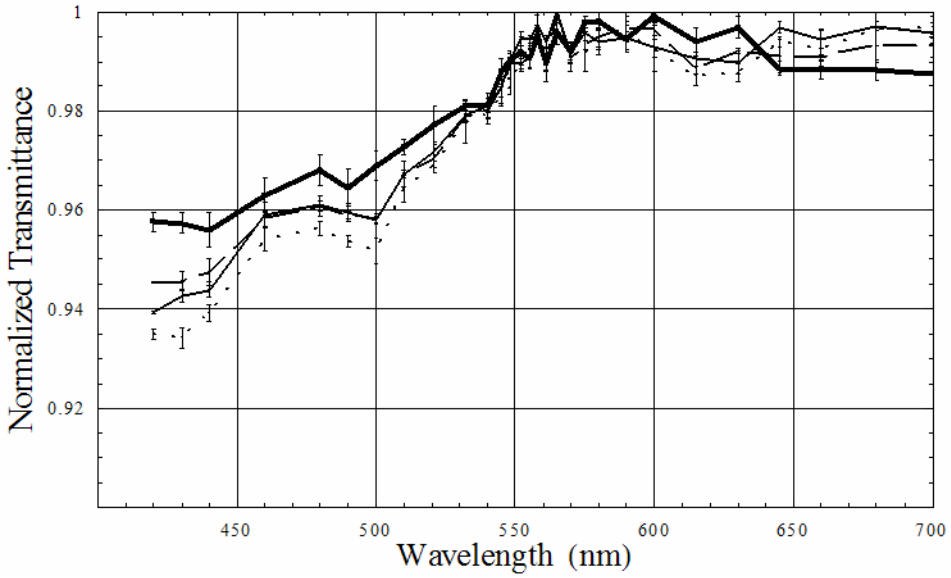

FIGURE 8.6. Four concentrations of BSS Plus and ascorbic acid. The thick solid curve corresponds to a BSS Plus/ascorbic concentration equal to physiological vitreous concentrations. The next three curves (dashed, thin solid, and dotted) of decreasing blue light transmittance correspond to 3, 6 and 9 times the physiological concentration.

vitreous by passive transport down a concentration gradient and data from rabbit eye have shown the evidence of trace amounts of ascorbic acid in BSS Plus 24 hours post-vitrectomy. [96, 97]

As shown by our study, a substantial amount of ascorbic acid must be added to BSS Plus to provide the same level of absorption measured in vitreous. Our studies predict that the substitution of BSS Plus for vitreous during vitrectomy increases the transmission of blue light to the pig retina by 8-9%. This increased blue light transmission could induce retinal phototoxicity, particularly in the presence of posterior chamber intraocular lenses. [74, 98, 99, 100] The replacement of natural human crystalline lens with a conventional IOL substantially increases the amount of blue light transmitted to the retina as IOLs in current use do not absorb blue light like the human crystalline lens. [74, 101, 102, 103] The ageing eye may also be more prone

to light induced photo toxicity because of decreased retinal antioxidants occurring in the retina with age. [93, 94, 95] Although the addition of physiological levels of AA to BSS Plus does not provide the same level of blue light absorption offered by vitreous, it may still provide a significant amount of protection against blue light, particularly in aging eyes and in the presence of IOLs. We also speculate that the addition of ascorbic acid to BSS Plus may be beneficial during vitrectomy as it may decrease the exposure of retina to excessive light from surgical microscope and the endoilluminator by absorbing blue light. [11, 104] We are in the process of testing the retinal photo toxic effects of light from surgical microscope and endoilluminator on the retina with ascorbic acid in BSS Plus in an animal model.

Chapter 9
Conclusions and Future Work

Chapter 9 gives a brief summary of the key results presented in this dissertation and the author's suggestions for improvements to further this research. Recommendations are made for modifications to existing intravitreal techniques, data processing and suggestions are made for important future experiments to perform. Finally, the potential benefits of straylight modeling of retinal vessel imaging using intravitreal illumination is discussed and a preliminary model is presented.

9.1 Summary

Intravitreal illumination was employed to measure the optical properties of the retina and ocular fundus. A novel means of measuring oxygen saturation by fitting vessel spectral data to a nonlinear transmittance model was developed and used throughout the dissertation to estimate the blood oxygen saturation level of retinal vessels. Chapter 3 describes the development of the intravitreal illumination technique as it was performed on enucleated eyes. Multispectral retinal images obtained from the enucleated eye were taken as saline and blood of various blood oxygen saturation levels were manually pumped through the retinal vasculature via the chorio-retinal artery. This rather remarkable experiment was possible due to the skill of Dr. Robert I. Park, the retinal surgeon in collaboration with the author for all of the experiments described in this dissertation. In Chapter 4 the Lambertian model that is typically applied to fundus reflectance was tested by an experiment performed on two enucleated swine eyes in which the integrated diffuse reflectance of the fundus was quantitatively measured for a variety of illumination angles. The results showed that the fundus behaves generally as a Lambertian reflector to within 20%.

The development of the intravitreal illumination technique on enucleated eyes culminated in the application of this experimental technique to a series of live swine experiments. Chapter 5 discusses retinal oximetric measurements made on two swine for a variety of systemic blood oxygenation levels. Resulting vessel spectra proved to be largely free of the "glint" from the vessel apex that has plagued data obtained from extraocular illumination techniques. For one of the swine eyes studied in Chapter 5 we were able to successfully insert a small chip of Spectralon beneath the sensory retina. The same vessels are studied in this configuration and the results are described in the first half of Chapter 6. The latter half of Chapter 6 describes a third live swine experiment designed to study the effects of vitrectomy on retinal blood oxygenation and its correlation with systemic blood oxygen saturation. The data strongly indicates that vitrectomy adversely affects the correlation of systemic and retinal venous blood oxygen saturation.

Fundus reflectance was extensively analyzed in Chapter 7, and two interesting data analysis techniques were developed. Fourier methods were used to check and correct for relative motion between the illuminator and the retinal surface. Secondly, a technique was developed to convert the relative diffuse spectral reflectance measurements obtained from the swine described in Chapters 5 and 6 into absolute diffuse spectra reflectance measurements. A by product of the latter technique is that the melanin content and equivalent blood thickness layer of the fundus region was calculated from the spectral measurements.

The role of ascorbic acid in blue light absorption is the concluding analysis of this dissertation. Spectral transmittance analysis of enucleated vitreous and concentrations of saline solution and ascorbic acid revealed that ascorbic acid plays a large role in the absorption of harmful blue wavelength light for normal eyes. It is likely that much of the protective blue light absorption of the vitreous may be restored to patients having undergone vitrectomy by inclusion of the correct concentration of ascorbic acid into the vitreous replacement material.

9.2 Suggestions for Future Research

Perhaps the most fundamental aspect of the methodology used in the research for this dissertation was the technique of imaging spectrometry: multispectral images were obtained of a test target (the retina) and spectra were constructed over regions of interest. Specifically, the multispectral reflectance from the fundus was measured by sequentially illuminating the fundus with a predetermined set of quasimonochromatic illumination wavelengths. While this technique has its merits and proved to be effective, other techniques are constantly being invented, and their development should be periodically monitored and evaluated for applicability to multispectral fundus imaging. This section describes potential improvements to the current intravitreal illumination including image acquisition and processing techniques, and concludes with a description of future experiments that should be performed.

9.2.1 Data Processing Techniques: Image Alignment

Accurate oximetric calculation, regardless of the technique used, relies on accurate measurement of vessel spectra. Two very important factors affect the proper measurement of these required spectra including glint and animal motion during image acquisition. Intravitreal illumination by its nature allows for the minimization of glint effects; if retinal vessels are illuminated obliquely, the specular reflection from the vessel apex (i.e. glint) does not enter the aperture of the imaging system. Animal motion during image acquisition manifests itself as image misregistration, and this was the single largest detriment to accurate vessel spectra measurement encountered during this research.

The images obtained in this research were corrected for motion artifacts by alignment with a mutual information maximization algorithm. For most multispectral image sets, this technique worked quite well, even though the technique was not developed to its full capacity. One general rule determines how well misaligned im-

ages are corrected: the more alike two misaligned images are, the better chance one has at successfully aligning them. The similarity of the spectral images varied with wavelength, as is evident in the abundance of spectral images shown throughout this dissertation. Generally speaking, the images from 420nm to 590nm had dark vessels and were readily aligned. Images obtained with red wavelengths (600-700nm) resulted in vessels that were often brighter than the background, precluding them from automatic alignment with dark vessel images. A study (possibly a dissertation) focused on improving the image alignment algorithm should look at techniques such as edge detection filtering (high pass filtering), alternate merit functions, and different search algorithms.

9.2.2 General Improvements on Current Intravitreal Techniques

This section details a few general improvements that should be made before the next generation of research using intravitreal illumination is performed. Most of these improvements are practical in nature, and appear to be obvious in hindsight. They are mentioned here in the hope that future research will benefit from them.

Obtaining multispectral retinal images from a swine during a during a live surgical procedure is a complicated process that requires careful planning and coordination of both equipment and people. During the experiments performed for this research, separate optics were used for the surgical procedures (the surgeon used a Leica surgical microscope) and for data collection (described in Chapter 5). A simplification in data collection could be achieved by retrofitting the assist port of the surgical microscope with a mount for the scientific grade camera used for multispectral image acquisition. Successful implementation of this recommendation would require two things: a highly sensitive CCD camera (roughly half the light is available to the assist port because of the embedded beam splitter) and a carefully chosen vitrectomy lens of appropriate optical power to supply the desired image magnification. The potential benefits of

such a change in procedure warrant the effort required to implement the modification.

The light pipe holder described in Chapter 3 was a moderately successful first design, but is by no means fully optimized for use in a surgical setting. Important characteristics for a satisfactory holder include ease of use, stability during data collection, and flexibility of positioning. Further improvements to the light pipe holder should include an "umbrella" type feature on the light pipe to control depth of the end of the fiber.

Perhaps the biggest improvement to be made in regards to hardware could be achieved by fabrication of a fiber optic cable with an embedded beam sampler. The sampled light from the scanning monochromator would be used to measure the amount of spectral illumination incident on the retinal spectral *absolutely*, effectively providing an absolute imaging spectro-radiometer. This modification would circumvent the need to use the methods developed in Chapter 7 to estimate the absolute reflectance of the fundus, for example. Proper use of this technique would require careful measurement of the beam profile as a function of propagation distance.

As a final comment on data collection, if not performing experiments in a confocal arrangement, consider using the least amount of illumination light as possible to reduce the effects of stray light.

9.2.3 Intravitreal Illumination: Straylight Modeling

A primary source of error associated with any imaging application is due to the presence of straylight. Straylight effects are amplified in retinal imaging due to the integrating sphere like behavior of the optical globe. It is the author's opinion that a comprehensive straylight model of the intravitreal illumination/fundus imaging system should be developed to increase the understanding of straylight effects in retinal imaging. Several software packages have been designed for the general task of straylight analysis including Trace Pro (Lambda Research Corporation, Littleton,

Massachusetts), ASAP (Breault Research, Tucson, AZ), and FRED (Photon Engineering, Tucson, AZ). A preliminary FRED model developed by the author is briefly presented now. This model is meant only to illustrate the potential benefits of such an analysis and to describe the capabilities of the software. A comprehensive discussion or development of such a model is beyond the scope of this dissertation.

Figure 9.1 shows the FRED model developed by the author. In the figure, the important components of the intravitreal illumination/fundus imaging system have been included: the fiber optic illuminator, the macrozoom lens (modeled as a classic double Gauss design), a CCD detector, and the eye. The eye model was built based on the Liou model, which is described elsewhere for the interested reader. [105] FRED allows for many scatter and reflectance models to be applied to any optical surface layer, and has the ability to handle stratified layers. Rays are tracked through the optical system and quantified on the detector plane. Ray paths can be differentiated and quantified separately based on the paths that they traveled through the optical system. For example, rays that exit the light pipe, strike the fundus and are scattered directly into the system aperture can be differentiated from rays that leave the fundus, strike the globe and re-illuminate the fundus.

Modeling could also be conducted at a smaller scale, at red blood cell (RBC) level to help understand the scattering behavior of light from the bicuspid RBC. The opportunities to increase understanding of straylight and light scattering are real and exciting.

9.2.4 Future Experiments

The experiments performed and analyzed during this research answered many questions and provided valuable insight, and simultaneously raised many more questions. Understanding the light paths involved in retinal oximetry is of paramount importance to the development of a robust oximetry technique. To increase this under-

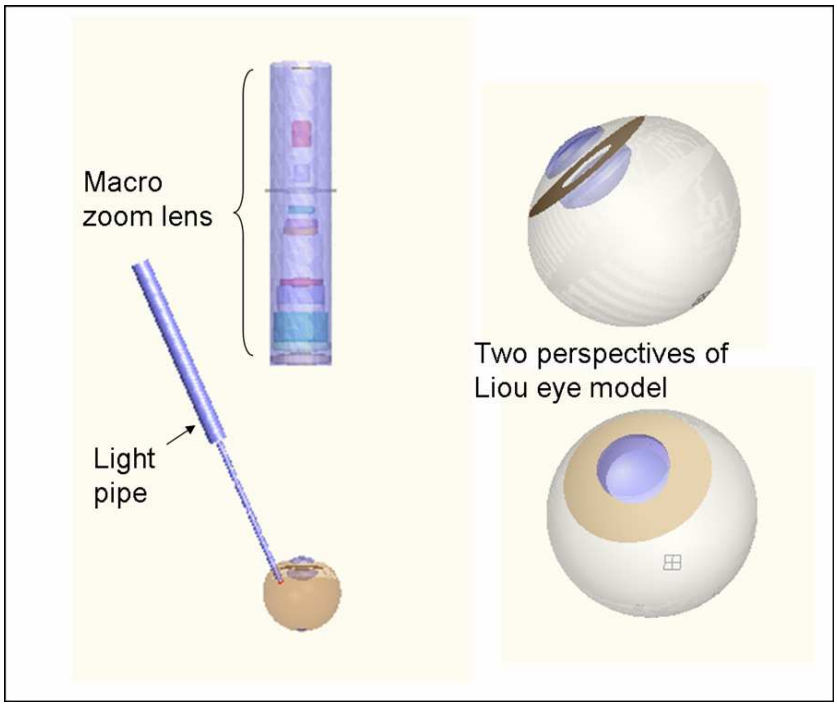

FIGURE 9.1. Optical components used in intravitreal imaging spectroscopy of the eye as modeled in FRED.

standing, more research is necessary, including the following two experiments. Both experiments involve spatially controlling the illumination on the retinal vessels.

For the current intravitreal illumination technique light exits the fiber optic illuminator at an NA=1 (in air). This diverging beam can cause confusion as to light paths and illumination angles, as the illumination angle varies spatially on the target. A modification to the light pipe consisting of a ball lens or similar lens added to the fiber optic illuminator would provide a focused beam on the retina. Scanning this focused spot across the retinal vessel while taking multispectral image sets would provide some separation of light paths collected by the imaging system. An internal aperture placed conjugate to the retinal surface would provide further suppression of scattered light.

Similarly, experiments with small spatial extent collimated light would limit the illumination, perhaps improving the experimental technique used in Chapters 4 and 7 to measure fundus reflectance. Again, this technique would involve considerable optical modifications to the end of the light pipe. The size of the collimated beam would be essentially the same size as the scleratomy created in the globe, which would complicate the maintenance of intraocular pressure during the surgical procedure.

9.2.5 Conclusions

The application of a new illumination technique for studies in retinal vessel oximetry and fundus reflectometry has been characterized and several important results presented in this document. Studies on enucleated swine eyes have provided new insight into the bidirectional reflectance distribution function of the fundus. Research on live swine has shown accurate measurement of retinal vessel oxygen saturation and provided the first *in vivo* spectral transmittance measurement of the sensory retina. A secondary discovery during this research suggests that vitrectomy alters the retinal vasculature, an finding that should spawn new research in its own right. It is the author's hope that this research will be continued and improved upon by future workers to ultimately advance the fields of retinal oximetry and fundus reflectometry.

References

[1] O. van Assendelft, *Spectrophotometry of Haemoglobin Derivatives*, Charles C. Thomas, Springfield, IL, 1970.

[2] J. van de Kraats, T. Berendschott, and D. van Norren, "The pathways of light measured in fundus reflectometry," *Vision Res.* **36**, pp. 2229–2247, 1996.

[3] J. Hickham, R. Frayser, and J. Ross, "A study of retinal venous blood oxygen saturation in human subjects by photographic means," *Circulation* **27**, pp. 375–385, 1963.

[4] D. Benaron, W. Benitz, R. Arigo, and D. Stevenson, "Noninvasive methods for estimating *in vivo* oxygenation," *Clin Pediatr* **31**, pp. 258–73, 1992.

[5] B. Chance, "Current state of methodology on hemoglobin oximetry in tissue," *Adv Exp Med Biol* **345**, pp. 23–32, 1994.

[6] T. Scalea, M. Holman, M. Fuortes, B. Baron, T. Phillips, A. Goldstein, S. Sclafani, and G. Shaftan, "Central venous blood oxygen saturation: Early, accurate measurement of volume during hemorrhage," *J Trauma* **28**, pp. 725–731, 1988.

[7] K. Denninghoff, M. Smith, and L. Hillman, "Retinal imaging techniques in diabetes," *Diabetes Technol Ther* **2**, pp. 111–113, 2000.

[8] E. Steffanson, M. L. III, and M. Wolbarsht, "Oxygenation and vasodilation in relation to diabetic and other proliferative retinopathies," *Ophthalmic Surg* **14**, pp. 209–226, 1983.

[9] E. Steffanson, P. Jensen, and T. E. *et al.*, "Optic nerve oxygen tension in pigs and the effect of carbonic anhydrase inhibitors," *Invest Ophthalmol Vis Sci* **40**, pp. 2756–2762, 1999.

[10] L. D. Schaepdrijver, P. Simoens, L. Pollet, H. Lauwers, and J. D. Lay, "Morphological and clinical study of the retinal circulation in the miniature pig. b: Fluorescein angiography of the retina,," *Exp Eye Res* **54**, pp. 975–985, 1992.

[11] R. Michels, C. Wilkinson, and T. Rice, *Retinal Detachment*, The C.V. Mosby Company, 1990.

[12] P. Kaufman and A. Alm, eds., *Adler's Physiology of the Eye, 10th Edition*, Mosby, Inc, 2003.

[13] C. Oyster, *The Human Eye : Structure and Function*, Sinauer Associates, Sunderland, Mass, 1999.

[14] A. Alm and B. Ehinger, *Development and Structure of the Retina*, Mosby, Inc, 2003.

[15] G. Cioffi, E. Granstam, and A. Alm, *Ocular Circulation*, Mosby, Inc, 2003.

[16] A. Alm and A. Bill, "Ocular and optic nerve blood flow at normal and increased intraocular pressures in monkeys (*Macaca irus*): a study with radioactively labelled microspheres including flow determinations in brain and some other tissues," *Exp Eye Res* **15**, p. 31, 1973.

[17] S. Hayreh, "The ophthalmic artery: Iii. branches," *Br J Ophthalmol* **46**, p. 212, 1962.

[18] B. Kiss, E. Polska, G. Dorner, K. Polak, O. Finl, G. Mayrl, H. Eichler, M. Wolzt, and L. Schmetterer, "Retinal blood flow during hyperoxia in humans revisited: Concerted results using different measurement techniques," *Microvasc Res* **64**, pp. 75–85, 2002.

[19] G. Feke, H. Tagawa, D. Deupree, D. Goger, J. Sebag, and J. Weiter, "Blood flow in the normal human retina," *Invest Ophthalmol Vis Sci* **30**, pp. 58–65, 1989.

[20] G. Feke, D. Goger, H. Tagawa, and F. Delori, "Laser doppler technique for absolute measurement of blood speed in retinal vessels," *IEEE Trans Biomed Eng BME* **34**, pp. 673–80, 1987.

[21] J. Caprioli, M. Sears, and A. Mead, "Ocular blood flow in phakic and aphakic monkey eyes," *Exp Eye Res* **39**, pp. 1–7, 1984.

[22] V. Twersky, "Multiple scattering of waves and optical phenomena," *J Opt Soc Am* **52**, pp. 145–171, 1962.

[23] V. Twersky, "Absorption and multiple scattering of biological suspensions," *J Opt Soc Am* **60**, pp. 1084–1093, 1970.

[24] W. Eaton, E. Henry, J. Hofrichter, and A. Mozzarelli, "Is cooperative oxygen binding in hemoglobin really undersood?," *Nat. Struct. Biol.* **6**, pp. 351–358, 1999.

[25] M. Smith, "Optimum wavelength combinations for retinal vessel oximetry," *Applied Optics* **38**, pp. 258–267, 1999.

[26] R. N. Pittman and B. R. Duling, "A new method for the measurement of percent oxyhemoglobin," *J. Appl. Physiol.* **38**, pp. 315–320, 1975.

[27] D. Schweitzer, M. Hammer, J. Kraft, E. Thamm, E. Konigsdorffer, and J. Strobel, "*In vivo* measurement of the oxygen saturation of retinal vessels in healthy volunteers," *J Appl Physiol* **94**, pp. 891–896, 2003.

[28] M. Smith, *Oximetry of Blood in Retinal Vessels, Dissertation*, University of Alabama in Huntsville, Huntsville, Alabama, 1996.

[29] A. Cohen and R. Laing, "Determination of retinal blood oxygen-saturation from microdensitometer scans of ocular photographs," *Photogr Sci Eng* **20**, pp. 31–34, 1976.

[30] A. Cohen and R. Laing, "Multiple-scattering analysis of retinal blood oximetry," *IEEE Trans Biomed Eng BME* **23**, pp. 391–400, 1976.

[31] F. Delori, "Noninvasive technique for oximetry of blood in retinal-vessels," *Applied Optics* **27**, pp. 1113–1125, 1988.

[32] F. Delori and K. Pflibsen, "Spectral reflectance of the human ocular fundus," *Applied Optics* **28**, pp. 1061–1077, 1989.

[33] M. Smith, K. Denninghoff, A. Lompado, and L. Hillman, "Effect of multiple light paths on retinal vessel oximetry," *Applied Optics* **39**, pp. 1183–1193, 2000.

[34] K. Denninghoff, M. Smith, R. Chipman, L. Hillman, P. Jester, C. Hughes, F. Hughn, and L. Rue, "Retinal large vessel oxygen saturations correlate with early blood loss and hypoxia in anesthetized swine," *J Trauma* **43**, pp. 29–34, 1997.

[35] K. Denninghoff, M. Smith, L. Hillman, D. Redden, and L. Rue, "Retinal venous oxygen saturation correlates with blood volume," *Acad Emerg Med.* **5**, pp. 577–582, 1998.

[36] K. Denninghoff, M. Smith, A. Lompado, and L. Hillman, "Retinal venous oxygen saturation and cardiac output during controlled hemorrhage and resuscitation," *J Appl Physiol* **94**, pp. 891–896, 2003.

[37] J. Beach, K. Schwenzer, , S. Srinivas, D. Kim, and J. Tiedeman, "Oximetry of retinal vessels by dual-wavelength imaging: calibration and influence of pigmentation," *J Appl Physiol* **86**, pp. 748–758, 1999.

[38] B. Khoobehi, J. Beach, and H. Kawano, "Hyperspectral imaging for measurement of oxygen saturation in the optic nerve head," *Invest Ophthalmol Vis Sci* **45**, pp. 1464–1472, 2004.

[39] J. Vos, A. Munnik, and J. Boogaard, "Absolute spectral reflectance of the fundus oculi," *J Opt Soc Am* **55**, pp. 573–574, 1965.

[40] D. van Norren and L. Tiemeijer, "Spectral reflectance of the human eye," *Vision Research* **26**, pp. 313–320, 1986.

[41] M. Hammer, D. Schweitzer, L. Leistritz, M. Scibor, K. Donnerhacke, and J. Strobel, "Imaging spectroscopy of the human ocular fundus *in vivo"*, journal=,"

[42] M. Hammer and D. Schweitzer, "Quantitative reflection spectroscopy at the human ocular fundus," *Phys Med Biol* **47**, pp. 179–191, 2002.

[43] F. Delori, "Spectrophotometer for noninvasive measurement of intrinsic fluorescence and reflectance of the ocular fundus," *Applied Optics* **33**, pp. 7439–7452, 1994.

[44] F. D. S. Burns, "Fundus reflectance and the measurement of crystalline lens density," *J Opt Soc Am A* **13**, pp. 215–226, 1996.

[45] N. Zagers, J. vand de Kraats, T. Berendschot, and D. van Norren, "Simultaneous measurement of foveal spectral reflectance and cone-photoreceptor directionality," *Applied Optics* **41**, pp. 4686–4696, 2002.

[46] R. Knighton, "Quantitative reflectometry of the ocular fundus," *IEEE Trans Biomed Eng BME* **20**, pp. 43–51, 1995.

[47] T. Berendschot, P. DeLint, and D. van Norren, "Fundus reflectancehistorical and present ideas," *Progress in Retinal and Eye Research* **22**, pp. 171–200, 2003.

[48] G. Kortum, *Reflectance Spectroscopy: Principles, Methods, Applications*, Springer-Verlag, New York, 1969.

[49] D. Salyer, N. Beaudry, S. Basavanthappa, K. Twietmeyer, M. Eskandari, K. Denninghoff, and R. I. P. R.A. Chipman, "*In vitro* multispectral diffuse reflectance measurements of the porcine fundus," *Invest Ophthalmol Vis Sci* **46**, pp. 2120–2124, 2005.

[50] D. Salyer, K. Twietmeyer, N. Beaudry, S. Basavanthappa, K. Denninghoff, R. Park, and R. Chipman, "Retinal oximetry using intravitreal illumination," *Current Eye Research* **31**, pp. 617–627, 2006.

[51] M. Knudtson, B. Klein, T. Wong, L. Hubbard, K. Lee, S. Meuer, and C. Bulla, "Variation associated with measurement of retinal vessel diameters at different points in the pulse cycle," *Br J Ophthalmol* **88**, pp. 57–61, 2004.

[52] H. Chen, V. Patel, J. Wiek, and *et. al.*, "Vessel diameter changes during the cardiac cycle," *Eye* **8**, pp. 97–103, 1994.

[53] M. Dumskyj, S. Aldington, C. Dore, and E. Kohner, "The accurate assessment of changes in retinal vessel diameter using multiple frame electrocardiograph synchronised fundus photography," *Cur Eye Res* **15**, pp. 625–632, 1996.

[54] G. Topulos, N. Lipsky, J. L. R. Rogers, and J. Butler, "Fractional changes in lung capillary blood volume and oxygen saturation during the cardiac cycle in rabbits," *J Appl Phys* **82**, pp. 1668–1676, 1997.

[55] P. Viola and W. W. III, "Alignment by maximization of mutual information," *International Journal of Computer Vision* **24**, pp. 137–154, 1997.

[56] D. Schweitzer and M. Scibor, "Imaging spectrometry in ophthalmology - principle and application in microcirculation and in investigation of pigments," *Ophthalmic Research* **28**, pp. 37–44, 1996.

[57] D. Schweitzer, E. Thamm, M. Hammer, and J. Kraft, "A new method for the measurement of oxygen saturation at the human ocular fundus," *Int Ophthalmol* **23**, pp. 347–353, 2001.

[58] K. Levenberg, "A method for the solution of certain problems in least squares," *Quarterly of Applied Mathematics* **2**, pp. 164–168, 1944.

[59] D. Marquardt, "An algorithm for least squares-estimation of nonlinear parameters," *SIAM Journal of Applied Mathematics* **11**, pp. 431–441, 1963.

[60] T. V. D. Berg and K. Tan, "Light transmittance of the human cornea from 320 to 700 nm for different ages," *Vision Res.* **34**, pp. 1453–1456, 1994.

[61] T. Gorgels and D. van Norren, "Spectral transmittance of the rat lens," *Vision Res.* **32**, pp. 1509–1512, 1992.

[62] I. Barbazetto, J. Liang, S. Chang, and et. al., "Oxygen tension in the rabbit lens and vitreous before and after vitrectomy," *Exp Eye Res* **78**, pp. 917–924, 2004.

[63] E. Stefansson, R. Novack, and D. Hatchell, "Vitrectomy prevents retinal hypoxia in branch retinal vein occlusion," *Invest Ophthalmol Vis Sci* **31**, pp. 284–289, 1990.

[64] W. Smiddy and H. Flynn, "Vitrectomy in the management of diabetic retinopathy," *Surv Ophthalmol* **43**, pp. 491–507, 1999.

[65] H. Tabandeh, P. Sullivan, P.Smahliuk, H. Flynn, and J. Schiffman, "Suprachoroidal hemorrhage during pars plana vitrectomy: Risk factors and outcomes," *Ophthalmology* **106**, pp. 236–242, 1999.

[66] H. Nagasaki, K. Shinagawa, and M. Mochizuki, "Risk factors for proliferative vitreoretinopathy," *Prog Retinal Eye Res* **17**, pp. 77–98, 1998.

[67] V. Gabel, R. Birngruber, and F. Hillekamp, "Visible and near infrared light absorption in pigment epithelium and choroid," in *XXIII Concilium Ophthalmologium*, K. Shimizu and J. Oosterhuis, eds., *International Congress Series*, Excerpta Medica, Elsevier, Amsterdam, 1978.

[68] K. Denninghoff, R. Chipman, and L. Hillman, "Oxyhemoglobin saturation measurements by green spectral shift," *Optics Letters* **31**, pp. 1–3, 2006.

[69] J. Dillon, "The photophysics and photobiology of the eye," *J Photochem Photobiol B* **10**, pp. 23–40, 1991.

[70] R. Weale, "Age and the transmittance of the human crystalline lens," *Journal of Physiology* **395**, pp. 577–587, 1988.

[71] S. Zigman, "Environmental near-uv radiation and cataracts," *Optometry and Visual Science* **72**, pp. 899–901, 1995.

[72] A. Cullen, "Photokeratitis and other phototoxic effects on the cornea and conjunctiva," *Int J Toxicol* **21**, pp. 455–464, 2002.

[73] E. Boettner and J. Wolter, "Transmission of the ocular media," *Invest Ophthalmol and Vis Sci* **1**, pp. 776–783, 1962.

[74] A. Bron, G. Vrensen, and e. a. J. Koretz J, "The ageing lens," *Ophthalmologica* **214**, pp. 86–104, 2000.

[75] J. Mellerio, "Yellowing of the human lens: nuclear and cortical contributions," *Vis Res* **27**, pp. 1581–1587, 1987.

[76] A. Ringvold, "The significance of ascorbate in the aqueous humor protection against uv-a and uv-b.," *Exp Eye Res.* **62**, pp. 261–264, 1996.

[77] R. Brubaker and W. B. L. B. J. McLaren, "Ascorbic acid content of human corneal epithelium," *Invest Ophthalmol Vis Sci* **41**, pp. 1681–1683, 2000.

[78] N. Delamere, "Ascorbic acid and the eye," *Subcell Biochem* **25**, pp. 313–329, 1996.

[79] Balazs, "Studies on the structure of the vitreous body. the absorption of ultraviolet light," *Am J Ophthalmol* **38**, pp. 21–28, 1954.

[80] A. Ringvold, E. Anderssen, and I. Kjonniksen, "Ascorbate in the corneal epithelium of diurnal and nocturnal species.," *Invest. Ophthalmol. Vis. Sci.* **39**, pp. 2774–2777, 1998.

[81] A. Ringvold, E. Anderssen, and I. Kjonniksen, "Distribution of ascorbate in the anterior bovine eye.," *Invest. Ophthalmol. Vis. Sci.* **41**, pp. 20–23, 2000.

[82] V. Reddy, F. Giblin, L. Lin, and B. Chakrapani, "The effect of aqueous humor ascorbate on ultraviolet-b-induced dna damage in lens epithelium," *Invest Ophthalmol Vis Sci* **39**, pp. 344–350, 1998.

[83] P. Kaufman and A. Alm, eds., *Adler's Physiology of the Eye, 10th Edition*, Mosby, Inc, 2003.

[84] W. Noell, V. W. B. Kang, and S. Berman, "Retinal damage by visible light," *Invest Ophthalmol Vis Sci* **5**, pp. 450–473, 1966.

[85] W. Ham, J. Ruffolo, H. Mueller, A. Clarke, and M. Moon, "Histologic analysis of photochemical lesions produced in rhesus retina by short-wavelength light," *Invest Ophthalmol Vis Sci* **17**, pp. 1029–1035, 1978.

[86] H. R., Taylor, S. West, B. Munoz, F. S. Rosenthal, S. B. Bressler, and N. M. Bressler, "The long-term effect of visual light to the eye.," *Arch. Ophthalmol.* **110**, pp. 99–104, 1992.

[87] K. Cruickshanks, R. Klein, B. Klein, and D. Nondahl, "Sunlight and the 5-year incidence of early age-related maculopathy: the beaver dam eye study," *Arch Ophthalmol* **119**, pp. 246–250, 2001.

[88] R. Bodannes and P. Chan, "Ascorbic acid as a scavenger of singlet oxygen," *FEBS Lett.* **105**, pp. 195–196, 1979.

[89] B. Halliwell, M. Wasil, and M. Grootveld, "Biologically significant scavenging of the myeloperoxidase-derived oxidant hypochlorous acid by ascorbic acid. implications for antioxidant protection in the inflamed rheumatoid joint," *FEBS Lett* **213**, pp. 15–17, 1987.

[90] R. Rose, "Ascorbic acid protection against free radicals.," *Ann. N.Y. Acad. Sci.* **498**, pp. 506–508, 1987.

[91] M. Nishikimi, "Oxidation of ascorbic acid with superoxide anion generated by the xanthine-xanthine oxidase system 63 (1975), pp. 463-468," *Biochem Biophys Res Comm* **63**, pp. 463–468, 1975.

[92] L. Brown and D. Jones, *The biology of ascorbic acid.*, pp. 117–154. E. Cadenas and K. Packer, New York, 1996.

[93] R. Rose and A. Bode, "Ocular ascorbate transport and metabolism.," *Comp. Biochem. Physiol.* **100**, pp. 273–285, 1991.

[94] J. Berger, D. Shephard, F. Morrow, J. Sadowski, T. H. A., and Taylor, "Reduced and total ascorbate in guinea pig eye tissues in response to dietary intake," *Curr Eye Res* **7**, pp. 681–686, 1988.

[95] S. Takano, S. Ishiwata, M. N. M. Mizugaki, and M. Tamai, "Determination of ascorbic acid in human vitreous humor by high-performance liquid chromatography with uv detection," *Curr Eye Res* **16**, pp. 589–594, 1997.

[96] J. DiMattio, "A comparative study of ascorbic acid entry into aqueous and vitreous humors of the rat and guinea pig," *Invest Ophthalmol Vis Sci* **30**, pp. 2320–2331, 1989.

[97] L. Manjanas, J. Pastor, R. Munoz, and T. Girbes, "Intraocular solutions and vitrectomy-related changes (in protein, lactic and ascorbic acid) in rabbit vitreous," *Ophthalmic Res* **24**, pp. 61–67, 1992.

[98] M. Mainster, "Spectral transmittance of intraocular lenses and retinal damage from intense light sources," *Am J Ophthalmol* **85**, pp. 167–170, 1978.

[99] M. Mainster, "Solar retinitis, photic maculopathy and the pseudophakic eye," *J Am Intraocul Implant Soc* **4**, pp. 84–86, 1978.

[100] M. Mainster, "The spectra, classification, and rationale of ultraviolet-protective intraocular lenses," *Am J Ophthalmol* **102**, pp. 727–732, 1986.

[101] J. Marshall, "The ageing retina: physiology or pathology.," *Eye* **1**, pp. 282–295, 1987.

[102] A. Hunyor, "Solar retinopathy: its significance for the ageing eye and the younger pseudophakic patient," *Aust N Z J Ophthalmol* **15**, pp. 371–375, 1987.

[103] M. Mainster, "Light and macular degeneration: a biophysical and clinical perspective," *Eye* **1**, pp. 304–310, 1987.

[104] Y. Ogura, "Retinal irradiation from an operating microscope during vitrectomy: Observation by endoscopy," *Ophthalmic Surg Lasers* **27**, pp. 636–637, 1996.

[105] H. Liou and N. Brennan, "Anatomically accurate, finite model eye for optical modeling," *J. Opt. Soc. Am.* **14**, pp. 1684–1695, 1997.